REPORT DOCUMENTATION PAGE

Form Approved
OMB No. 0704-0188

1. AGENCY USE ONLY (Leave blank)	2. REPORT DATE	3. REPORT TYPE AND DATES COVERED
	September 1994	Final (Aug. 93 - Aug. 94)

4. TITLE AND SUBTITLE

A THEORETICAL STUDY ON IGNITION MECHANISMS OF LIQUID PROPELLANTS

5. FUNDING NUMBERS

DAAH04-93-G-0409

6. AUTHOR(S)

A. Prosperetti and H. Yuan

7. PERFORMING ORGANIZATION NAME(S) AND ADDRESS(ES)

The Johns Hopkins University, Department of Mechanical Engineering
Latrobe Hall
Baltimore MD 21218

8. PERFORMING ORGANIZATION REPORT NUMBER

9. SPONSORING/MONITORING AGENCY NAME(S) AND ADDRESS(ES)

U.S. Army Research Office
P.O. Box 12211
Research Triangle Park, NC 27709-2211

10. SPONSORING/MONITORING AGENCY REPORT NUMBER

ARO 31572.1-EG

11. SUPPLEMENTARY NOTES

The views, opinions and/or findings contained in this report are those of the author(s) and should not be construed as an official Department of the Army position, policy, or decision, unless so designated by other documentation.

12a. DISTRIBUTION/AVAILABILITY STATEMENT

Approved for public release; distribution unlimited.

12b. DISTRIBUTION CODE

13. ABSTRACT *(Maximum 200 words)*

Two possible mechanisms for the accidental ignition of liquid propellants are studied: (*i*) The heating of the liquid surrounding a strongly compressed gas bubble, and (*ii*) The heating due to viscous dissipation in a rapidly compressed drop. For the first problem the heating of the gas is calculated precisely rather than estimated on the basis of an adiabatic model. For the second problem proper allowance is made for the temperature dependence of the liquid viscosity. In general, the results indicate that ignition is in principle possible, although marginally so. This finding is generally consistent with experiment, and it may explain why it is difficult to deduce definite conclusions from the available experimental evidence.

14. SUBJECT TERMS			15. NUMBER OF PAGES
liquid propellant ignition, gas bubble heating, viscous heating			66
			16. PRICE CODE
17. SECURITY CLASSIFICATION OF REPORT	18. SECURITY CLASSIFICATION OF THIS PAGE	19. SECURITY CLASSIFICATION OF ABSTRACT	20. LIMITATION OF ABSTRACT
UNCLASSIFIED	UNCLASSIFIED	UNCLASSIFIED	UL

A THEORETICAL STUDY ON IGNITION MECHANISMS OF LIQUID PROPELLANTS

ARO Grant No. DAAL04 - 93 - G - 0409

Final Report for the
Period August 15 1993 - August 14 1993

A. Prosperetti and H. Yuan
Department of Mechanical Engineering
The Johns Hopkins University
Baltimore MD 21218

Prepared: September 14, 1994

ABSTRACT

Two possible mechanisms for the accidental ignition of liquid propellants are studied: (*i*) The heating of the liquid surrounding a strongly compressed gas bubble, and (*ii*) The heating due to viscous dissipation in a rapidly compressed drop. Contrary to previous work, for the first problem the heating of the gas is calculated precisely rather than estimated on the basis of an adiabatic model, while for the second one proper allowance is made for the temperature dependence of the liquid viscosity.

For the first problem the compression due to a pressure pulse and a pressure step have been studied. In the first case, the maximum response is found when the pulse time scale is comparable to that for the collapse of the bubble. The temperature reached by the liquid can be in excess of 1,000 K, which presumably would lead to vaporization not accounted for in the model. The duration of such high temperatures however is probably too limited for direct ignition. However, if the propellant vaporizes, its vapor can conceivably be heated during the next compression cycle of the bubble oscillatory motion. Some limited results for the case of non-spherical collapse of the bubble are also presented.

For the viscous heating problem a marked effect of the temperature dependence of viscosity has been found. Furthermore, although very high temperatures develop when the velocity with which the drop is compressed is held constant, this only happens when the pressure is so large that the assumption of a constant velocity is unrealistic. The effect of a wall slip boundary condition has also been studied and found to be large. The results indicate that the process under consideration is strongly influenced by subtle aspects that cannot be ignored even as a first approximation.

In general, all the results indicate that ignition is in principle possible, although marginally so. While this finding is generally consistent with experiment, it may also explain why it is difficult to deduce definite conclusions from the available experimental evidence with its apparently inconsistent results.

Contents

LIST OF FIGURES FOR CHAPTER 2

Fig. 16. Normalized radius R/R_0 versus the normalized time t/t_R for an air bubble with initial radius R_0 = 1 mm subject to a step pressure increase $\Delta p = 100$ bars. The Rayleigh collapse time is $t_R = 9.2$ μs.

Fig. 17. Core gas (dashed) and bubble surface (solid) temperatures for a step pressure increase with $\Delta p =$ 100 bars and $R_0 = 0.1$ mm. The Rayleigh time is $t_R = 0.92$ μs.

Fig. 18. Core gas (dashed) and bubble surface (solid) temperatures for a step pressure increase with $\Delta p =$ 100 bars and $R_0 = 1$ mm. The Rayleigh time is $t_R = 9.2$ μs.

Fig. 19. Core gas (dashed) and bubble surface (solid) temperatures for a step pressure increase with $\Delta p =$ 100 bars and $R_0 = 10$ mm. The Rayleigh time is $t_R = 92$ μs.

Fig. 20. Bubble surface temperature for a step pressure increase with $\Delta p = 100$ bars and $R_0 = 10$ mm. The Rayleigh time is $t_R = 92$ μs. These results differ from those of Fig. 19 because here the liquid thermal conductivity is 0.075 rather than 0.15 W/mK and the gas adiabatic index is 5/3 rather than 7/5.

Fig. 21. Example of a numerically generated orthogonal grid for the solution of the Laplace and energy equation in the gas. Here the initial bubble has a radius $R_0 = 1$ mm, with a rigid wall 1.2 mm below the initial bubble center. The collapse is triggered by a pressure step $\Delta p = 10$ bars. The grid is shown at the time $t = 26.64$ μs. The Rayleigh time is $t_R = 29$ μs.

Fig. 22. The left figure shows isotherms calculated with the full model for $R_0 = 1$ mm, with a rigid wall 1.2 mm below the initial bubble center and a pressure step $\Delta p = 10$ bars at $t = 26.64$ μs. The right figure shows the corresponding lines of constant Φ. Here the Rayleigh time is $t_R = 29$ μs.

Fig. 23. The gas temperature along the axis of symmetry of the bubble (from the closest to the farthest point from the wall) for the case of the previous figure.

Fig. 24. Comparison between the gas temperatures predicted by the full model (dashed line) and the boundary layer approximation (solid line) for the spherical collapse of an air bubble with $R_0 = 1$ mm and a step pressure increase $\Delta p = 10$ bars.

Fig. 25. Comparison between the heat fluxes at the jet tip predicted by the full model (dashed line) and the boundary layer approximation (solid line) for an asymmetric collapse. The case is that of Figs. 21 to 23.

Fig. 26. Successive bubble configurations for a collapse induced by a sudden overpressure with $\Delta p = 10$ bars, $p_0 = 1$ bar. The initial bubble radius is $R_0 = 1$ mm and the rigid wall is initially 1.2 mm below the bubble center.

Fig. 27. Successive shapes of a 1 mm-radius air bubble subjected to a Gaussian pressure pulse (2.3.1) with with $t_R/t_p = 4$ and $\Delta p = 10$ bars. Notice that the jet continues to move toward the opposite bubble surface even while the rest of the bubble is rebounding.

Fig. 28. The local heat flux along the bubble surface for a step pressure increase $\Delta p = 10$ bars as computed from the boundary-layer model at different times for $R_0 = 1$ mm. The abscissa denotes the node number. At each time step sixty equispaced nodes were used.

Fig. 29. Estimated jet tip liquid temperature as a function of time for the case of Figs. 21 to 23 (solid line). The dashed line is the liquid temperature for a spherical collapse.

LIST OF FIGURES FOR CHAPTER 3

1 Introduction

The increasing technological importance of liquid monopropellants such as LGP 1845 and 1846 motivates a strong interest in the safe operational limits of their use (see e.g. Knapton et al. 1992 for a review). In particular, the propellant behavior under conditions of high pressures, strong impact, or high-speed flow has a direct bearing on safety issues. In view of its thermal nature, for ignition to occur, the mechanical energy associated with these processes must somehow lead to the formation of so-called 'hot spots'. A number of mechanisms for this to happen have been described in the literature (see e.g. Field et al. 1982; Field et al 1992). In the work described in this report, following our original proposal, we focus on two:

1. The heating of the liquid surrounding a strongly compressed gas bubble avoiding the assumption of adiabatic behavior of the gas in the bubble.

2. The heating due to viscous dissipation in a rapidly compressed drop accounting for the temperature dependence of the liquid viscosity.

According to Field (1992; Field et al. 1992), the "hot spots" responsible for ignition need to have dimensions of typically 0.1 - 10 μm, duration of 0.01 to 1 msec, and temperatures greater than $\sim$ 700 K. It is useful to keep in mind these orders of magnitude in the light of the results described below.

2 Bubble Collapse

One of the scenarios envisaged for the observed accidental ignition is as follows: A gas bubble can remain trapped by several mechanisms in the course of propellant transport and filling operations. When this bubble is exposed to high pressures (e.g. due to shock waves generated by water hammer effects or other causes), it collapses and the nearly-adiabatic heating of the gas can cause a temperature rise of the surrounding liquid sufficient to cause ignition. The concrete possibility of explosive sensitization due to gas cavities has been demonstrated for solid propellants (see e.g. Heavens and Field 1974; Chaudhri and Field 1974; Field et al. 1982; Krishna Moan and Field 1984). For liquid propellants the experimental evidence is less clear (Coley and Field 1973; Bourne and Field 1989, 1991, 1992). While sometimes initiation is observed, many times it is not and, furthermore, the role played by the impacting of the microjet on the opposite side of the bubble is unclear. Theoretically, the situation is not much clearer. While some authors (e.g. Andersen and Gillespie 1980) discount the role of gas pocket compression, others (Johansson 1958; Randolph and Simpson 1976; Morrison et al. 1982; Frey 1985) reach the opposite conclusion.

In all of the previous theoretical analyses, the gas behavior in the collapsing bubble was modelled very crudely, usually by assuming adiabatic behavior. The purpose of this part of the work is to relax this assumption and to account properly for the thermal behavior of the gas. We shall consider two cases, spherical collapse and asymmetric collapse in the vicinity of a plane rigid wall.

2.1 Mathematical Formulation

We assume that the liquid is incompressible and inviscid so that its velocity field $\mathbf{u}$ can be described in terms of a harmonic potential ϕ

$$\mathbf{u} = \nabla\phi, \qquad \nabla^2\phi = 0. \tag{2.1.1}$$

With the neglect of body force that do not influence the process of present concern due to its rapidity, the Bernoulli integral is

$$\frac{\partial\phi}{\partial t} + \frac{1}{2}u^2 + \frac{p_L}{\rho_L} = \frac{p_\infty(t)}{\rho_L}, \tag{2.1.2}$$

where ρ_L is the liquid density, p_L the pressure, and p_∞ the time-dependent "ambient" pressure (the rising of which will cause the bubble to collapse). The kinematic boundary condition on the bubble surface requires

that

$$\mathbf{n} \cdot \frac{d\mathbf{x}_s}{dt} = \mathbf{n} \cdot \nabla\phi\,, \tag{2.1.3}$$

where $\mathbf{n}$ is the unit normal directed into the liquid and $\mathbf{x}_s$ the generic surface point. With the neglect of viscous stresses in the gas, the dynamic boundary condition stipulates that, on the bubble surface S,

$$p - p_L = \sigma\mathcal{C} \tag{2.1.4}$$

where p is the gas pressure, σ the surface tension coefficient, and $\mathcal{C}$ the local surface curvature reckoned as positive when the centers of curvature lie in the gas. In particular, this relation establishes the value of the internal gas pressure p_{G0} necessary for a spherical bubble with radius R_0 to be in equilibrium in a constant pressure field p_0:

$$p_{G0} - p_0 = \frac{2\sigma}{R_0}\,. \tag{2.1.5}$$

In our treatment of the gas we assume that the Mach number of the gas flow is small so that the gas pressure p is approximately uniform in space,

$$p(\mathbf{x}, t) \simeq p(t)\,. \tag{2.1.6}$$

This assumptions is certainly justified during the greatest part of the collapse. In the very latest stages the bubble wall can reach velocities of several thousand m/s, but on the other hand the gas temperature is also quite high so that the speed of sound can easily be greater than 1,000 m/s. Thus, while one expects (2.1.6) to be in error in the final stages of the collapse, this error is in fact smaller than might appear at first and is also significant only for a minute fraction of the total process. The approximation (2.1.6) avoids the need to consider the momentum equation in the gas.

The gas continuity equation is

$$\frac{d\rho_G}{dt} + \rho_G \nabla \cdot \mathbf{v} = 0\,, \tag{2.1.7}$$

where ρ_G and $\mathbf{v}$ are the density and velocity fields in the gas and $d/dt = \partial/\partial t + \mathbf{v} \cdot \nabla$ denotes the convective derivative, and the gas energy equation is

$$\rho_G C_p \frac{dT}{dt} + \frac{1}{\rho_G}\left(\frac{\partial \rho_G}{\partial T}\right)_p \frac{dp}{dt} = \nabla \cdot (K \nabla T)\,, \tag{2.1.8}$$

where C_p and K are the constant-pressure specific heat and thermal conductivity and T is the temperature field. For a perfect gas

$$p = \mathcal{R}\rho_g T\,, \tag{2.1.9}$$

where $\mathcal{R}$ is the universal gas constant divided by the gas molecular weight, so that

$$\left(\frac{\partial \rho_G}{\partial T}\right)_p = \frac{1}{T}\,. \tag{2.1.10}$$

Furthermore, upon combining (2.1.7) and (2.1.8) and using the fact that

$$C_p \rho_G T = \frac{\gamma}{\gamma - 1} p\,, \tag{2.1.11}$$

where γ is the ratio of specific heats, one finds

$$\frac{dp}{dt} + \gamma p \nabla \cdot \mathbf{v} = (\gamma - 1)\nabla \cdot (K \nabla T)\,. \tag{2.1.12}$$

Upon using the assumed spatial uniformity of p, this equation can be cast in the form

$$\nabla \cdot \left(\gamma p \mathbf{v} + \frac{1}{3}\dot{p}\mathbf{x} - (\gamma - 1)K\nabla T\right) = 0\,, \tag{2.1.13}$$

where $\mathbf{x}$ is the position vector and the dot denotes the time derivative. This equation can be integrated to find

$$\gamma p \mathbf{v} + \frac{1}{3}\dot{p}\mathbf{x} - (\gamma - 1)K\nabla T = \mathbf{A}\,, \tag{2.1.14}$$

where

$$\nabla \cdot \mathbf{A} = 0\,. \tag{2.1.15}$$

Upon solving for $\mathbf{v}$ and calculating the vorticity field we find

$$\gamma p \nabla \times \mathbf{v} = \nabla \times \mathbf{A} + (\gamma - 1)\nabla \times (K\nabla T)\,. \tag{2.1.16}$$

In gases the thermal conductivity is very nearly dependent only on the temperature, so that the last term is negligible. This relation then shows that $\nabla \times \mathbf{v} \propto \nabla \times \mathbf{A}$. On the other hand, it is well known from Fluid Mechanics that, in a motion started from rest, vorticity can only arise due to the barotropic term proportional to $\nabla\rho_G \times \nabla p$ or to diffusion from the boundaries and convection. The barotropic term vanishes here due to (2.1.6) and, due to the small value of the dynamic viscosity for gases, we shall neglect boundary vorticity diffusion. As a consequence, we must require that $\nabla \times \mathbf{A} \simeq 0$. We thus may write $\mathbf{A} = \nabla\Phi$ with, from (2.1.15),

$$\nabla^2\Phi = 0\,. \tag{2.1.17}$$

Hence, from (2.1.14) the gas velocity field can be expressed as

$$\mathbf{v} = \frac{1}{\gamma p}\left[(\gamma - 1)K\nabla T + \nabla\Phi - \frac{1}{3}\dot{p}\mathbf{x}\right]\,. \tag{2.1.18}$$

Another consequence of (2.1.13) is an equation for the gas pressure. To find this relation we integrate (2.1.13) over the bubble volume V and use the divergence theorem to find

$$\int_S \left(\gamma p \mathbf{v} + \frac{1}{3}\dot{p}\mathbf{x} - (\gamma - 1)K\nabla T\right) \cdot \mathbf{n}\, dS = 0\,, \tag{2.1.19}$$

where S is the bubble surface. From this relation we readily obtain

$$\dot{p} = -\frac{1}{V}\left[(\gamma - 1)Q + \gamma p \dot{V}\right] \tag{2.1.20}$$

where

$$Q = -\int_S K\mathbf{n} \cdot \nabla T\, dS \tag{2.1.21}$$

is the total heat conducted into the liquid at the bubble wall.

From Eq. (2.1.18) and the kinematic condition we find a boundary condition for Φ at the bubble wall:

$$\mathbf{n} \cdot \nabla\Phi = \gamma p \frac{d\mathbf{x}_s}{dt} \cdot \mathbf{n} + (\gamma - 1)q_n + \frac{1}{3}\dot{p}\mathbf{x}_s \cdot \mathbf{n}\,, \tag{2.1.22}$$

where

$$q_n = -K\mathbf{n} \cdot \nabla T \tag{2.1.23}$$

is the heat flux into the liquid at the bubble wall.

One last equation is needed to complete the formulation, and this is taken to be the energy equation (2.1.8) specialized to the case of a perfect gas:

$$\frac{\gamma}{\gamma - 1}\frac{p}{T}\left(\frac{\partial T}{\partial t} + \mathbf{v} \cdot \nabla T\right) - \dot{p} = \nabla \cdot (K\nabla T)\,. \tag{2.1.24}$$

2.2 Spherical Bubbles

We apply the previous formulation to the case of spherical bubbles first following our earlier work (Prosperetti et al. 1988; Prosperetti 1991).

For the problem in the liquid, from (2.1.1) and (2.1.3) we have

$$\phi = -\frac{R^2}{r}\dot{R}, \tag{2.2.1}$$

where R is the bubble radius and the radial coordinate r is measured from the bubble center. Upon using (2.1.2) to evaluate the liquid pressure and substituting into the dynamic boundary condition (2.1.4) we find the well-known Rayleigh-Plesset equation

$$R\ddot{R} + \frac{3}{2}\dot{R}^2 = \frac{1}{\rho_L}\left[p - p_\infty(t) - \frac{2\sigma}{R}\right]. \tag{2.2.2}$$

Actually, in the spherical case first-order effects in the liquid compressibility are readily incorporated (see e.g. Prosperetti and Lezzi 1986. Hence, in place of (2.2.2), we shall use

$$\left(1 - \frac{\dot{R}}{c_L}\right) R\ddot{R} + \frac{3}{2}\left(1 - \frac{\dot{R}}{3c_L}\right)\dot{R}^2 = \frac{1}{\rho_L}\left[1 - \frac{\dot{R}}{c_L} + \frac{R}{c_L}\frac{d}{dt}\right]\left(p - p_\infty(t) - \frac{2\sigma}{R}\right). \tag{2.2.3}$$

The only spherically symmetric solution of the Laplace equation for Φ bounded at the origin is $\Phi =$ constant and, since only derivatives of Φ have physical meaning, we can take the constant to be 0. Hence, the gas velocity field becomes, from (2.1.18),

$$v = \frac{1}{\gamma p}\left[(\gamma - 1)K\frac{\partial T}{\partial r} - \frac{1}{3}\dot{p}\, r\right], \tag{2.2.4}$$

where v is the radial component of $\mathbf{v}$. The pressure equation (2.1.20) gives in this case

$$\dot{p} = \frac{3}{R}\left[(\gamma - 1)K\left.\frac{\partial T}{\partial r}\right|_{r=R} - \gamma p\dot{R}\right]. \tag{2.2.5}$$

Upon substitution into (2.2.4) we have

$$v = \frac{1}{\gamma p}\left\{(\gamma - 1)\left[K\frac{\partial T}{\partial r} - \left(K\frac{\partial T}{\partial r}\right)_{r=R}\right] + \gamma\frac{r}{R}p\dot{R}\right\}. \tag{2.2.6}$$

The energy equation (2.1.24) is

$$\frac{\gamma}{\gamma - 1}\frac{p}{T}\left(\frac{\partial T}{\partial t} + v\frac{\partial T}{\partial r}\right) - \dot{p} = \frac{1}{r^2}\frac{\partial}{\partial r}\left(r^2 K\frac{\partial T}{\partial r}\right). \tag{2.2.7}$$

Since the gas temperature excursions are considerable, to increase accuracy we allow the thermal conductivity to depend on temperature and rewrite (2.2.7) in terms of the auxiliary variable

$$\tau = \int_{T_\infty}^{T} K(\theta)\, d\theta, \tag{2.2.8}$$

where T_∞ is the initial temperature. A linear relation for the dependence of K upon T has been assumed as in our previous papers.

In the spherically symmetric case it is also relatively easy to solve the energy equation in the liquid that is

$$\frac{\partial T_L}{\partial t} + \frac{R^2}{r^2}\dot{R}\frac{\partial T_L}{\partial r} = \frac{D_L}{r^2}\frac{\partial}{\partial r}\left(r^2\frac{\partial T_L}{\partial r}\right), \tag{2.2.9}$$

where D_L is the liquid thermal diffusivity.

An efficient numerical model for the solution of these equations has been described in Kamath and Prosperetti (1989) and Kamath et al. (1993). The methd is based on a coordinate transformation in the gas

$$y = \frac{r}{R(t)} \tag{2.2.10}$$

and in the liquid

$$\frac{1}{\xi} = 1 + \ell\sqrt{\frac{\omega R_0^2}{D_L}}\left[\frac{r}{R(t)} - 1\right]. \tag{2.2.11}$$

and a spectral representation of the gas and liquid temperature fields. In (2.2.11) R_0 is the initial bubble radius, ω a characteristic inverse time, and ℓ a numerical constant taken to be about 0.05.

2.3 Results for Spherically Collapsing Bubbles

We now present some numerical results for spherical bubbles. In the examples that follow, unless otherwise indicated, the physical properties of air are used. For the liquid we take $\rho_L = 1{,}452\ \mathrm{kg/m^3}$, $K = 0.15\ \mathrm{W/mK}$, $D_L = 4.49 \times 10^{-8}\ \mathrm{m^2/s}$. These values are representative of LGP 1845.

The equilibrium pressure is $p_0 = 1$ bar and the undisturbed temperature $T_\infty = 293$ K.

We first consider Gaussian pressure pulses with the form

$$p_\infty = p_0 + \Delta p \exp -\frac{t^2}{t_p^2}, \tag{2.3.1}$$

where Δp is the maximum amplitude and t_p is a measure of the width of the pressure pulse.

Our first case is a bubble with $R_0 = 1$ mm for $\Delta p = 10$ bars. The corresponding value of the Rayleigh collapse time t_R defined by

$$t_R = 0.915 R_0\sqrt{\frac{\rho_L}{\Delta p}} \tag{2.3.2}$$

is 29 μs. Figure 1 shows the normalized radius R/R_0 versus the normalized time t/t_R for $t_R/t_p = 0.1$ (dashed), 1(solid), and 10 (dotted). In the first case the pressure rise is slow and the bubble is compressed quasi-statically except for a series of weak nearly free oscillations executed about the instantaneous pressure. When the pressure pulse is much shorter than the collapse time (dotted line), on the other hand, the bubble responds with essentially free oscillations about the undisturbed constant pressure level. When $t_R/t_p = 1$, the collapse is very violent with a volume reduction of nearly two orders of magnitude.

The temperature attained by the gas at the bubble center (squares) and by the liquid at the bubble surface (circles) at the end of the first collapse are shown in Fig. 2 for $t_R/t_p = 0.1$, 0.2, 0.5, 1, 2, 5, and 10. The circles in this figure are the adiabatic prediction for the gas temperature

$$T = T_\infty \left(\frac{V_0}{V}\right)^{\gamma-1}. \tag{2.3.3}$$

It can be seen that the heating is maximum when the pressure time scale t_p is close to the bubble collapse time t_R. In none of these cases, however, the liquid heating appears to be sufficient to cause ignition.

The center gas temperature and the liquid surface temperature for the three cases of Fig. 1 are shown as a function of t/t_R in Figs. 3 and 4 respectively (the figures are drawn to the same scale). As before the dashed curves are for $t_R/t_p = 0.1$, the solid ones for $t_R/t_p = 1$, and the dotted ones for $t_R/t_p = 10$. The marked differences caused by the "detuning" of the rate of compression with respect to the collapse time are very clear from these figures also. Figure 5 shows the corresponding wall heat flux. The duration of the temperature spike for $t_R/t_p = 1$ is less than 2 μs and therefore shorter than the lower bound on the duration required for ignition quoted in section 1. The maximum temperature reached by the liquid, on the other

hand (Fig. 4) seems to be too small to cause ignition. Figure 6 is the amount of heat Q delivered to the liquid as a function of time:

$$Q(t) = 4\pi \int_0^t R^2 K \left.\frac{\partial T}{\partial r}\right|_{r=R(t)} dt\,. \tag{2.3.4}$$

Since these results show that the largest temperature rises occur for $t_R \simeq t_p$, we now consider the effect of the bubble radius when $t_R = t_p$ for the same $\Delta p = 10$ bars in Figs. 7 and 8. These figures show the core gas (dashed) and the bubble surface (solid) temperature for $R_0 = 100$ μm and 10 mm respectively. The corresponding values of t_R are 2.9 μs and 0.29 ms. The temperature responses are very similar when plotted as functions of the normalized time t/t_R as here. The first compression gives a high temperature in the gas, but the rise in the liquid is relatively modest. The subsequent gas temperature oscillations due to the free oscillations executed after the passage of the pulse (see Fig. 1) hardly affect the liquid temperature.

When the magnitude of the pressure pulse is larger, $\Delta p = 100$ bars, as in Figs. 9 to 11, the general behavior is also little dependent on the value of the radius on a t/t_R scale. These figures refer to $R_0 = 0.1$, 1, and 10 mm. The corresponding values of t_R are 0.92, 9.2, and 92 μs. The liquid temperature accompanying the large gas temperature spike reaches about 1,500 K, but the duration of this extreme temperature seems to be too short to cause ignition even for the 10 mm bubble for which it is of the order of 5 μs. Furthermore, it appears likely that the liquid temperature would be somewhat decreased by vaporization that is not included in the present model.

Another situation of interest is that in which an overpressure of long duration is applied to the bubble:

$$p_\infty(t) = p_0 + \Delta p\, H(t) \tag{2.3.5}$$

where $H(t)$ is Heaviside's step function. This simulates the effect of a compression wave with a rise time faster than the Rayleigh time and a duration much longer than t_R. For a slower rise time the bubble would compress quasi-statically as shown before in Figs. 1, 3, and 4 and the temperature increases would be small.

Figures 12 to 15 are for $\Delta p = 10$ bars. Figure 12 shows the bubble radius versus time for $R_0 = 1$ mm. The pressure step excites oscillations that are slowly damped by the dissipative processes affecting the bubble motion. Asymptotically, the bubble radius tends to a new equilibrium value consistent with the pressure $p_0 + \Delta p$, see (2.1.5). This behavior is typical for all the cases studied. Figures 13 to 15 show the temperature response of the gas and of the liquid for $R_0 = 0.1$, 1 and 10 mm respectively. The liquid temperature rises after each collapse due to the gas temperature spike, but the integrated effect remains small.

The radius-versus-time curve for $R_0 = 1$ mm and a larger pressure step, $\Delta p = 100$ bars, is shown in Fig. 16. The gas and liquid temperature behavior under this stronger excitation are shown in Figs. 17 to 19 again for $R_0 = 0.1$, 1 and 10 mm. The liquid temperature is somewhat greater than before, but still appears to remain below the level required for ignition except for an initial spike with a duration of less than 10 μs. It is doubtful that such marginal conditions would be sufficient to trigger ignition.

We have also conducted a few simulations with a gas adiabatic index $\gamma = 5/3$ (appropriate for monatomic gases) and different values of the liquid thermal conductivity. We give an example in Fig. 20 with $K = 0.075$ W/mK (i.e., half the value used in the previous simulations) $\gamma = 5/3$, $R_0 = 10$ mm, for a step pressure increase $\Delta p = 100$. This figure should therefore be compared with Fig. 19. Due to the greater value of γ the gas heating is much larger than before and is not shown in order to maintain readability of the liquid temperature information. The liquid gets much hotter than before during the initial spike which in this case is somewhat longer than before (about 20 instead of 10 μm). Although, on the basis of the estimate given in the Introduction, ignition would appear to be possible, conditions seem to be too close to marginal to be able to make a definite prediction.

2.4 Non-Spherical Collapse – Full Model

In the case of a non-spherical collapse, no analytical progress is possible and the mathematical model outlined before must be solved by fully numerical means.

For the solution of the potential problem in the liquid we use a boundary integral approach as follows (see e.g. Oguz and Prosperetti 1989, 1990). By evaluating the Bernoulli equation (2.1.2) on the bubble surface and using (2.1.4) to eliminate the liquid pressure we find

$$\frac{d_n\phi}{dt} \equiv \frac{\partial\phi}{\partial t} + u_n\frac{\partial\phi}{\partial n} = u_n^2 - \frac{1}{2}u^2 - \frac{p - \sigma\mathcal{C} - p_\infty(t)}{\rho_L}. \tag{2.4.1}$$

Here u_n is the liquid velocity normal to the interface. The reason for rewriting the equation in this form is that the right-hand side now expresses the Lagrangian time rate of change of the potential following the interface in the normal direction. Integration of this equation in time gives therefore the new value of the potential at each new position of the interface and, therefore, by differentiation, the tangential velocity field of the liquid at the bubble surface. To calculate the normal velocity u_n use is made of Green's identity adapted to the present axisymmetric situation:

$$\phi\mathbf{x},t) = \int_S (Gu_n - H\phi)\, ds'. \tag{2.4.2}$$

Here the integration is along the trace S of the bubble surface on a meridian half-plane. The functions G and H are related to elliptic integrals and depend on the field point $\mathbf{x}$ and on the integration point $\mathbf{x}'$. Explicit expressions can be found in Oguz and Prosperetti (1989). Upon choosing the field point $\mathbf{x}$ on the bubble surface, Eq. (2.4.2) is treated as an integral equation for u_n, given that ϕ is known from integrating (2.4.1).

The numerical procedure used to execute a time step can be summarized as follows:

1. The potential on the bubble surface is updated by the explicit one-step Euler method using (2.4.1)
2. The velocity normal to the surface is then evaluated from (2.4.2)
3. With this velocity field the bubble surface is displaced using (2.1.3), again with the explicit one-step Euler method
4. An orthogonal grid is generated inside the bubble; an example is shown in Fig. 21.
5. The Laplace (2.1.17) and energy (2.1.24) equations are discretized on the orthogonal grid by centered finite differences and the resulting system, including the pressure equation (2.1.20), is solved iteratively.

Unfortunately, this numerical scheme suffers from a weakness in that, as is clear from Fig. 21, the orthogonal grid possesses a singularity near the bubble center. As a consequence of this, the aspect ratio of the grid cells changes dramatically as one moves from the bubble surface inward. It is well known that this situation adversely affects accuracy and, as a matter of fact, here the scheme breaks down when the bubble starts getting involuted with the formation of a jet directed toward the plane wall. This circumstance requires a different approach that will be described in the next section.

Nevertheless the method gives good results in the early stages of the bubble collapse, some of which are shown in Figs. 22 and 23. Here the initial bubble radius is 1 mm and the pressure step $\Delta p = 10$ bars. A rigid boundary is located initially 1.2 radii below the bubble center. The left part of Fig. 22 shows the gas isotherms. The expected boundary layer structure of the temperature field is evident here. A further illustration of this feature of the temperature distribution is provided in Fig. 23 that shows the temperature distribution along a line connecting the "south" to the "north pole" of the bubble. The gas temperature is essentially uniform in the core, and falls abruptly to the liquid temperature in thin transition layers near the boundary. The right part of Fig. 22 shows lines of equal Φ for the same case. It can be seen that this function is very regular. These graphs refer to the time $t/t_R = 0.92$.

We exploit this concentration of isotherms near the boundary to formulate an approximate calculation scheme that we now describe.

2.5 Non-Spherical Collapse – Boundary Layer Approximation

The very abrupt change of the temperature field near the bubble boundary shown in Fig. 23, coupled with the smooth variation of the field Φ, suggests to approximate the energy equation (2.1.24) in a boundary layer fashion.

To this end, we introduce a new coordinate system in which the bubble surface corresponds to the line $x = 0$ while the y = constant lines are normal to the surface. In the immediate vicinity of the surface these coordinate lines are very nearly orthogonal. In this system, the energy equation (2.1.24) is, omitting conduction in the tangential direction,

$$\frac{\partial \tau}{\partial t} + (v_x - V_x)\frac{\partial \tau}{\partial x} + (v_y - v_{y0})\frac{\partial \tau}{\partial y} = -D\dot{p} + D\frac{\partial^2 \tau}{\partial y^2}. \tag{2.5.1}$$

Here τ is the auxiliary temperature variable defined in (2.2.8) and $D = K/(C_p \rho_G)$ is the gas thermal diffusivity. Furthermore, the term V_x is the grid velocity in the tangential direction and v_{y0} is the bubble surface normal velocity. From (2.1.18) we have

$$v_y - v_{y0} = -\frac{\dot{p}}{3\gamma p} y + \frac{\gamma - 1}{\gamma p}\left(\frac{\partial \tau}{\partial y} - \left.\frac{\partial \tau}{\partial y}\right|_{y=0}\right) + \frac{\partial \Phi}{\partial y} - \left.\frac{\partial \Phi}{\partial y}\right|_{y=0}. \tag{2.5.2}$$

In view of the smooth variation of Φ in the vicinity of the bubble wall (see Fig. 22) the last two terms can be simplified by means of a Taylor series expansion:

$$\begin{aligned} \frac{\partial \Phi}{\partial y} - \left.\frac{\partial \Phi}{\partial y}\right|_{y=0} &\simeq \left.\frac{\partial^2 \Phi}{\partial y^2}\right|_{y=0} y \\ &= -\left(\frac{\partial^2 \Phi}{\partial x^2} + \frac{1}{R_x}\frac{\partial \Phi}{\partial y} + \frac{1}{R_y}\frac{\partial \Phi}{\partial y}\right) y, \end{aligned} \tag{2.5.3}$$

where R_x and R_y are the radii of curvature of the surfaces x = const. and y =const calculated from the computed surface shape. The step from the first to the second line is due to the fact that $\nabla^2 \Phi = 0$.

The numerical solution procedure is the same as in the previous section, except for the fact that no grid is generated numerically and only an algebraic stretching is introduce to increase the node density near the surface.

This boundary layer approximation has been compared with the full model results for the spherical case and for the asymmetric case up to the point of jet formation with excellent results. A typical comparison for the spherical case is shown in Fig. 24 where the dashed line is the gas center temperature according to the full model and the solid line the boundary layer approximation. A comparison for the asymmetric case is shown in Fig. 25 that shows the heat fluxes at the jet tip predicted by the full model (dashed line) and by the boundary layer approximation (solid line) for the case of Figs. 21 to 23.

2.6 Non-Spherical Collapse – Some Results

Figure 26 shows successive bubble configurations for collapse induced by a sudden overpressure, Eq. (2.3.5), with $\Delta p = 10$ bars, $p_0 = 1$ bar. Here the initial bubble radius is $R_0 = 1$ mm and the rigid wall is initially 1.2 mm below the bubble center. Successive bubble shapes for the excitation by the pressure pulse (2.3.1) with $t_R/t_p = 4$ are shown in Fig. 27. The peculiar shape of the free surface in this case is due to the fact that, once formed, the jet continues its motion toward the opposite wall even after the rest of the cavity has started to rebound.

Figure 28 shows the local heat flux along the bubble surface for the step pressure increase $\Delta p = 10$ bars as computed from the boundary-layer model as a function of time. The abscissa in this figure denotes the

node number. Sixty equispaced nodes were used. The heat flux is fairly uniform over the surface until the jet forms. At this point the region near the jet tip starts absorbing heat considerably faster than other regions. Just before the jet strikes the other side of the bubble, the heat flux at the tip is calculated to reach more than 300 MW/m^2!

In this case we were unable to calculate directly the temperature in the liquid to find the temperature at the bubble surface. Hence, we use the following approximation. At the jet tip, the flow is only in the direction normal to the axis, and in the immediate vicinity of the tip (which is the only region where there are appreciable temperature gradients) is very nearly solid body. In a frame of reference moving with the tip, therefore, the liquid energy equation is therefore essentially the pure conduction equation. Furthermore, conduction in the direction tangent to the surface is very likely much slower than in the thin boundary layer normal to the surface. These considerations satisfy solving, on the tip axis, the equation

$$\frac{\partial T_L}{\partial t} = D_L \frac{\partial^2 T_L}{\partial y^2}, \tag{2.6.1}$$

subject to continuity of the normal heat fluxes. Even aside from the previously described approximations this procedure is not strictly correct as the gas energy equation is solved assuming that the liquid temperature is undisturbed. However the gas heating is so large that it is unlikely that accounting for the liquid surface heating would affect the gas temperature field very much.

In this way we can estimate the liquid temperature at the jet tip as a function of time. Results for the case of Fig. 26 are shown in Fig. 29 (solid line). In this figure the dashed line is the liquid temperature fr the corresponding spherical case.

2.7 Conclusions on Bubble Collapse

We have presented results for the gas and liquid temperatures attained during the collapse of gas bubbles exposed to pressure pulses and steps. The main conclusions are as follows:

1. The ratio between the characteristic time for the collapse (the Rayleigh time) t_R and the duration of the pressure pulse t_p has emerged as a very significant parameter. When this ratio is close to 1 the gas temperature reaches very high values. When the pressure pulse amplitude is 100 bars and t_p/t_R = 1 our computations give peak liquid temperatures of the order of 1500 K for bubble radii between 0.1 and 10 mm. The duration of these large temperatures is however very short, most likely too short to result in ignition. Furthermore, it may be assumed that, under these conditions, phase change will occur at the bubble wall with a corresponding decrease in temperature.

2. We have also studied the response of a spherical bubble to a pressure step. In this case the bubble executes a series of free oscillations of decreasing amplitude. As before, we find large liquid temperatures at the bubble surface, especially during the first collapse that is the most violent one. These temperatures are the larger the smaller the liquid thermal conductivity. Also, other things being equal, a monatomic gas gets hotter than a diatomic one due to the higher adiabatic index, with a corresponding greater liquid temperature. On the basis of these previous considerations, one may perhaps postulate a **new mechanism for ignition**: upon the first collapse, the bubble surface heats up considerably and part of the liquid vaporizes into the bubble core. Upon subsequent collapses this vapor is exposed to very large temperatures, much larger than the liquid at the bubble surface, and ignites. Whether this mechanism is possible cannot be decided on the basis of the current model that does not include phase change processes. An extension in this direction should however be feasible.

3. All of the previous conclusions have been reached assuming that the bubble maintains a spherical symmetry. This is actually rather unlikely in view of the well-known instability of the spherical shape. For this reason, and also to simulate the effect of nearby boundaries, we have formulated a model capable of handling axisymmetric collapses. This model is considerably more complex than the symmetric one and only a limited exploration of its predictions has been possible whithin the time span of this grant.

Nevertheless, as shown in Fig. 29, we find that the liquid microjet that penetrates the bubble as a result of the instability is exposed to much higher temperatures than in the spherical case, although again the duration of these high temperatures is very short. Experimental evidence does indicate that ignition, when it occurs, seems to be related (at least in time) to the impact of the microjet on the other side of the bubble wall. It is not clear however whether this is the result of the microjet heating up, or of the fact that the collapse continues even after the impact of the microjet, and that the maximum compression (and therefore the strongest heating) immediately follows the microjet impact. This circumstance is really accidental, in the sense that it is only due to the fact that the microjet takes a very long time to develop.

4. All of the results that we have found indicate that ignition is in principle possible, although marginally so. This finding may explain why it is difficult to deduce definite conclusions from the available experimental evidence with its apparently inconsistent results.

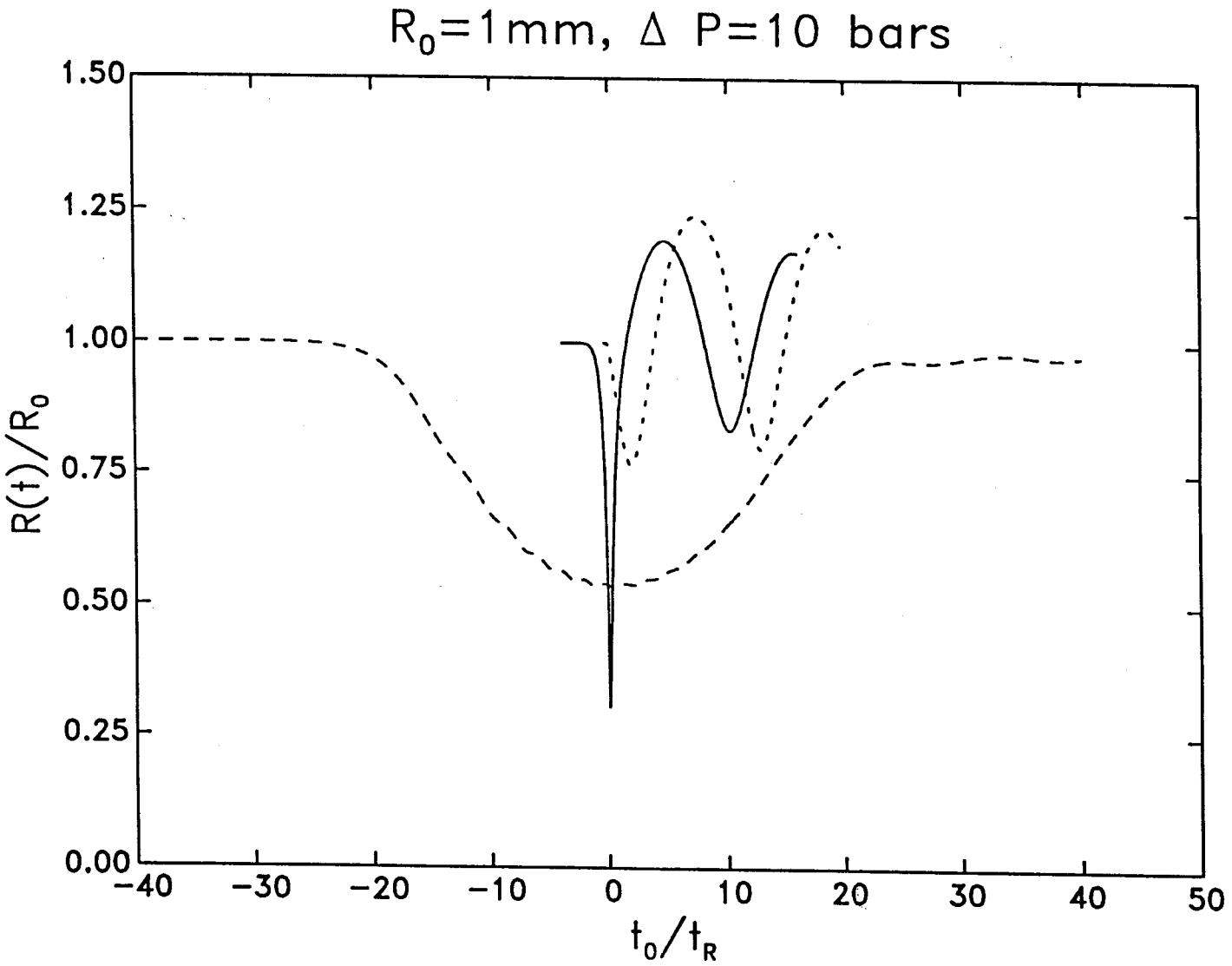

Fig. 1. Normalized radius R/R_0 versus the normalized time t/t_R [where $R_0 = 1$ mm is the initial radius and t_R is the Rayleigh collapse time defined in (2.3.2)] for an air bubble subject to Gaussian compression pulse of width t_p. The dashed line is for $t_R/t_p = 0.1$, the solid line for $t_R/t_p = 1$, and the dotted line for $t_R/t_p = 10$. The initial pressure is 1 bar, the maximum overpressure 10 bars, and $t_R \simeq 29$ μs.

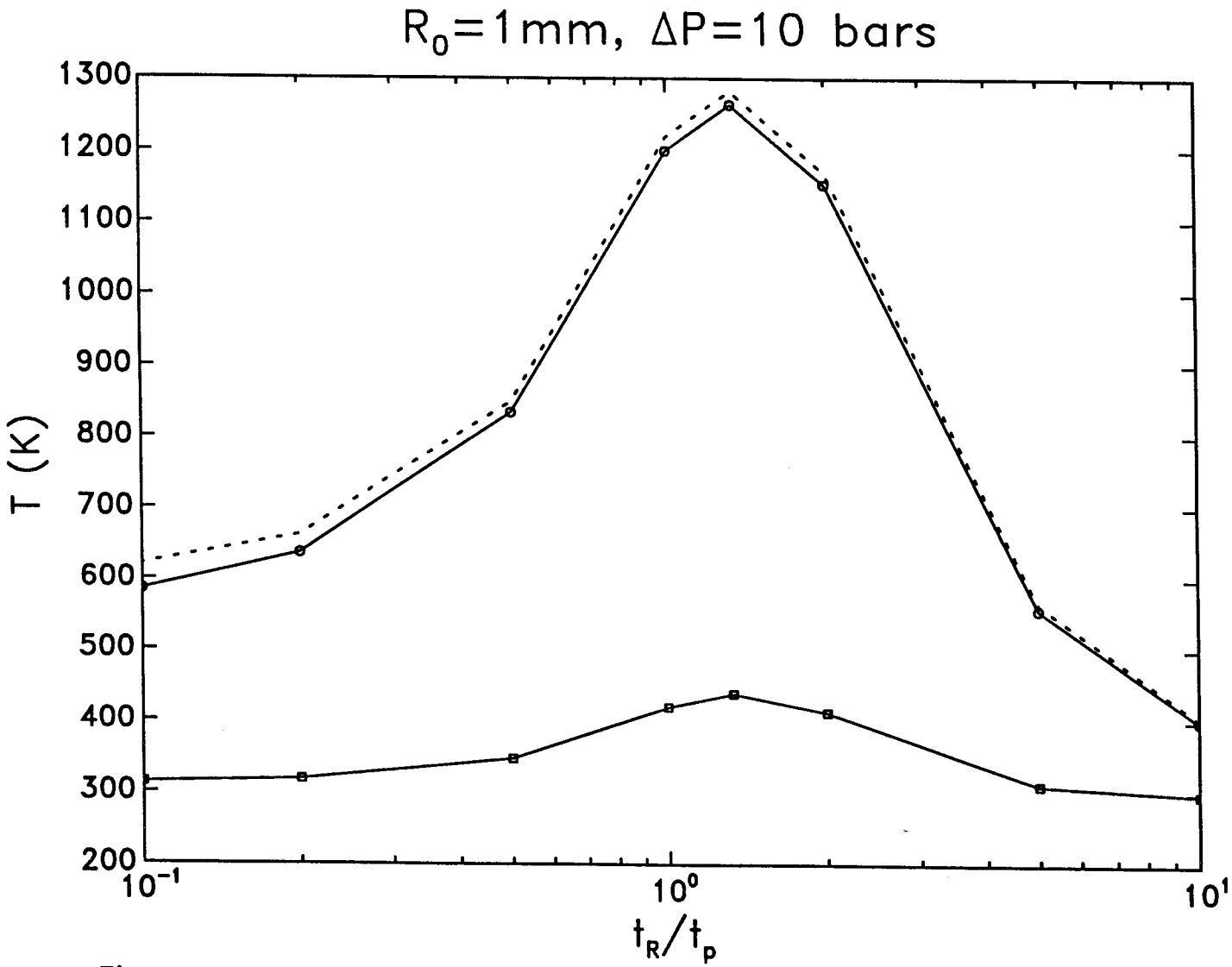

Fig. 2. Temperature attained by the gas at the bubble center (squares) and by the liquid at the bubble surface (circles) at the end of the first collapse for t_R/t_p = 0.1, 0.2, 0.5, 1, 2, 5, and 10. The dotted line is the adiabatic prediction. The collapse is caused by a Gaussian pressure pulse with width t_p and maximum amplitude 10 bars. The initial bubble radius is 1 mm and the initial ambient pressure 1 bar.

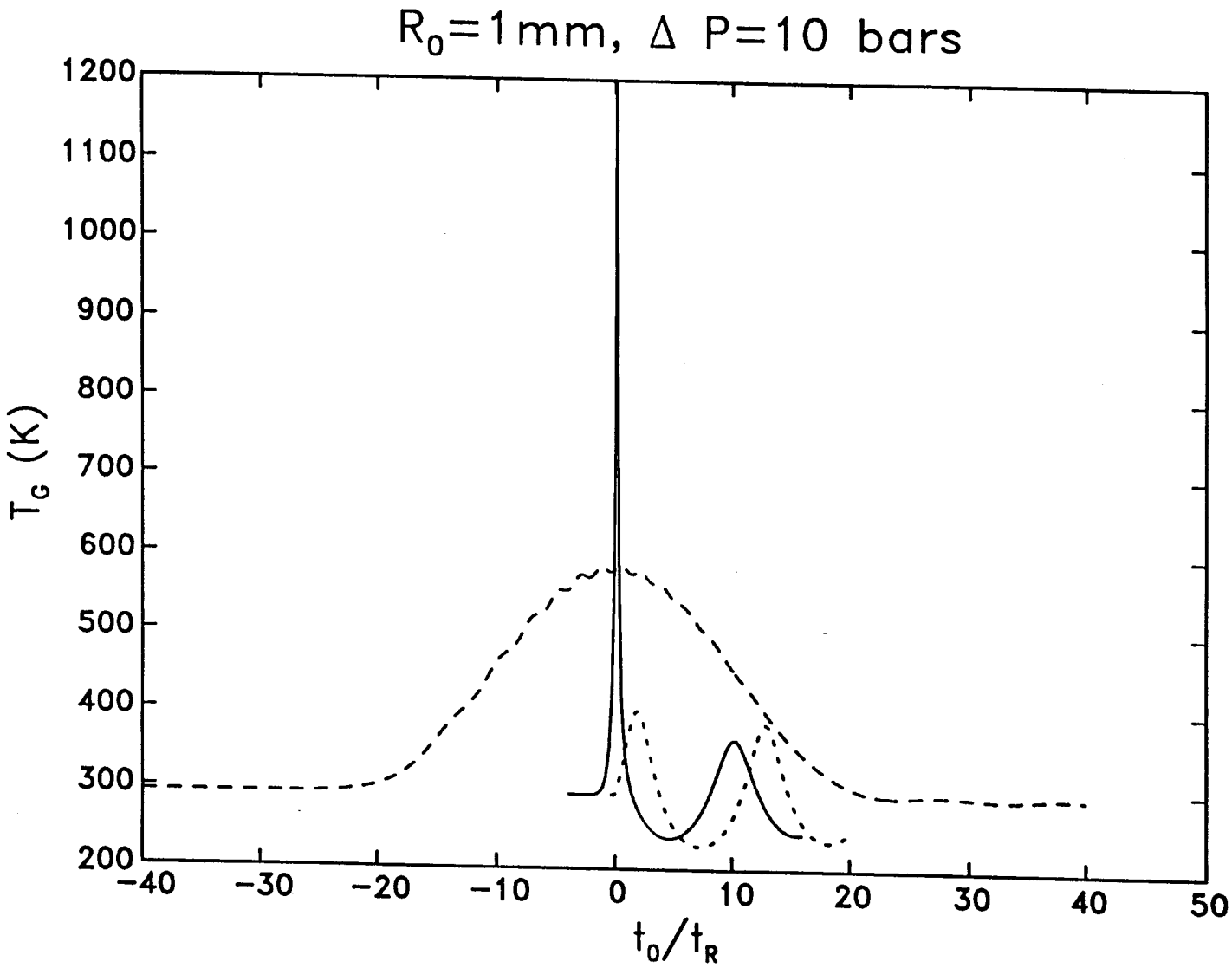

Fig. 3. Center gas temperature for the three cases of Fig. 1 as a function of t/t_R. The dashed curve is for $t_R/t_p = 0.1$, the solid one for $t_R/t_p = 1$, and the dotted one for $t_R/t_p = 10$.

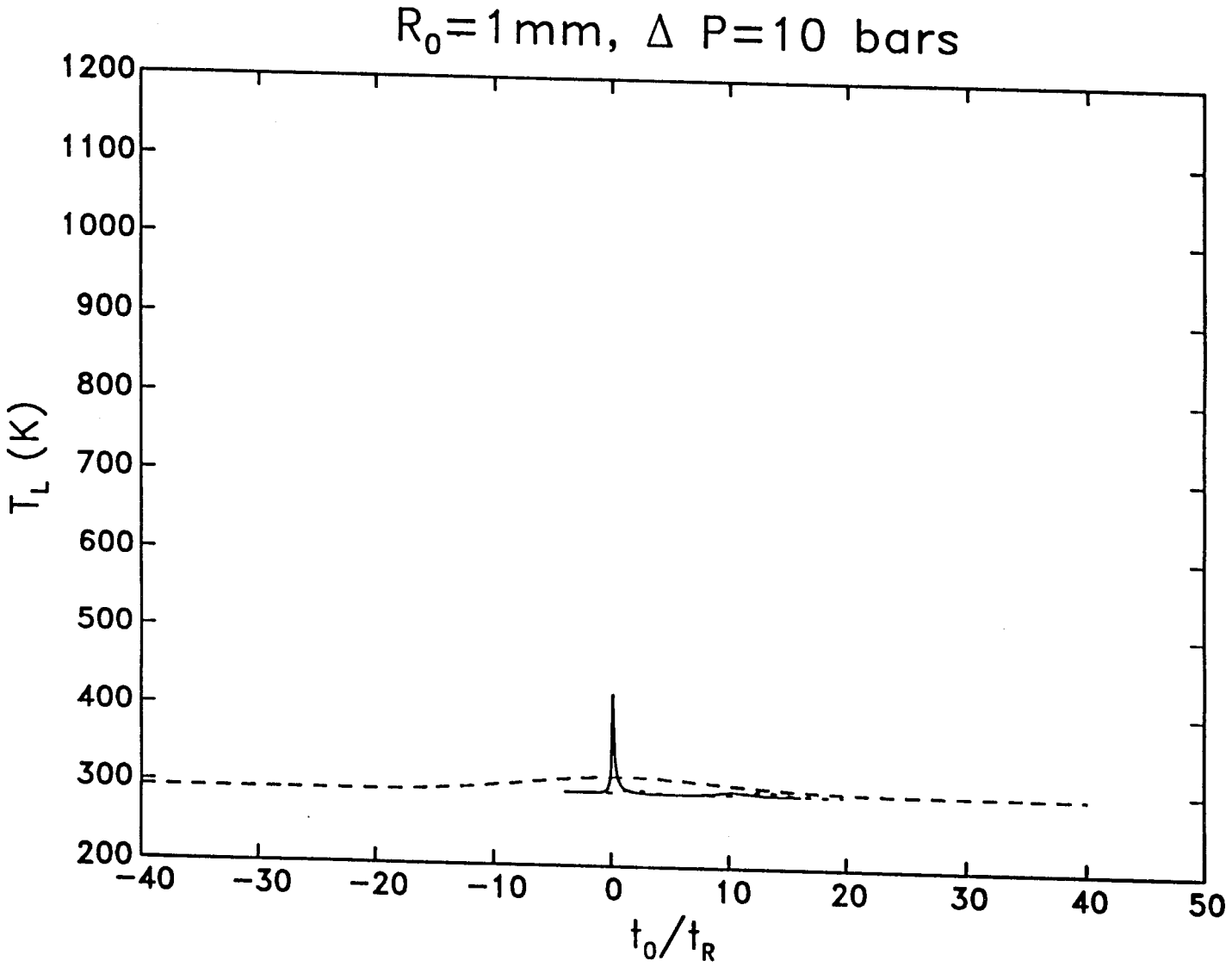

Fig. 4. Liquid surface temperature for the three cases of Fig. 1 as a function of t/t_R. The dashed curve is for $t_R/t_p = 0.1$, the solid one for $t_R/t_p = 1$, and the dotted one for $t_R/t_p = 10$.

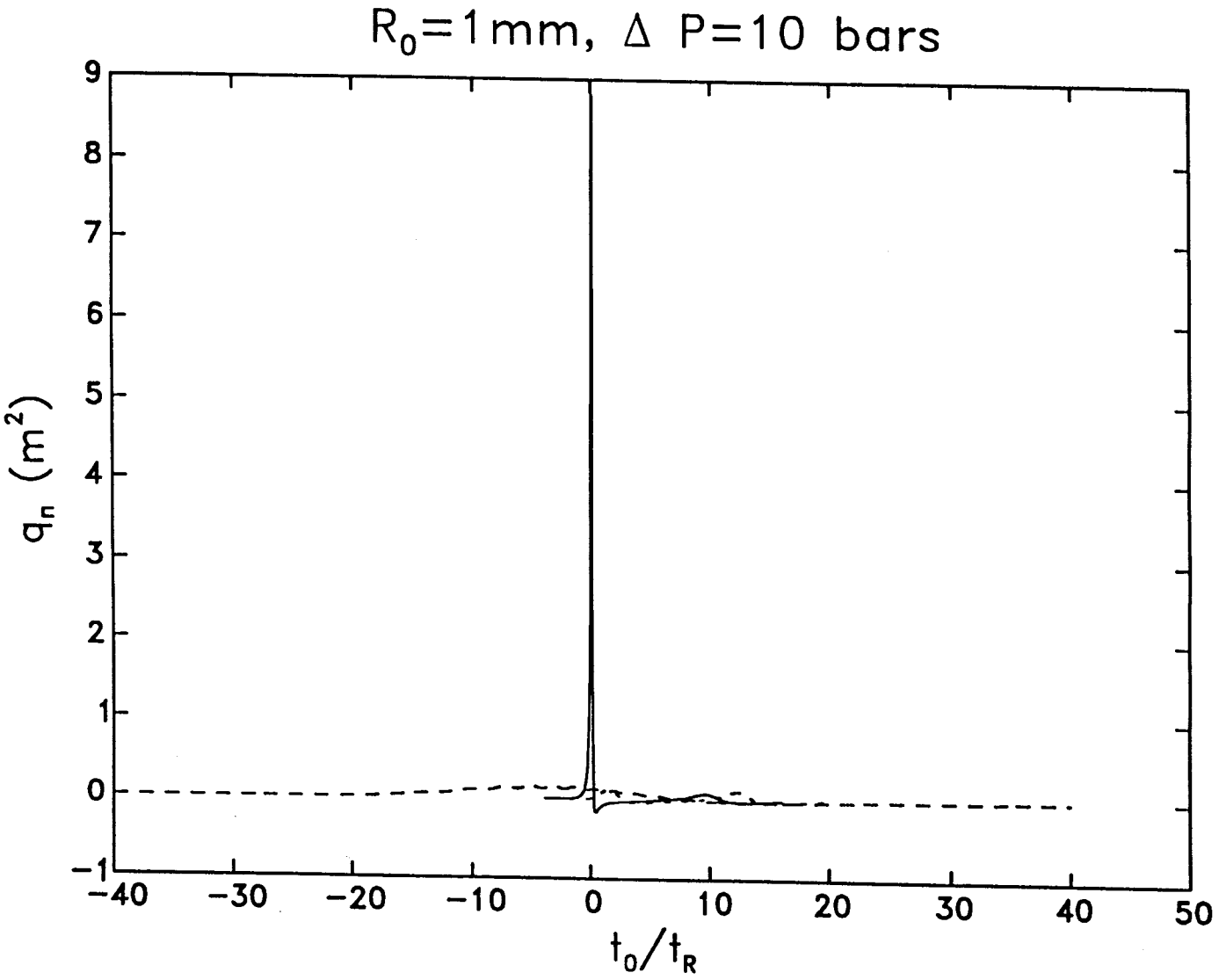

Fig. 5. Wall heat fluxes for the three cases of Fig. 1 as a function of t/t_R. The dashed curve is for $t_R/t_p = 0.1$, the solid one for $t_R/t_p = 1$, and the dotted one for $t_R/t_p = 10$.

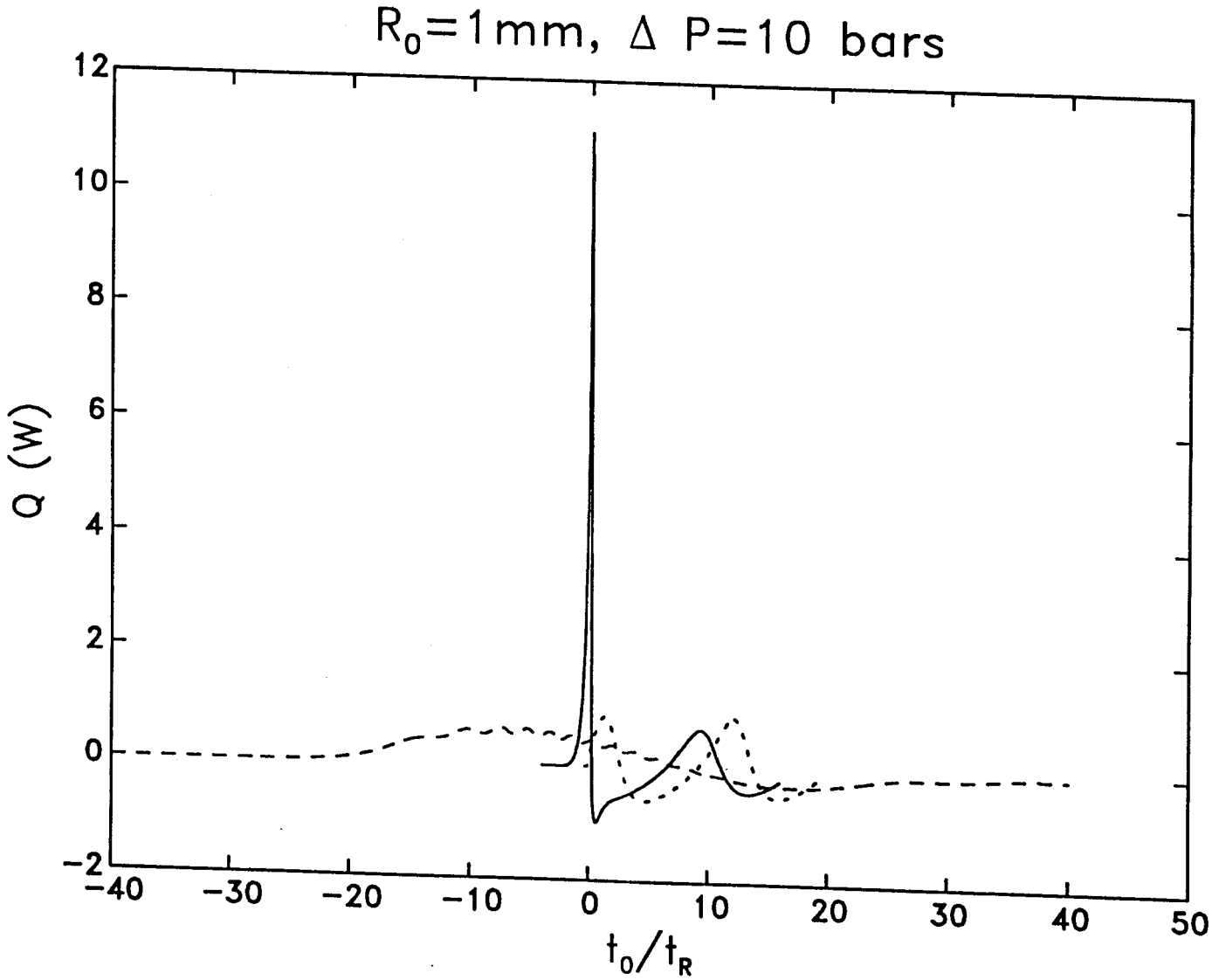

Fig. 6. Amount of heat delivered to the liquid (2.3.4) as a function of time for the three cases of Fig. 1. The dashed curve is for $t_R/t_p = 0.1$, the solid one for $t_R/t_p = 1$, and the dotted one for $t_R/t_p = 10$.

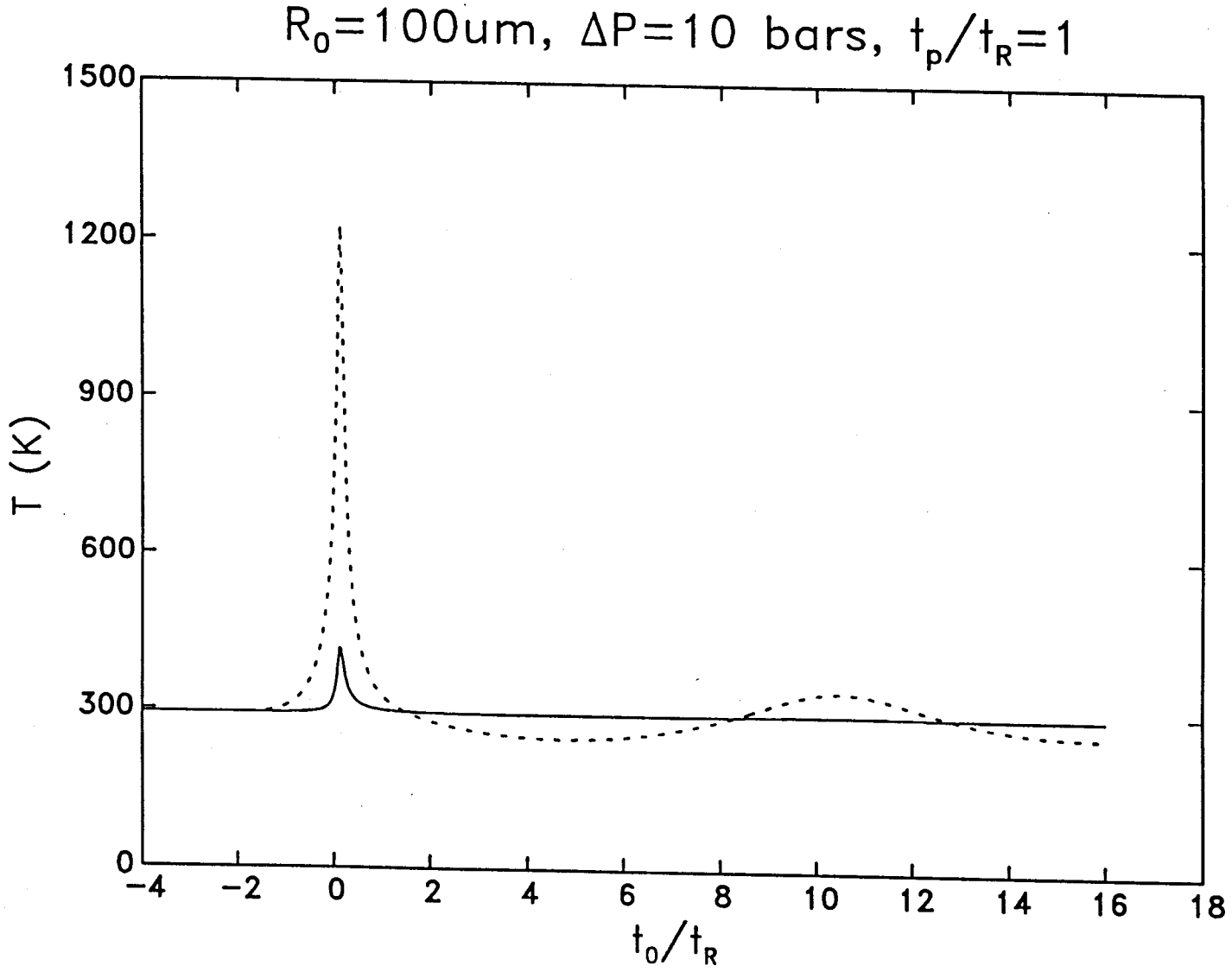

Fig. 7. Core gas (dashed) and bubble surface (solid) temperatures for $t_R = t_p$, $\Delta p = 10$ bars, and $R_0 = 0.1$ mm. The Rayleigh time is $t_R = 2.9$ μs.

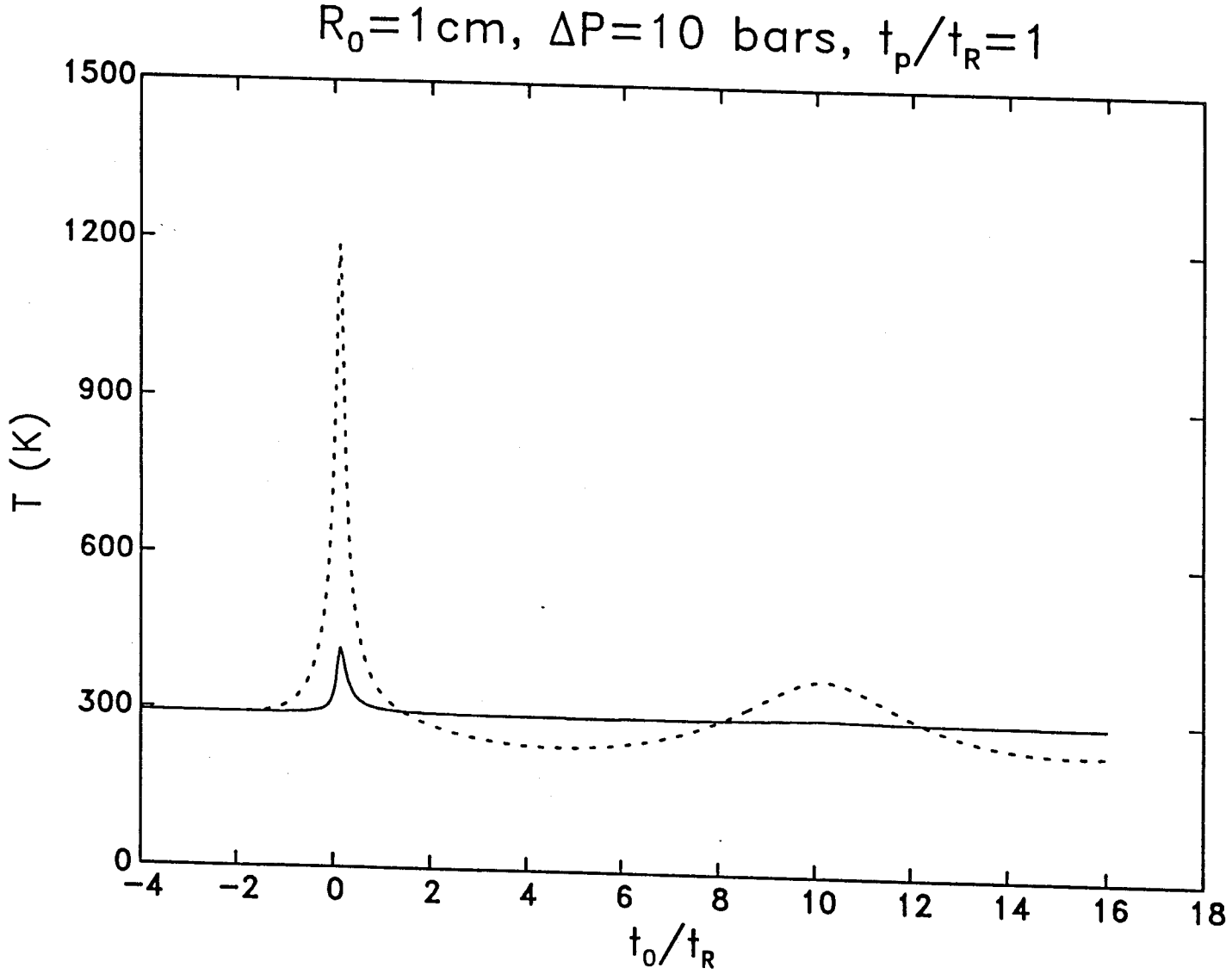

Fig. 8. Core gas (dashed) and bubble surface (solid) temperatures for $t_R = t_p$, $\Delta p = 10$ bars, and $R_0 = 10$ mm. The Rayleigh time is $t_R = 0.29$ ms.

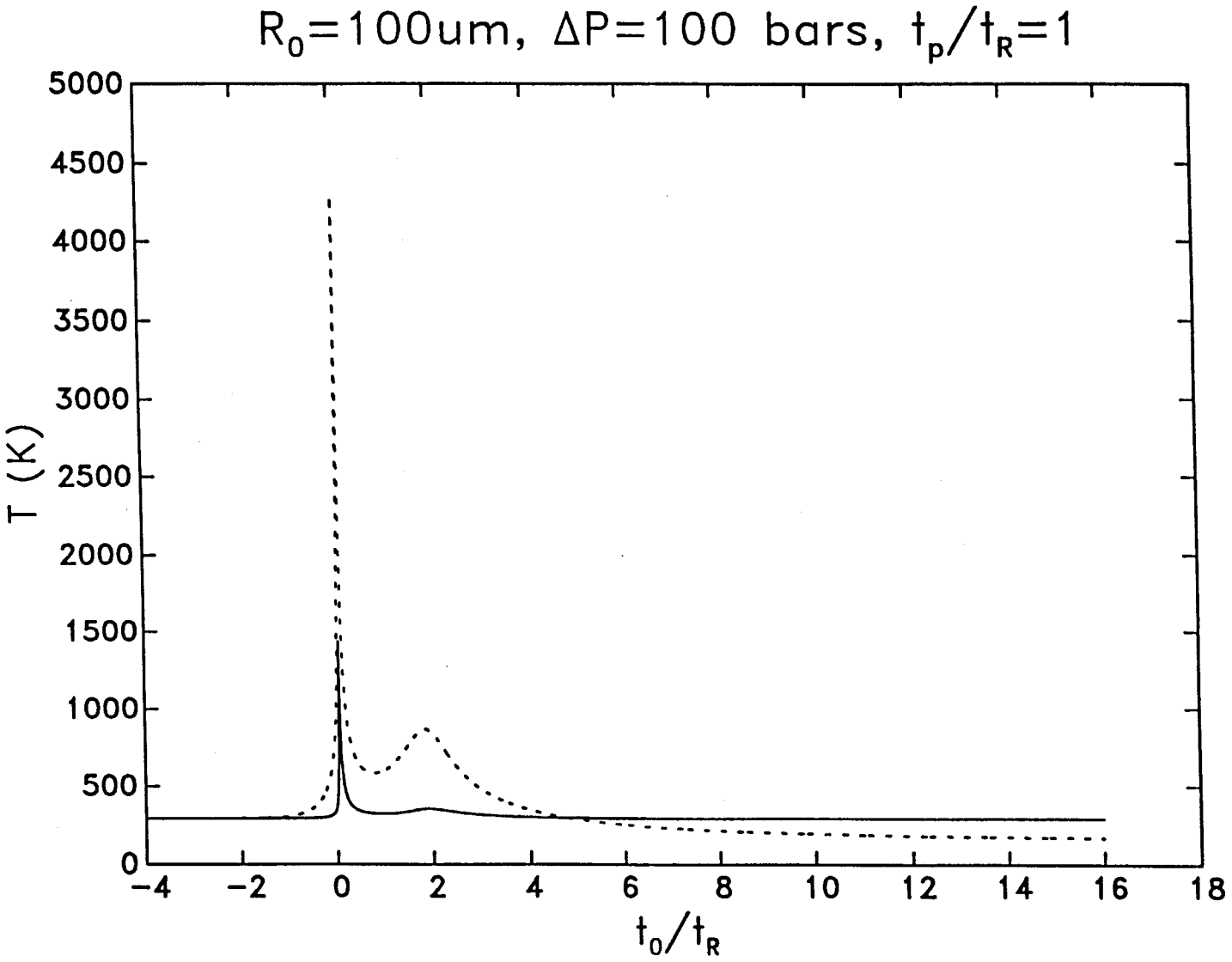

Fig. 9. Core gas (dashed) and bubble surface (solid) temperatures for $t_R = t_p$, $\Delta p = 100$ bars, and $R_0 = 0.1$ mm. The Rayleigh time is $t_R = 0.92$ μs.

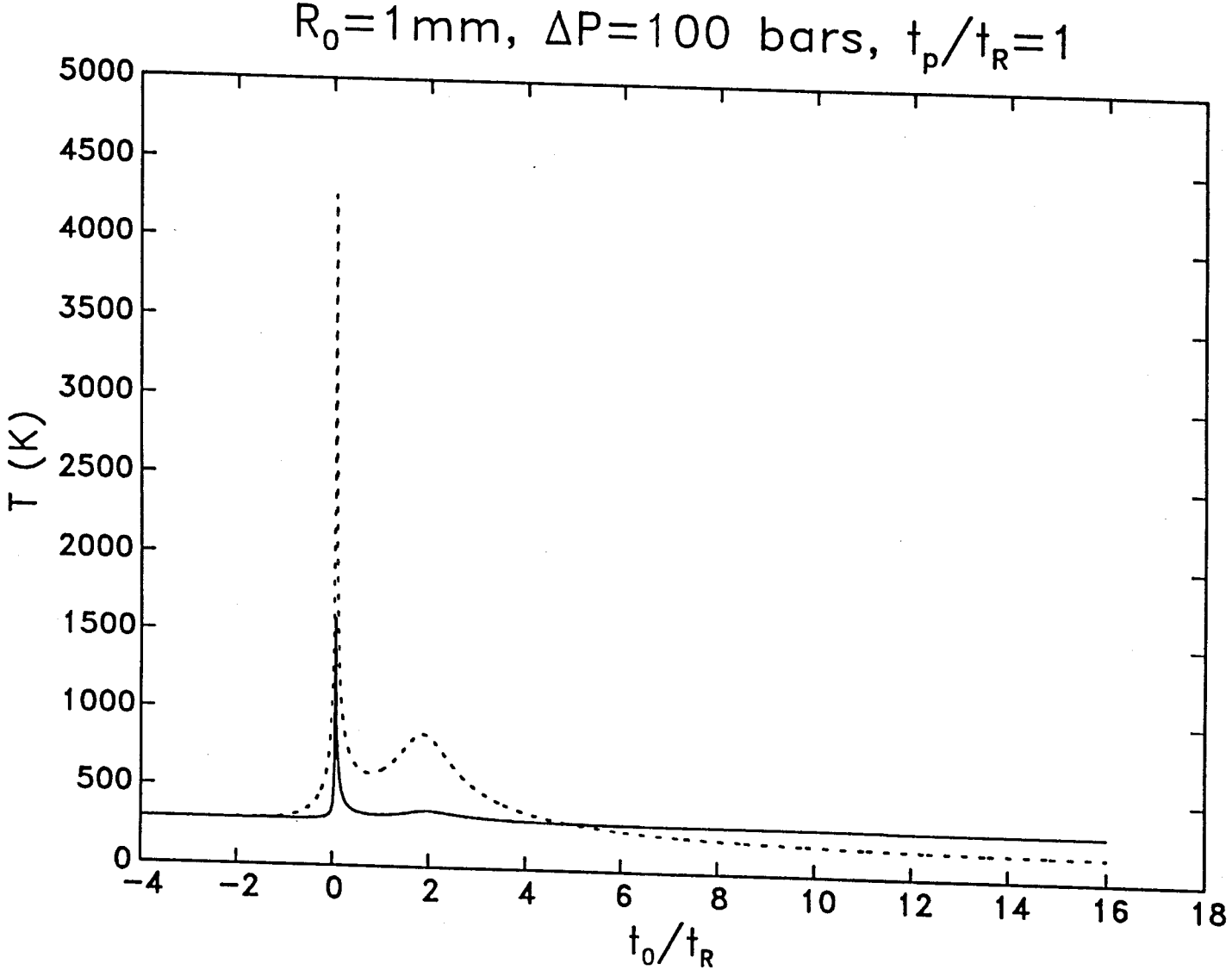

Fig. 10. Core gas (dashed) and bubble surface (solid) temperatures for $t_R = t_p$, $\Delta p = 100$ bars, and $R_0 = 1$ mm. The Rayleigh time is $t_R = 9.2$ μs.

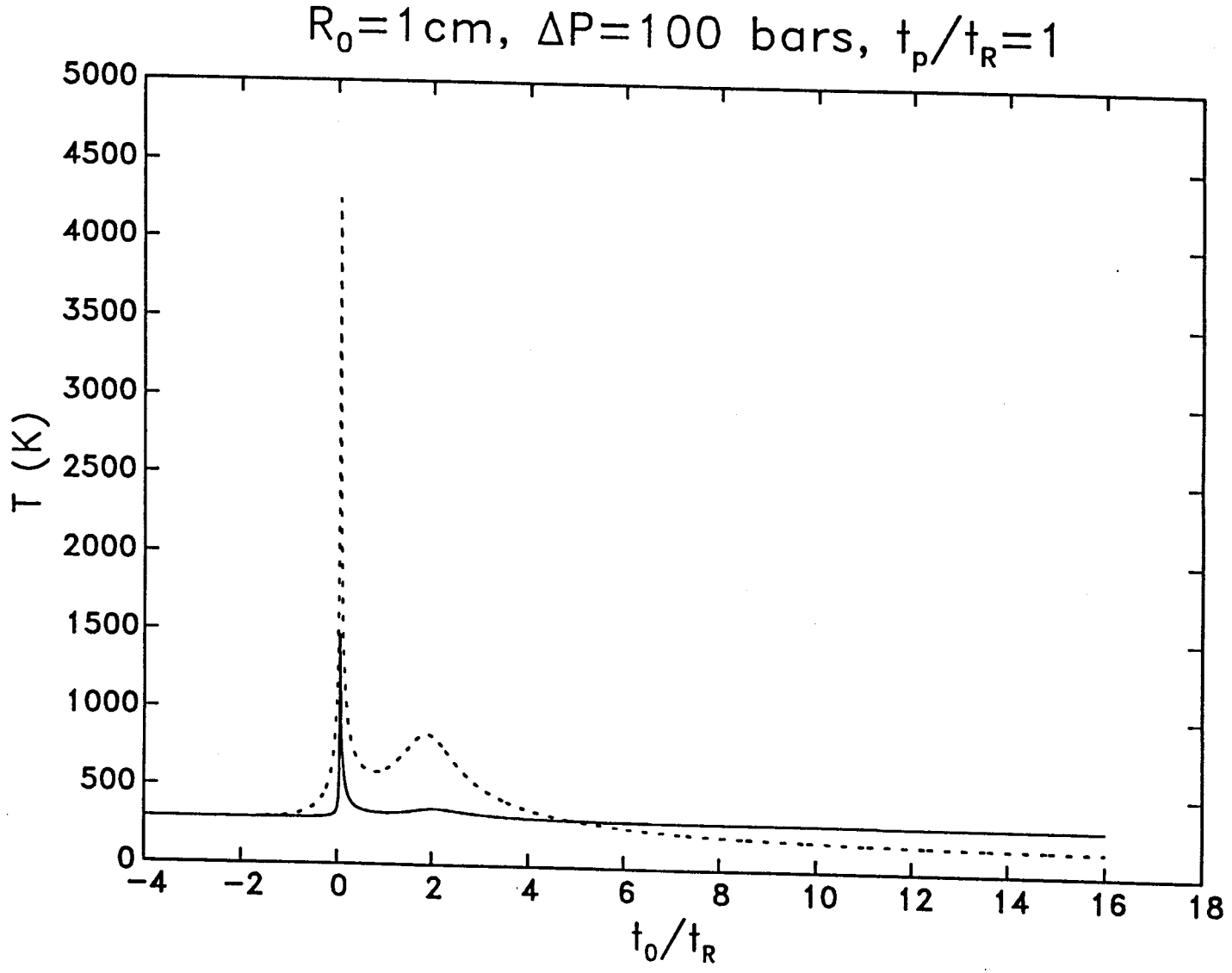

Fig. 11. Core gas (dashed) and bubble surface (solid) temperatures for $t_R = t_p$, $\Delta p = 100$ bars, and $R_0 = 10$ mm. The Rayleigh time is $t_R = 92$ μs.

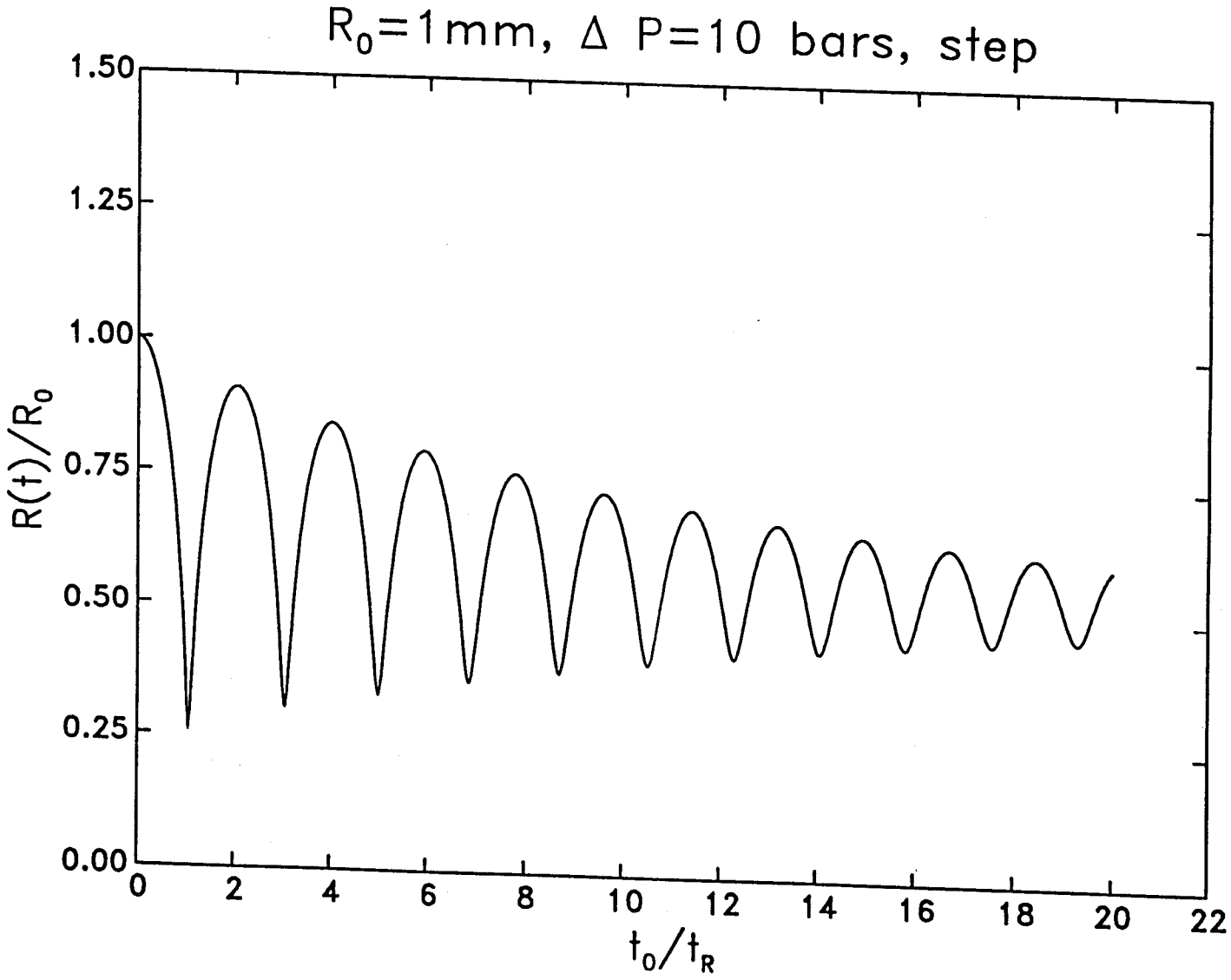

Fig. 12. Normalized radius R/R_0 versus the normalized time t/t_R for an air bubble with initial radius R_0 = 1 mm subject to a step pressure increase Δp = 10 bars. The Rayleigh collapse time is t_R = 29 μs.

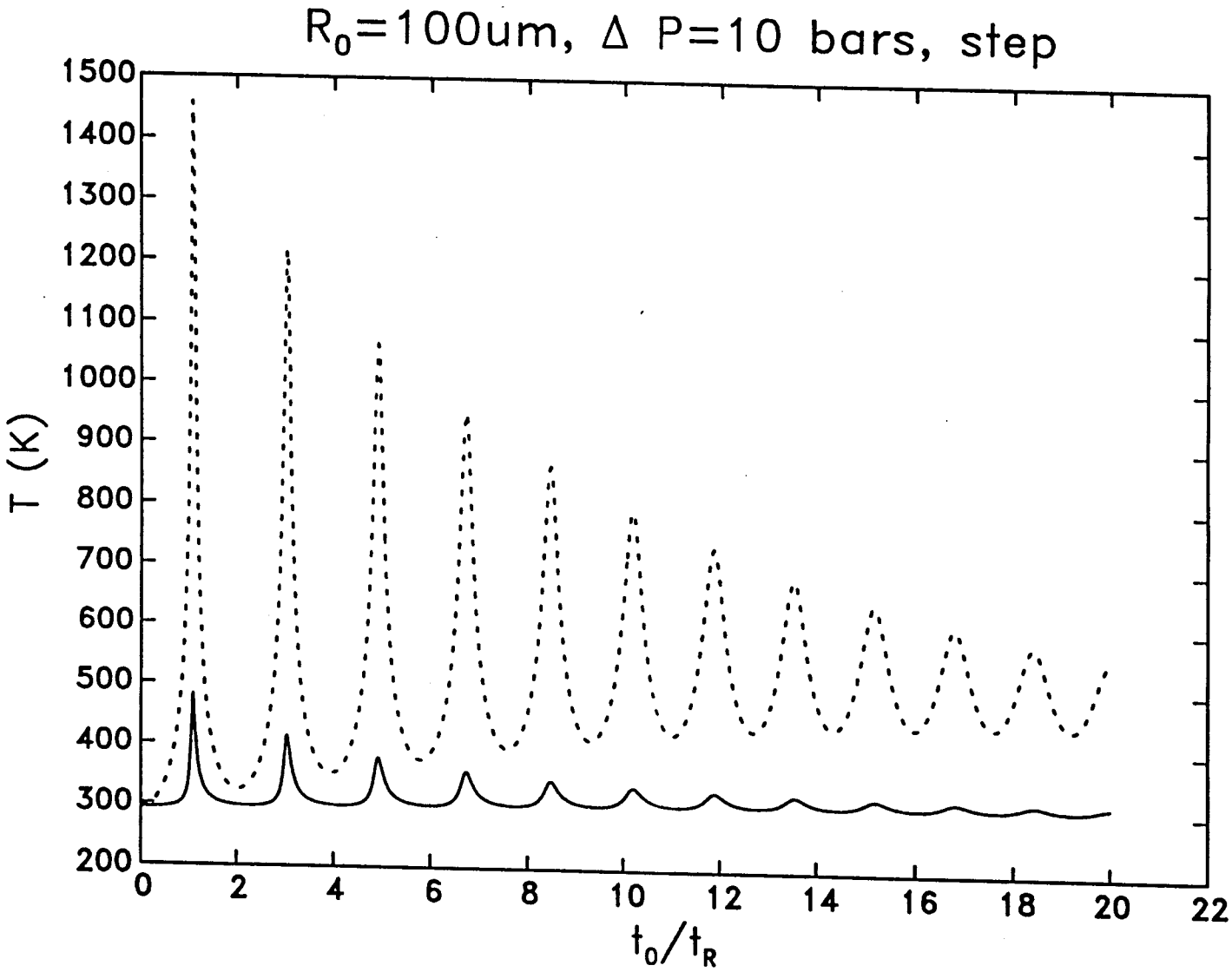

Fig. 13. Core gas (dashed) and bubble surface (solid) temperatures for a step pressure increase with $\Delta p =$ 10 bars and $R_0 = 0.1$ mm. The Rayleigh time is $t_R = 2.9$ μs.

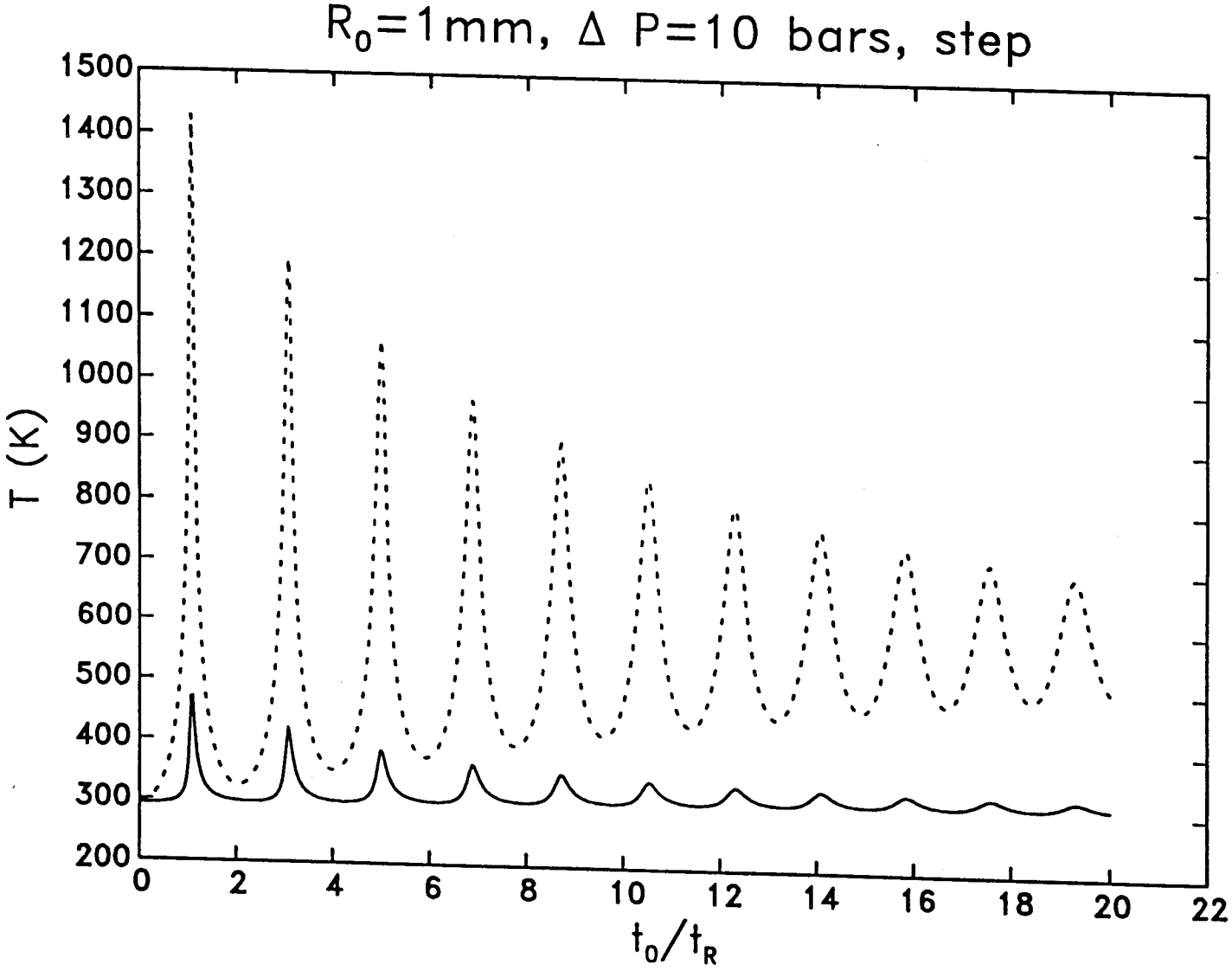

Fig. 14. Core gas (dashed) and bubble surface (solid) temperatures for a step pressure increase with $\Delta p =$ 10 bars and $R_0 = 1$ mm. The Rayleigh time is $t_R = 29$ μs.

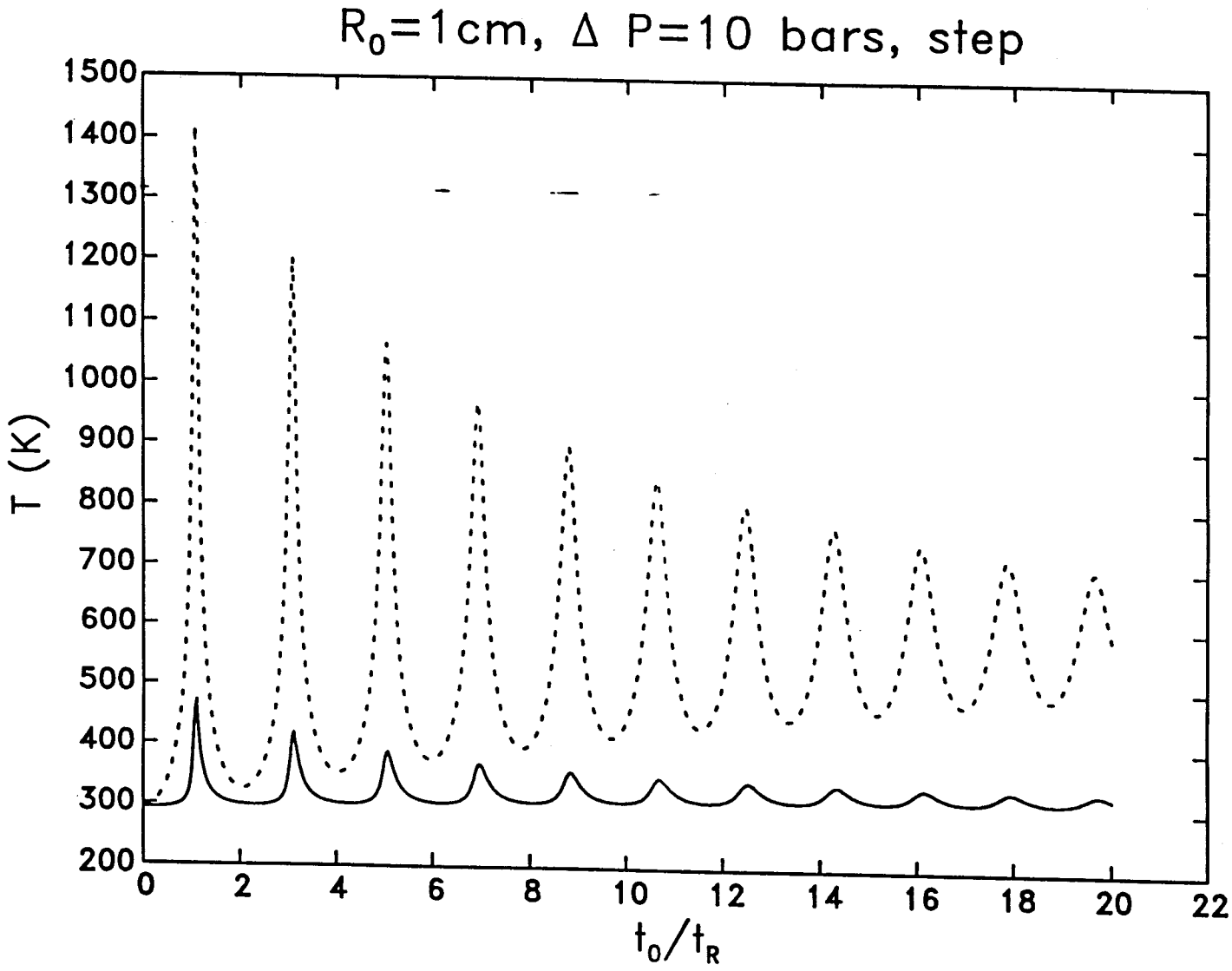

Fig. 15. Core gas (dashed) and bubble surface (solid) temperatures for a step pressure increase with $\Delta p =$ 10 bars and $R_0 = 10$ mm. The Rayleigh time is $t_R = 0.29$ ms.

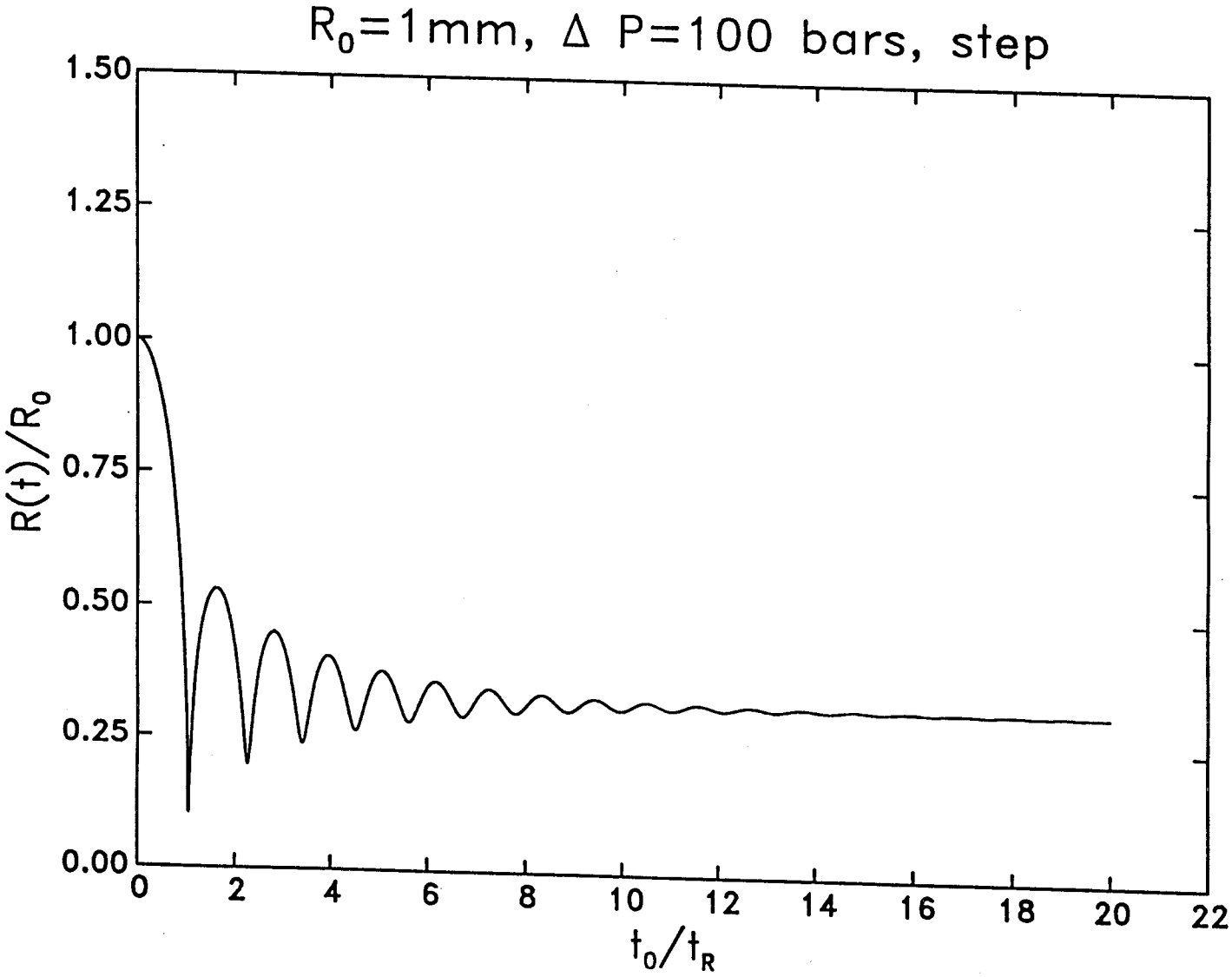

Fig. 16. Normalized radius R/R_0 versus the normalized time t/t_R for an air bubble with initial radius R_0 = 1 mm subject to a step pressure increase Δp = 100 bars. The Rayleigh collapse time is t_R = 9.2 μs.

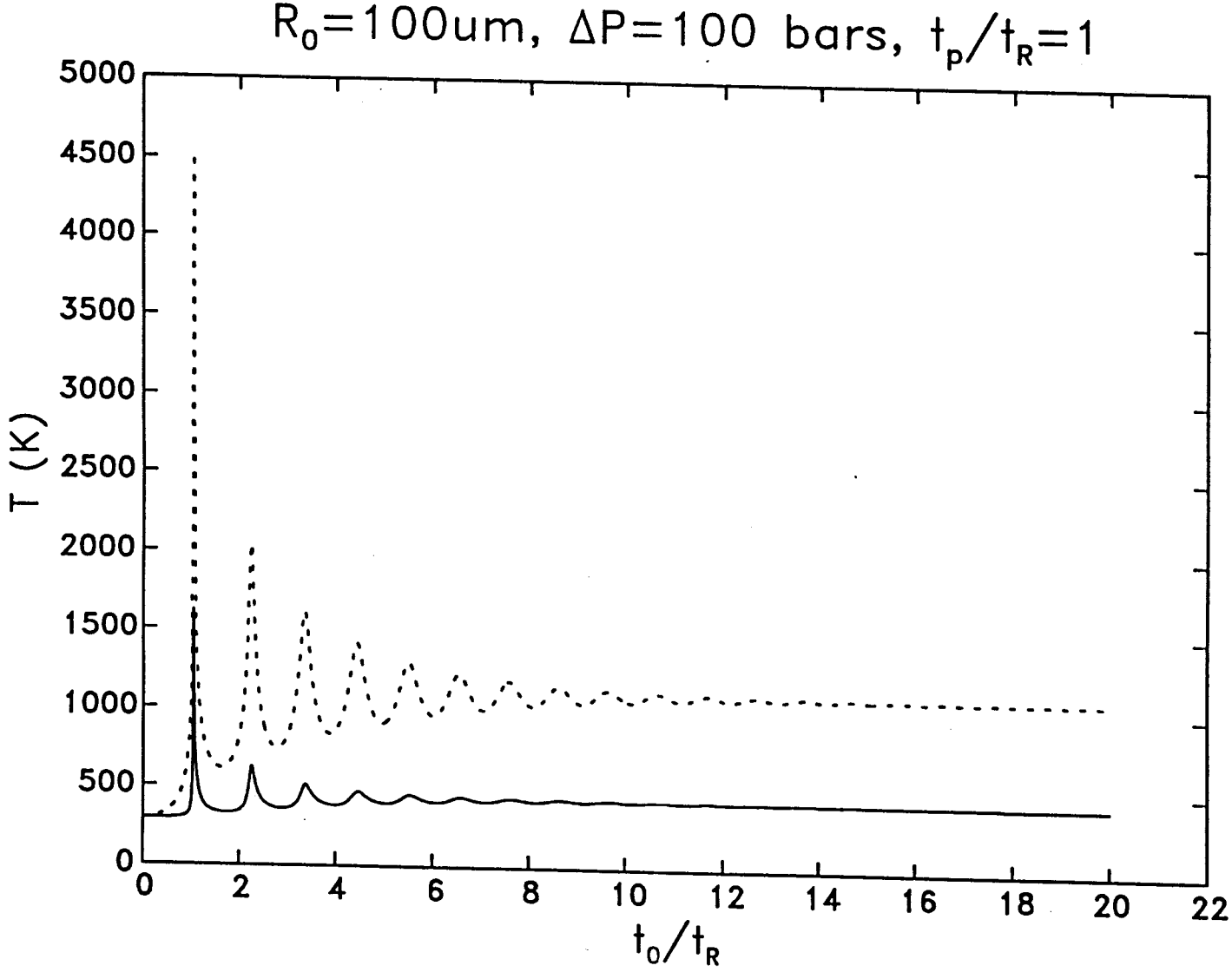

Fig. 17. Core gas (dashed) and bubble surface (solid) temperatures for a step pressure increase with $\Delta p =$ 100 bars and $R_0 = 0.1$ mm. The Rayleigh time is $t_R = 0.92$ μs.

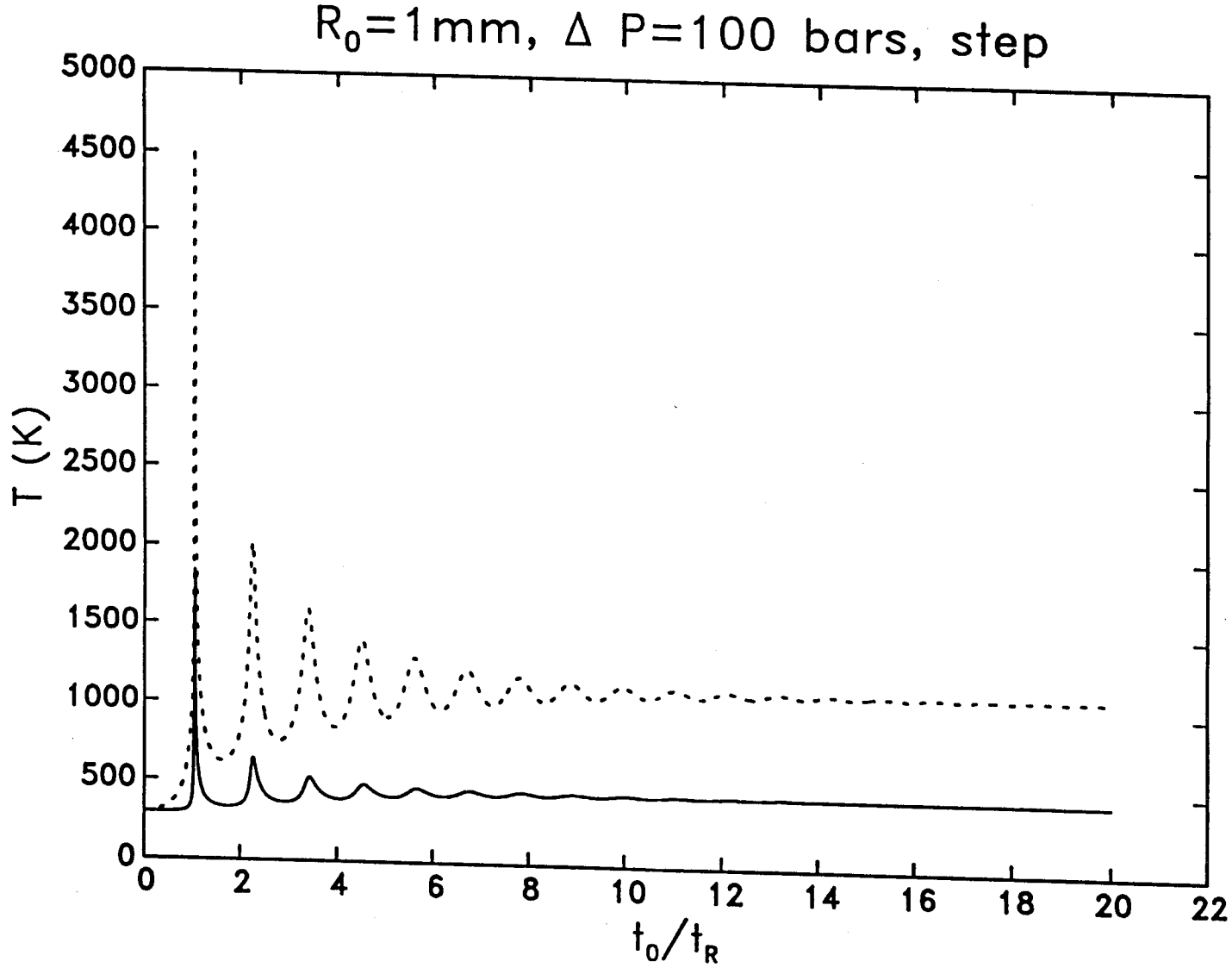

Fig. 18. Core gas (dashed) and bubble surface (solid) temperatures for a step pressure increase with $\Delta p =$ 100 bars and $R_0 = 1$ mm. The Rayleigh time is $t_R = 9.2$ μs.

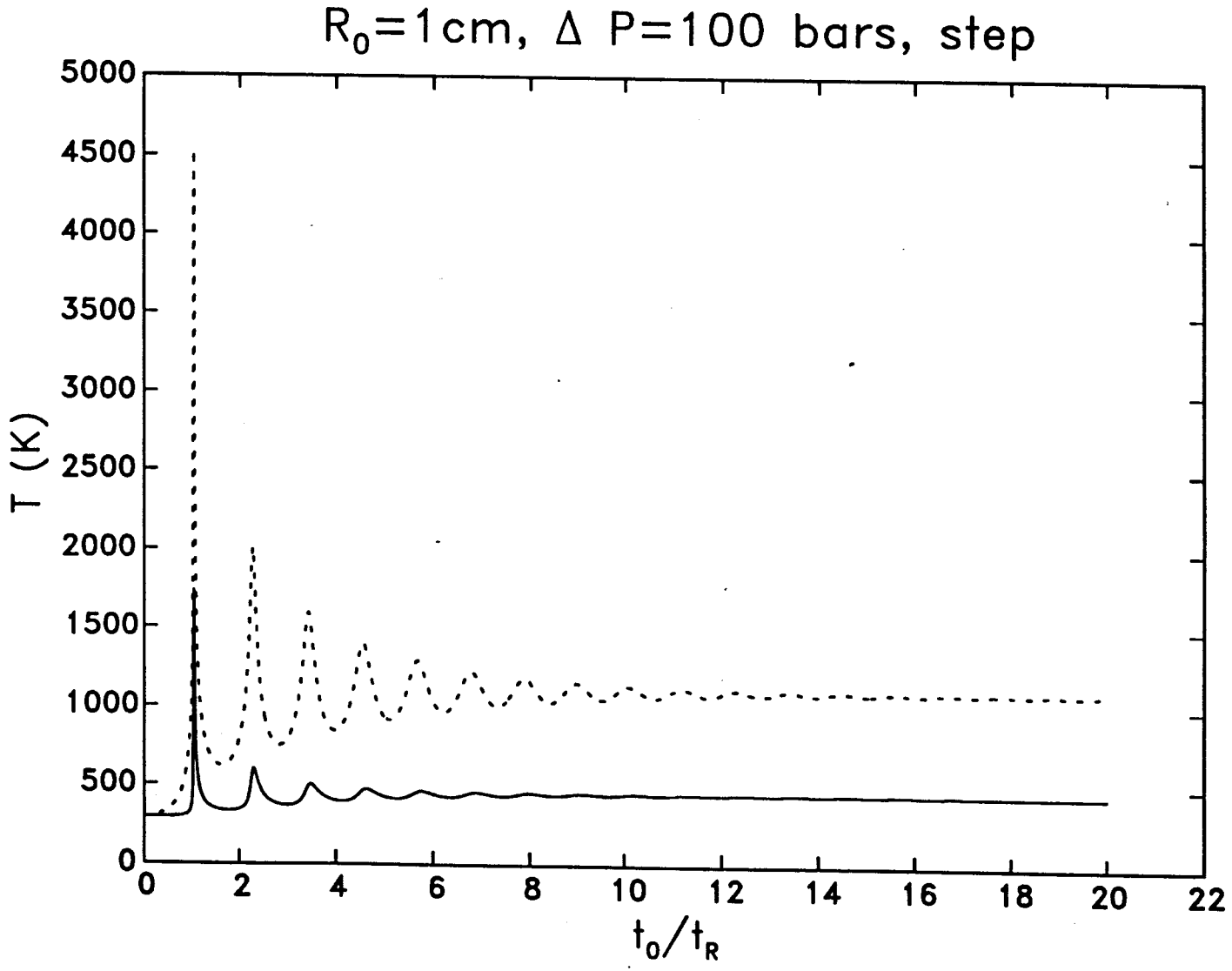

Fig. 19. Core gas (dashed) and bubble surface (solid) temperatures for a step pressure increase with $\Delta p =$ 100 bars and $R_0 = 10$ mm. The Rayleigh time is $t_R = 92$ μs.

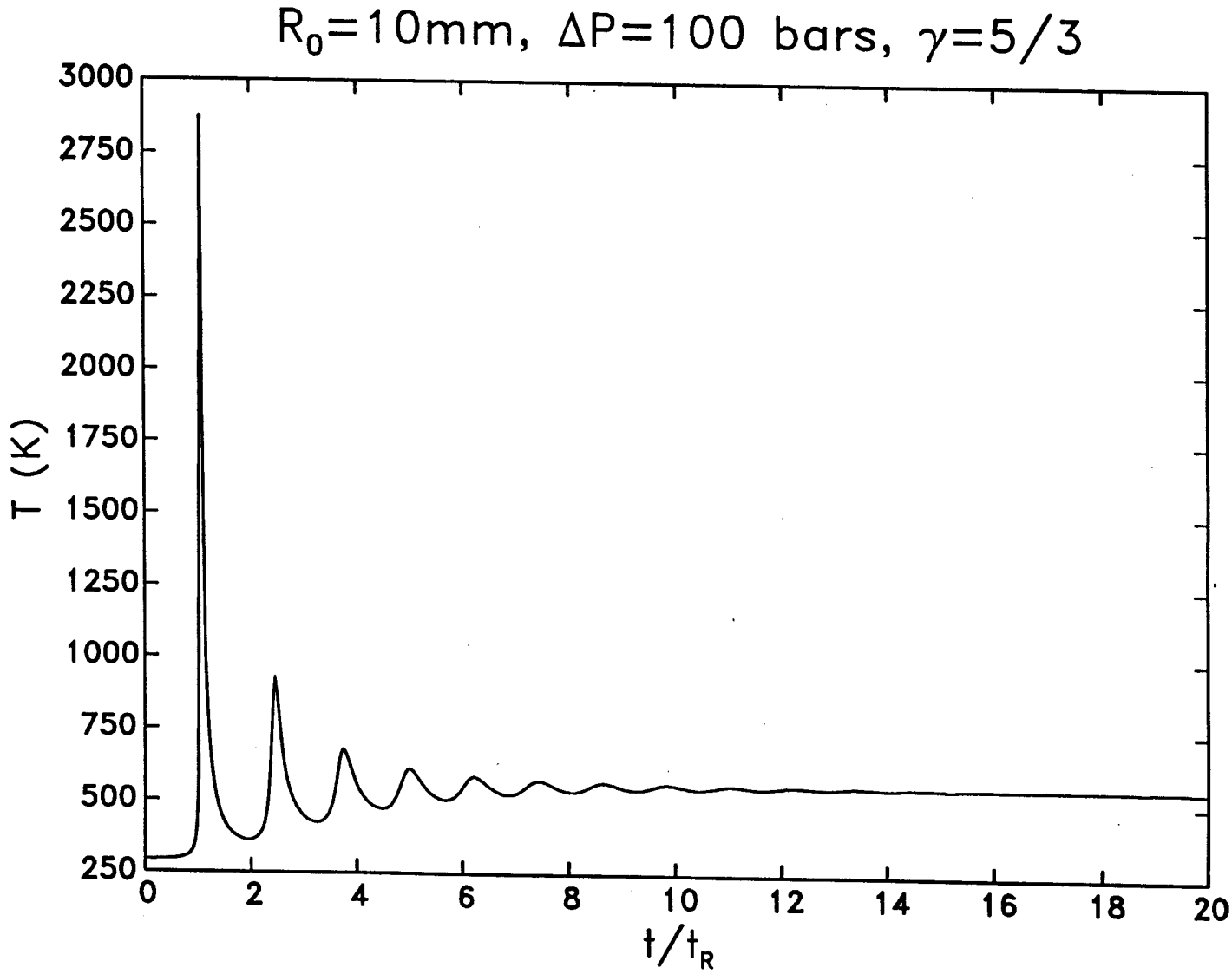

Fig. 20. Bubble surface temperature for a step pressure increase with $\Delta p = 100$ bars and $R_0 = 10$ mm. The Rayleigh time is $t_R = 92$ μs. These results differ from those of Fig. 19 because here the liquid thermal conductivity is 0.075 rather than 0.15 W/mK and the gas adiabatic index is 5/3 rather than 7/5.

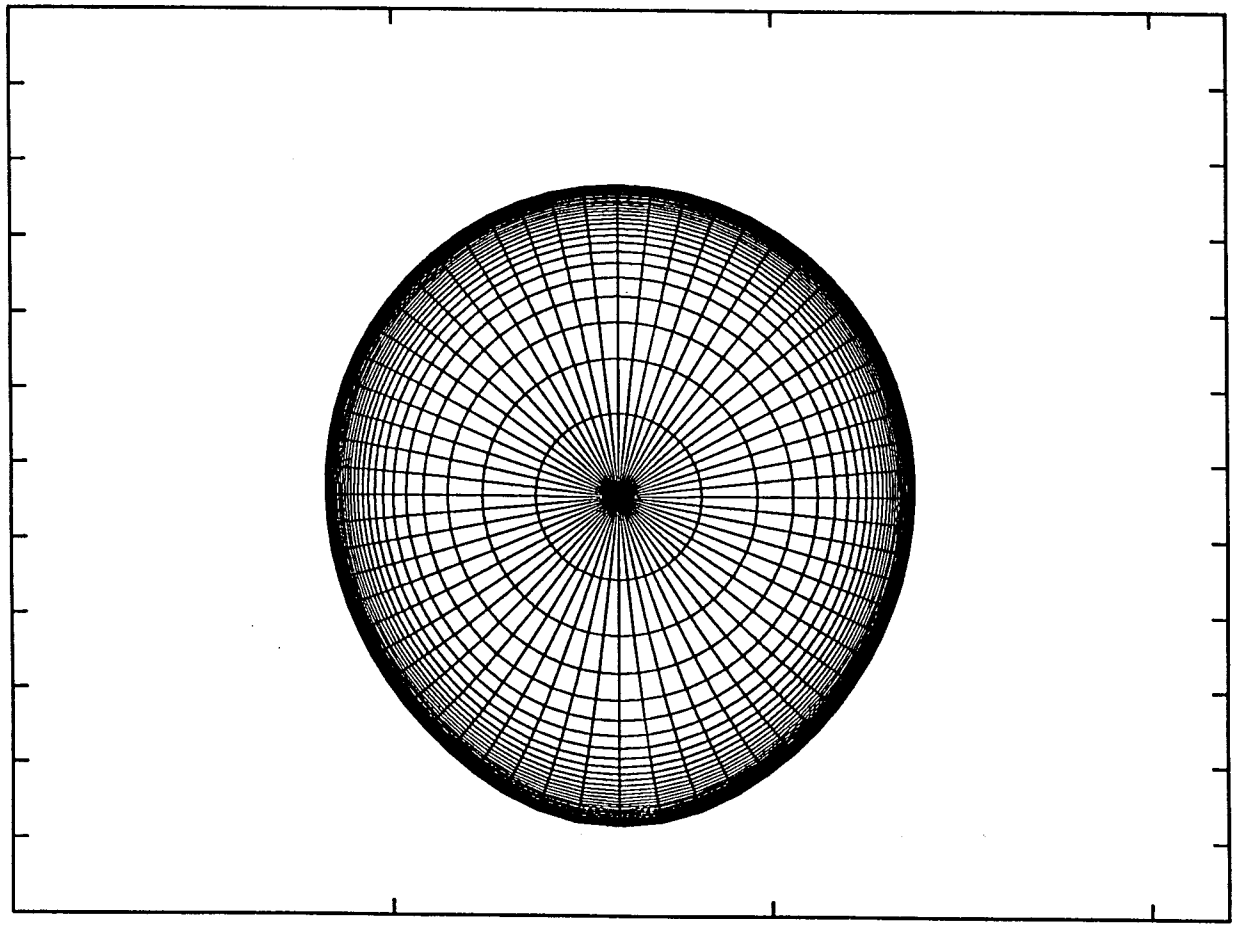

Fig. 21. Example of a numerically generated orthogonal grid for the solution of the Laplace and energy equation in the gas. Here the initial bubble has a radius $R_0 = 1$ mm, with a rigid wall 1.2 mm below the initail bubble center. The collapse is triggered by a pressure step $\Delta p = 10$ bars. The grid is shown at the time $t = 26.64$ μs. The Rayleigh time is $t_R = 29$ μs.

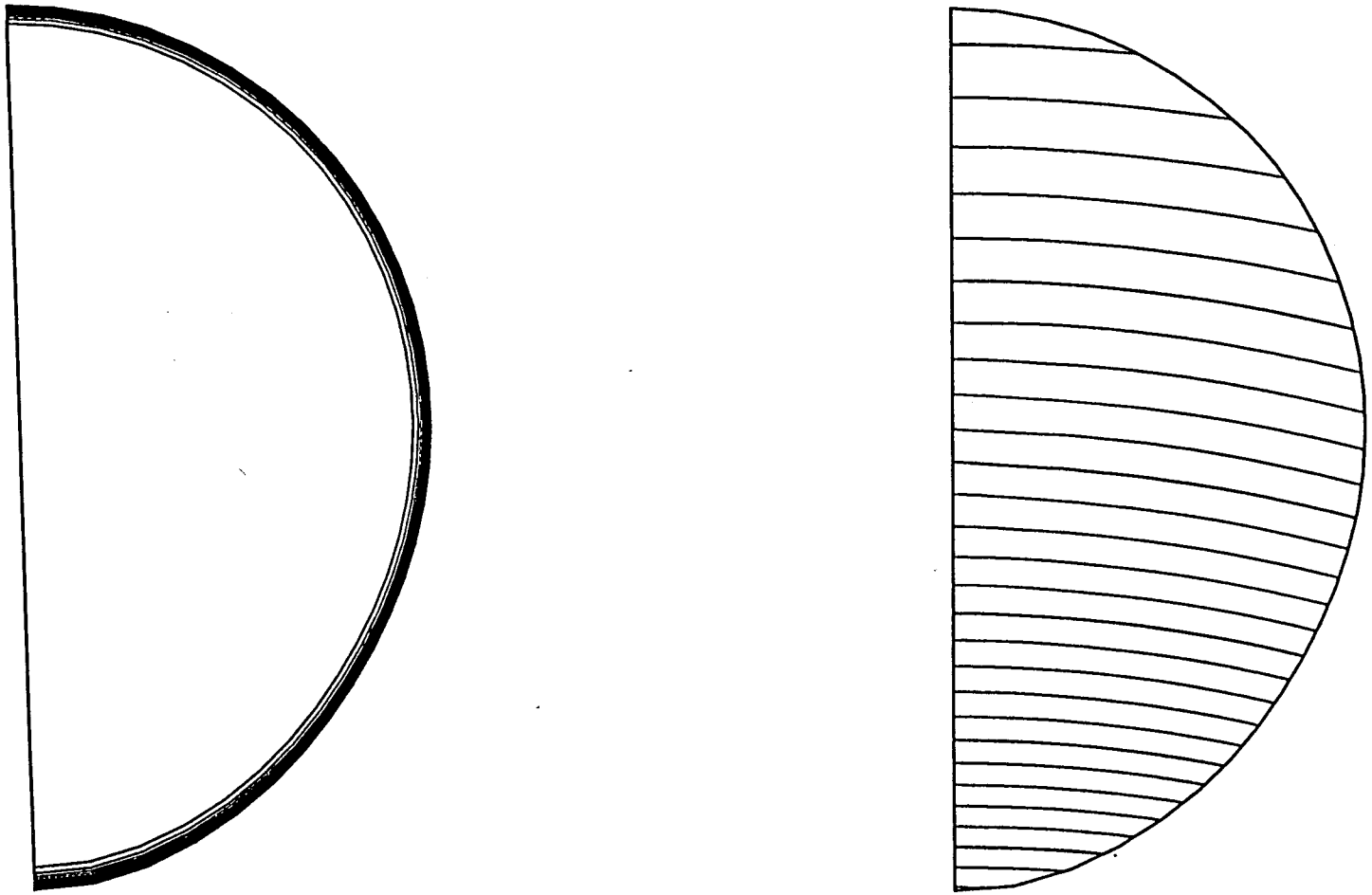

Fig. 22. The left figure shows isotherms calculated with the full model for $R_0 = 1$ mm, with a rigid wall 1.2 mm below the initail bubble center and a pressure step $\Delta p = 10$ bars at $t = 26.64$ μs. The right figure shows the corresponding lines of constant Φ. Here the Rayleigh time is $t_R = 29$ μs.

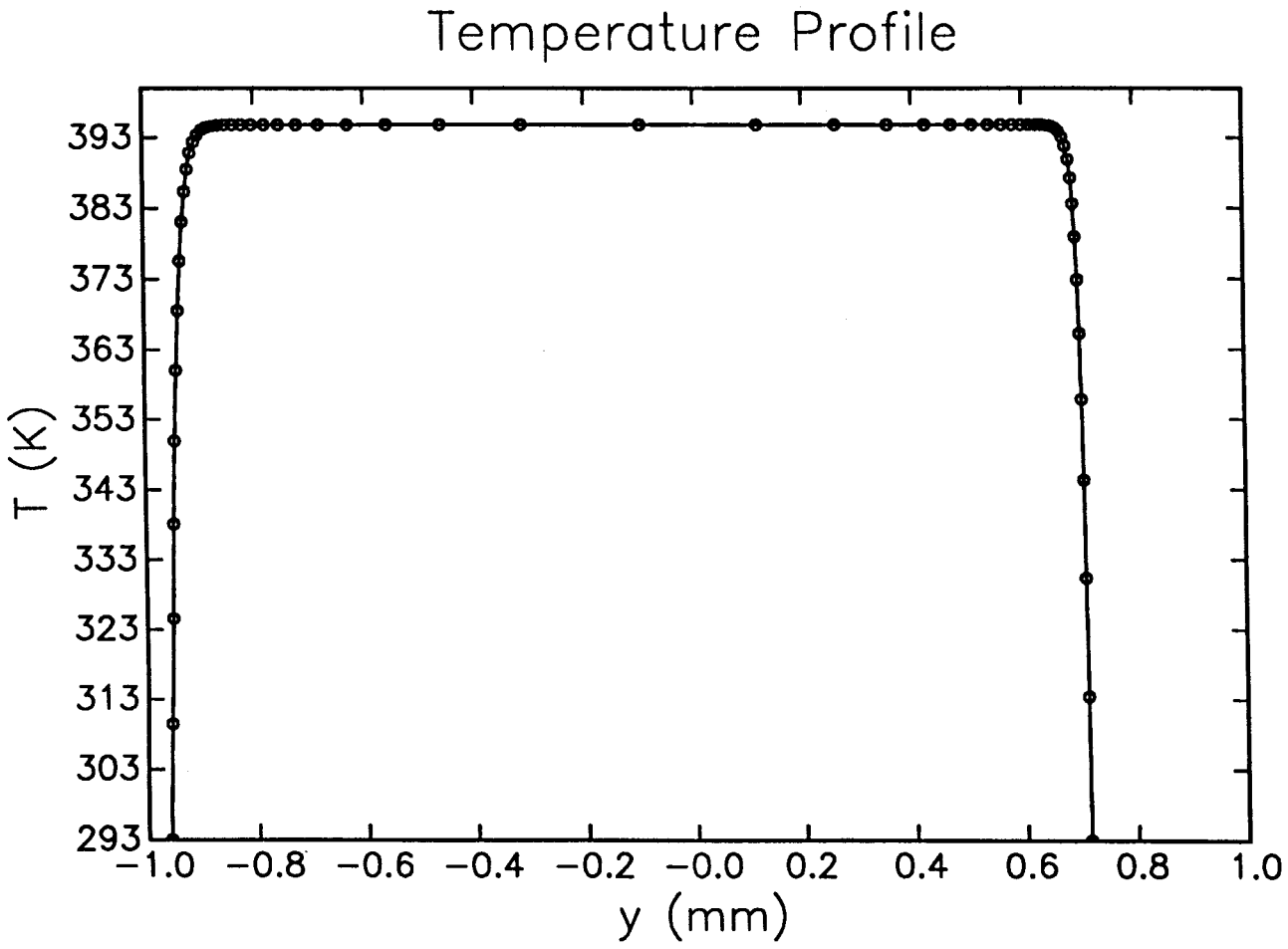

Fig. 23. The gas temperature along the axis of symmetry of the bubble (from the closest to the farthest point from the wall) for the case of the previous figure.

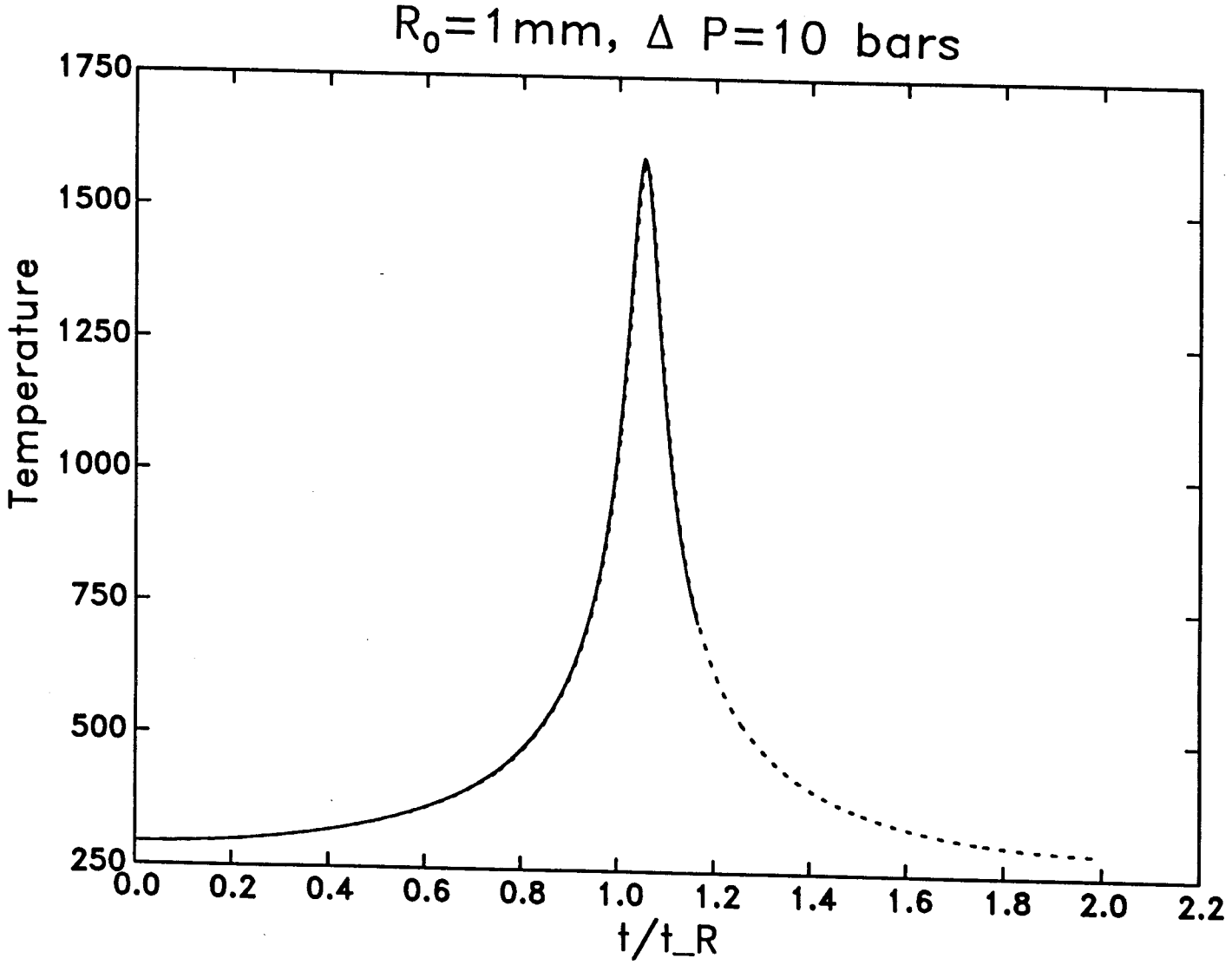

Fig. 24. Comparison between the gas temperatures predicted by the full model (dashed line) and the boundary layer approximation (solid line) for the spherical collapse of an air bubble with $R_0 = 1$ mm and a step pressure increase $\Delta p = 10$ bars.

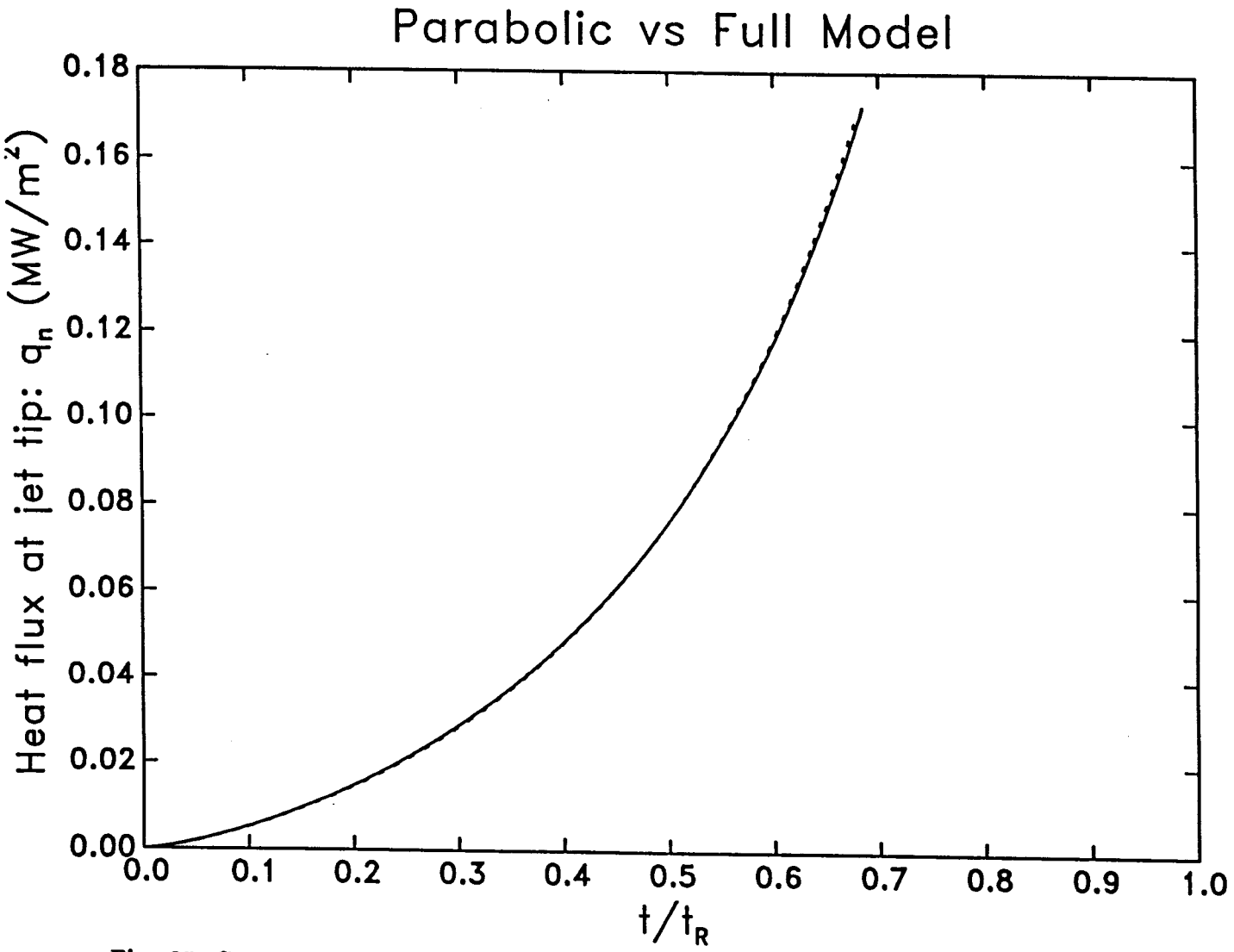

Fig. 25. Comparison between the heat fluxes at the jet tip predicted by the full model (dashed line) and the boundary layer approximation (solid line) for an asymmetric collapse. The case is that of Figs. 21 to 23.

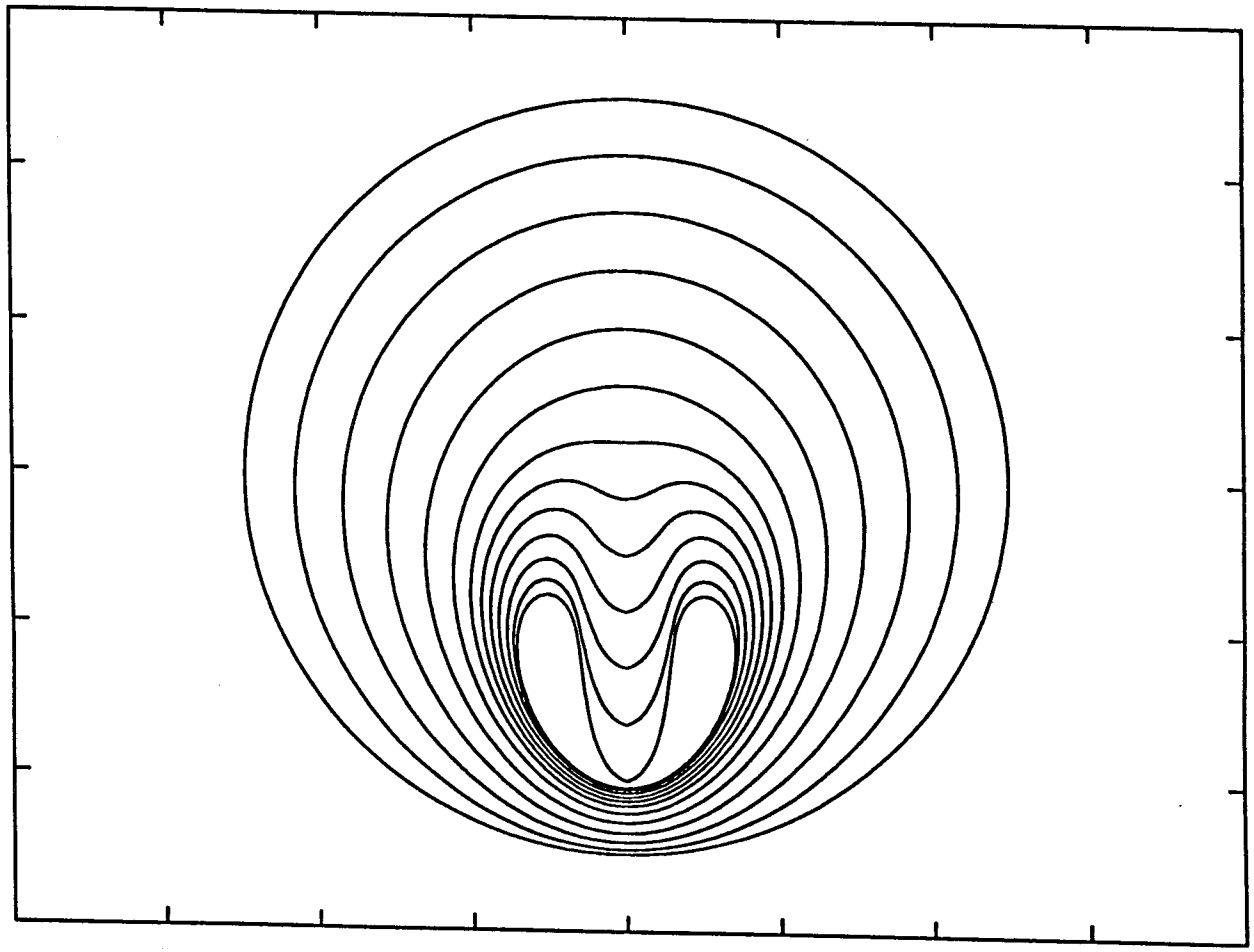

Fig. 26. Successive bubble configurations for a collapse induced by a sudden overpressure with $\Delta p = 10$ bars, $p_0 = 1$ bar. The initial bubble radius is $R_0 = 1$ mm and the rigid wall is initially 1.2 mm below the bubble center.

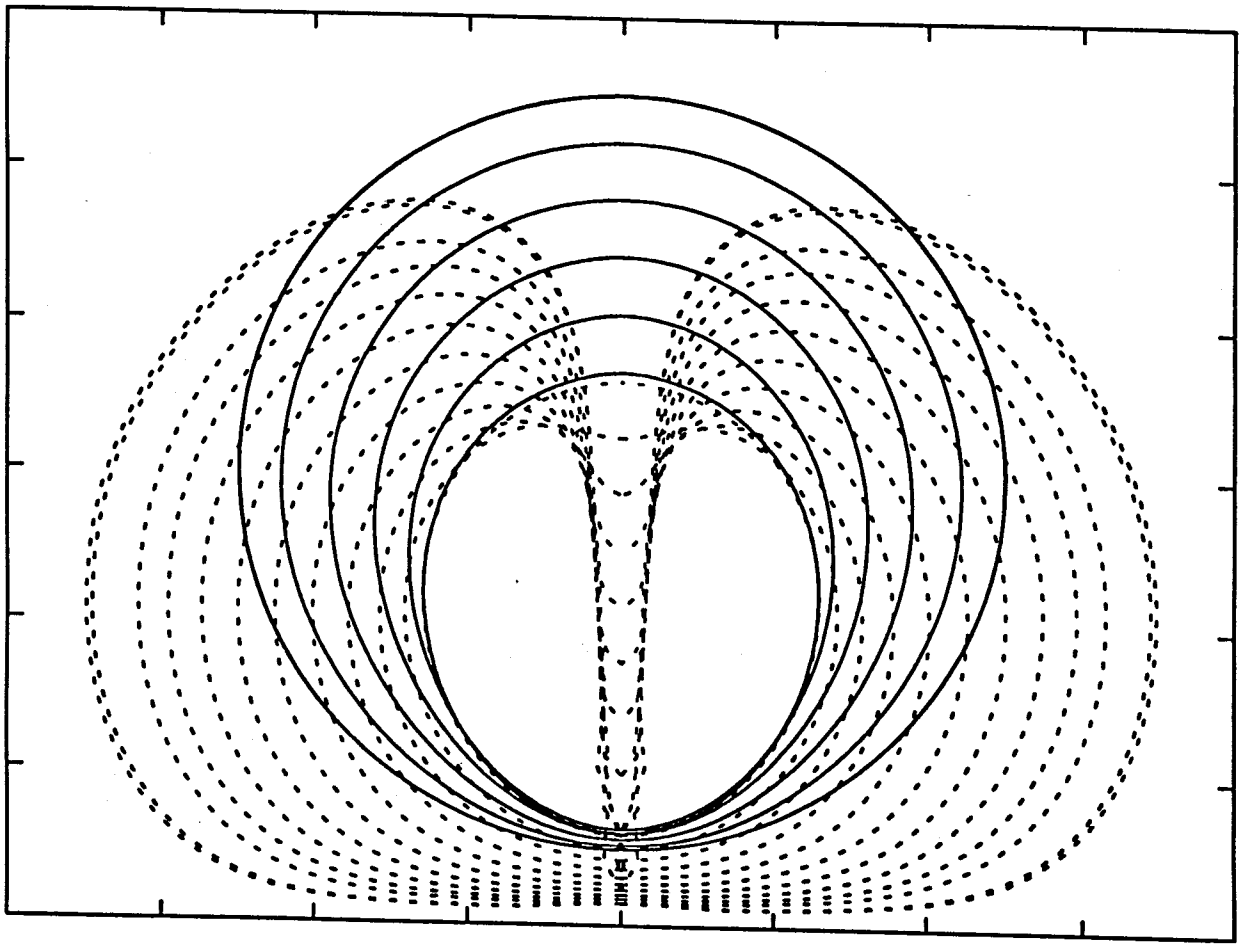

Fig. 27. Successive shapes of a 1 mm-radius air bubble subjected to a Gaussian pressure pulse (2.3.1) with with $t_R/t_p = 4$ and $\Delta p = 10$ bars. Notice that the jet continues to move toward the opposite bubble surface even while the rest of the bubble is rebounding.

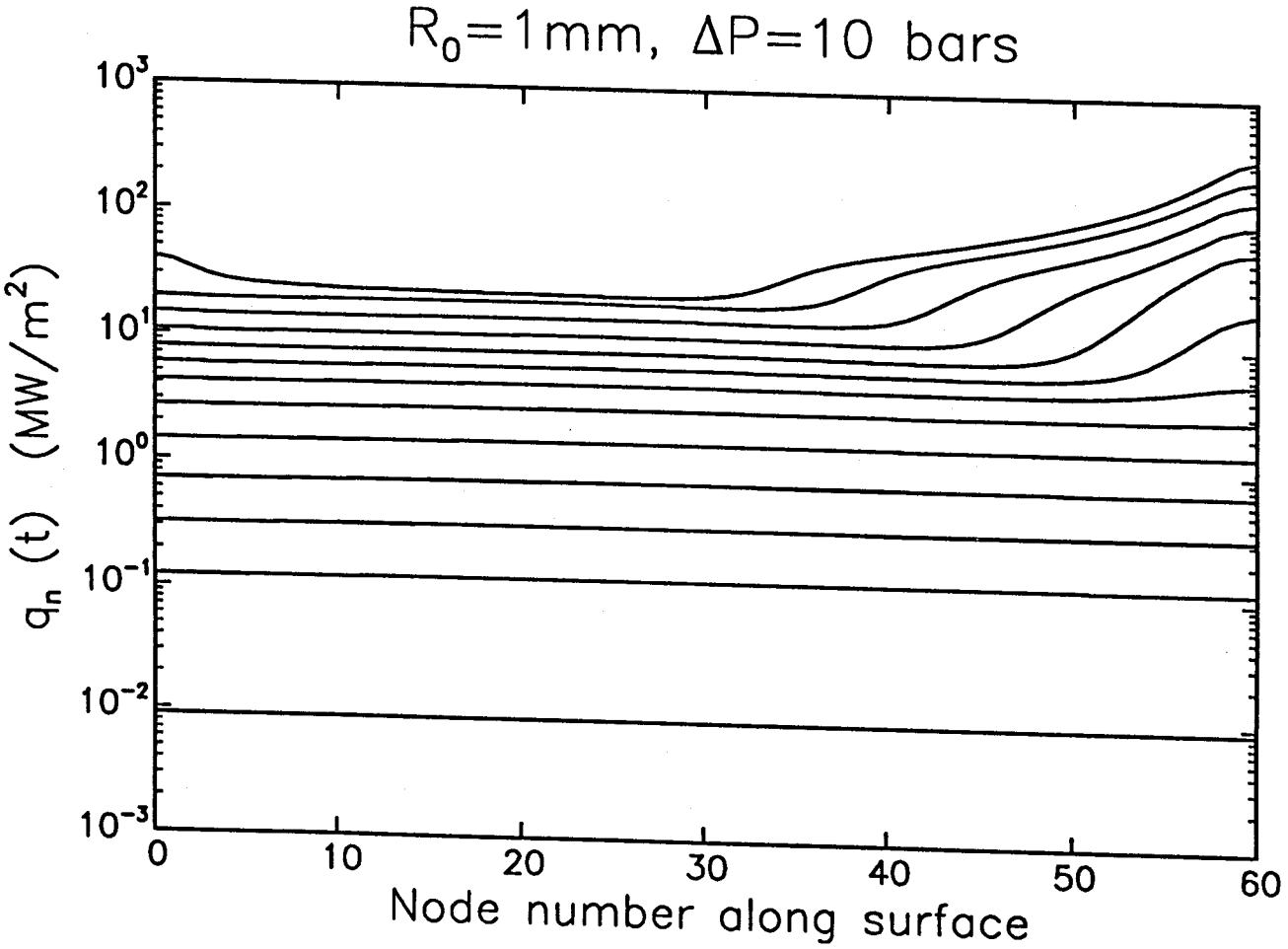

Fig. 28. The local heat flux along the bubble surface for a step pressure increase $\Delta p = 10$ bars as computed from the boundary-layer model at different times for $R_0 = 1$ mm. The abscissa denotes the node number. At each time step sixty equispaced nodes were used.

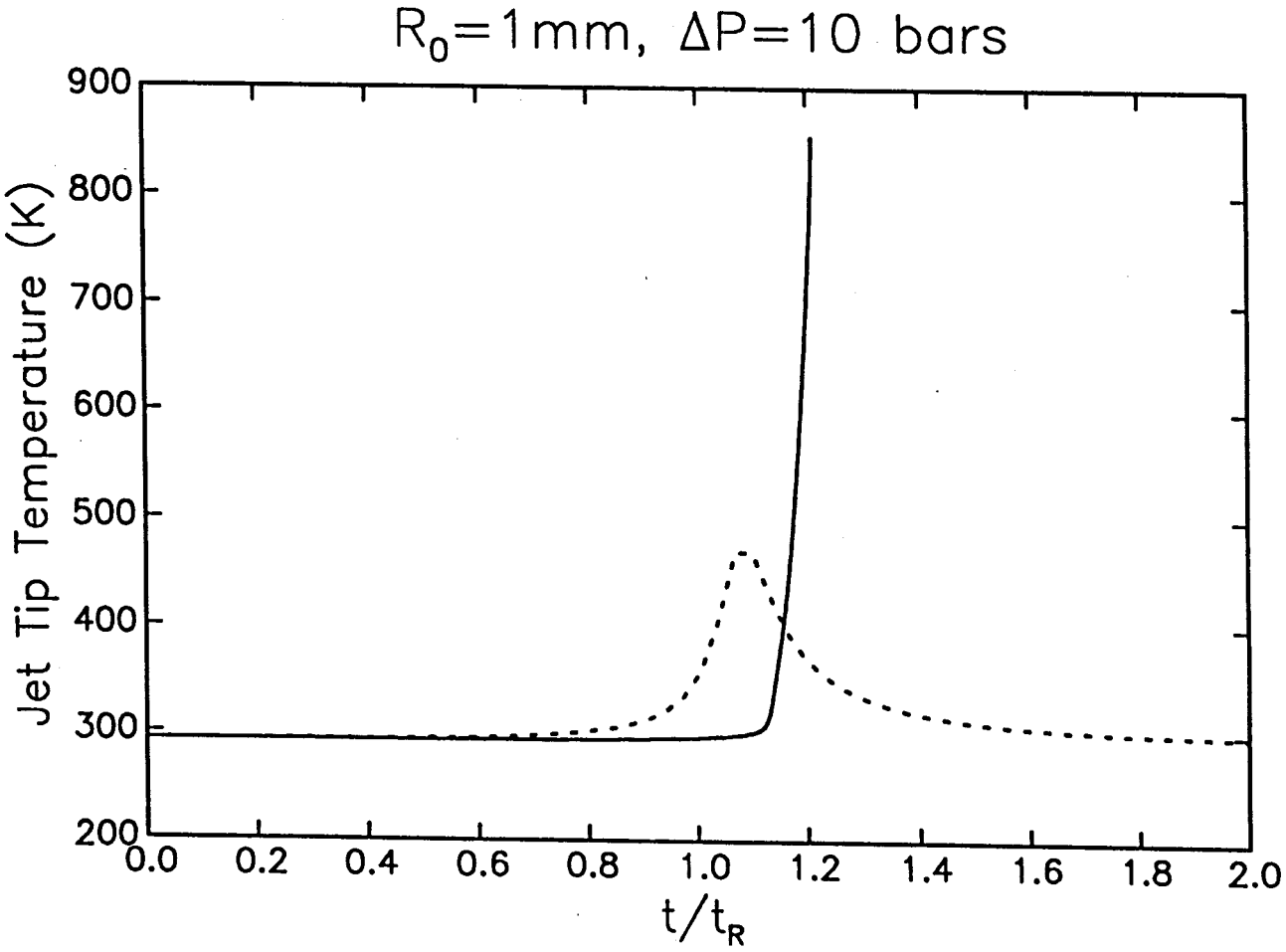

Fig. 29. Estimated jet tip liquid temperature as a function of time for the case of Figs. 21 to 23 (solid line). The dashed line is the liquid temperature for a spherical collapse.

3 Viscous heating of liquid layers under intense shear

The second mechanism that might lead to the appearance of a "hot spot" in the liquid monopropellant that we consider is viscous heating, with particular regard to the flow occurring during the squeezing of a drop of propellant between two colliding parallel plane surfaces. This particular configuration is suggested by the extensive experimental work carried out by Field and co-workers in their falling weight apparatus (Heavens and Field 1974; Swallowe and Field 1982; Krishna Moan and Field 1984; Krishna Moan et al. 1984; Field et al. 1982; Field et al 1992; Bourne and Walley 1993). Although this situation has been studied before (Eirich and Tabor 1947; Field et al. 1982; Bourne and Walley 1993), the effects of the temperature dependence of viscosity have been either disregarded or treated only approximately. Yet, this feature of the problem is exceedingly important as shown by the estimates of maximum temperature rise given by Heavens for nitroglycerine (Field et al. 1982) which drop from about 650 K to 100 K when the temperature dependence of viscosity is approximately allowed for.

In the flow considered, the maximum temperature rise occurs in thin regions parallel to the colliding surfaces. In these regions the viscosity is minimum and the shear is large. There is therefore a resemblance with the occurrence of shear bands in solid materials, which are known to be one of the processes leading to ignition (Winter and Field 1975; Field et al. 1982; Field 1992). This feature of the flow emerges very clearly from our numerical calculations, but is shown to decrease, rather than increase, energy dissipation. A rather non-conventional mechanism leading to another analogue of a shear band that we investigate is the allowance of a small amount of slip at the solid-liquid interface. The process is very sensitive to this effect, which is however limited by the expected smallness of the slip coefficient. This conclusion is however only tentative as little quantitative information is available on this quantity.

3.1 Mathematical Model

In the experimental situation to which reference was made earlier, the portion of the liquid region not bounded by solid surfaces is in contact with air. During the flow, therefore, the liquid-solid-air contact line moves along the solid surfaces. The problems associated with a realistic modeling of this motion are well known (see e.g. Dussan V. 1979). Since, in this study, we wish to focus specifically on viscous heating, we have decided to avoid any contact line problem by supposing that the two colliding plates are immersed in liquid rather than air as shown in Fig. 1. This figure also shows the frame of reference centered on the axis of symmetry at the midpoint of the gap with instantaneous thickness $2h(t)$. The radius of the plates is R.

The flow is assumed to be axi-symmetric and, since the distance between the plates is much smaller than R, we make a boundary layer approximation assuming that derivatives in the radial direction r are small with respect to those in the axial direction normal to the plates z. Neglecting further the compressibility of the liquid, the equations to be solved are the equation of continuity

$$\frac{1}{r}\frac{\partial ru}{\partial r} + \frac{\partial w}{\partial z} = 0\,, \tag{3.2.1}$$

of radial momentum

$$\rho\left(\frac{\partial u}{\partial t} + u\frac{\partial u}{\partial r} + w\frac{\partial u}{\partial z}\right) = -\frac{\partial p}{\partial r} + \frac{\partial}{\partial z}\left(\mu\frac{\partial u}{\partial z}\right)\,, \tag{3.2.2}$$

and of energy

$$\rho C_p\left(\frac{\partial T}{\partial t} + u\frac{\partial T}{\partial r} + w\frac{\partial T}{\partial z}\right) = K\frac{\partial^2 T}{\partial z^2} + \mu\left(\frac{\partial u}{\partial z}\right)^2\,. \tag{3.2.3}$$

Here the symbols have their customary meaning: u and w are the velocity components in the radial and axial direction, p is the pressure, T is the temperature, ρ is the density, C_p is the specific heat, and μ is the viscosity for which we assume a temperature dependence of the form

$$\mu = \mu_\infty \exp\frac{T_a}{T - T_b}\,. \tag{3.2.4}$$

In keeping with the boundary layer approximation the pressure is taken to be uniform in the z direction and to only depend on the distance from the axis of symmetry, $p = p(r,t)$.

The flow region considered is a cylinder of radius R bounded by the plates. The lateral surface of this cylinder is an ideal surface immersed in the fluid on which we prescribe a constant-pressure condition,

$$p = 0 \qquad r = R. \tag{3.2.5}$$

In view of the parabolic nature of the equations, no further conditions on velocity or pressure are necessary at $r = R$.

The normal velocity relative to the plates must vanish,

$$w(r, z = \pm h, t) = \mp V(t) \qquad \text{on} \quad z = \pm h(t), \tag{3.2.6}$$

where $V(t) > 0$ is the upward velocity of the lower plate or, equivalently, the downward velocity of the upper plate. For the tangential velocity, we write

$$u = \mp\lambda \frac{\partial u}{\partial z} \qquad \text{on} \quad z = \pm h(t), \tag{3.2.7}$$

where λ is a constant with dimensions of a length. Upon taking $\lambda = 0$, we recover the standard no-slip boundary condition.

In the course of the experiment that we model, the plates are driven together by the impact of a weight. When the mass M of this weight is very large, one may assume that the velocity V is a constant. However, for smaller masses, $V(t)$ must be determined accounting for the normal force exerted on the plates by the squeezing of the liquid. Thus, in this case, we write

$$2M\frac{dV}{dt} = \int p ds. \tag{3.2.8}$$

where the integration is over the surface of the plate from 0 to R. The contribution from the normal viscous stress is identically zero in the no-slip case as a consequence of (3.2.1) and very small in the case with slip and has been neglected. The factor of 2 in the left-hand side accounts for the fact that the plate velocity in the laboratory frame where the lower plate is at rest is twice the plate velocity in the present frame.

For the temperature field we consider two conditions on the solid surfaces:

i *Isothermal wall*

$$T = T_0. \tag{3.2.9}$$

ii *Adiabatic wall*

$$K\frac{\partial T}{\partial z} = \lambda\mu\left(\frac{\partial u}{\partial z}\right)^2. \tag{3.2.10}$$

We now introduce dimensionless variables, denoted by an asterisk, as follows:

$$r = Rr_* \qquad t = \frac{h_0}{V_0}t_*, \qquad z = h(t)z_* \qquad h(t) = h_0 h^*(t), \tag{3.2.11}$$

$$u = V_0 u_* \qquad w = \frac{h_0}{R}V_0 w_*, \tag{3.2.12}$$

$$p = \rho V_0^2 p_*, \qquad T = T_0 T_*, \qquad \mu = \mu_0 \mu_*. \tag{3.2.13}$$

Here $h_0 = h(0)$ is one half of the initial plate separation and μ_0 is the liquid viscosity at the initial ambient temperature. The definition of z_* in (3.2.11) has the advantage of mapping the time dependent domain $-h(t) \le z \le h(t)$ onto the fixed domain $-1 \le z_* \le 1$. V_0 is a characteristic value of the velocity V with which the plates approach each other and the scaling (3.2.12) for w reflects the boundary-layer like nature

of the flow. In terms of these new variables, and dropping the asterisks for simplicity, Eqs. (3.2.1) to (3.2.3) become

$$\frac{1}{r}\frac{\partial ru}{\partial r}+\frac{1}{h(t)}\frac{\partial w}{\partial z}=0\,, \tag{3.2.14}$$

$$\frac{\partial u}{\partial t}+Au\frac{\partial u}{\partial r}+\frac{1}{h(t)}(Aw-zh')\frac{\partial u}{\partial z}=-A\frac{\partial p}{\partial r}+\frac{1}{Re}\frac{1}{h(t)^2}\frac{\partial}{\partial z}\left(\mu\frac{\partial u}{\partial z}\right), \tag{3.2.15}$$

$$\frac{\partial T}{\partial t}+Au\frac{\partial T}{\partial r}+\frac{1}{h(t)}(Aw-zh')\frac{\partial T}{\partial z}=\frac{1}{Re\,Pr}\frac{1}{h(t)^2}\frac{\partial^2 T}{\partial z^2}+\frac{\mu}{h(t)^2}\frac{Ec}{Re}\left(\frac{\partial u}{\partial z}\right)^2. \tag{3.2.16}$$

Here $h'=dh/dt$,

$$\mu=\exp\frac{T_a^*(1-T)}{(T-T_b^*)(1-T_b^*)}\,, \tag{3.2.17}$$

and the aspect ratio A, Reynolds number Re, Prandtl number Pr, and Eckert number Ec are defined by

$$A=\frac{h_0}{R}\,,\qquad Re=\frac{\rho V_0 h_0}{\mu_0}\,,\qquad Pr=\frac{C_p\mu_0}{K}\,,\qquad Ec=\frac{V_0^2}{C_pT_0}\,. \tag{3.2.18}$$

An expression for the pressure gradient can be found by integrating Eq. (3.2.15) across the half-width of the gap $0\le z\le 1$:

$$A\frac{\partial p}{\partial r}=\frac{1}{Re}\frac{\mu}{h(t)^2}\frac{\partial u}{\partial z}\bigg|_1-\frac{\partial}{\partial t}\int_0^1 u\,dz+\frac{A}{2}\left(\frac{h'}{h}\right)^2 r-\frac{A}{r}\int_0^1\frac{\partial ru^2}{\partial r}dz\,. \tag{3.2.19}$$

Because of the symmetry of the flow about the midplane of the gap, it is sufficient to solve Eqs. (3.2.14) to (3.2.16) in the range $0\le z\le 1$. Appropriate symmetry conditions are imposed on $z=0$. At $z=1$ the velocity condition (3.2.7) becomes

$$u=\lambda_*\frac{\partial u}{\partial z}\qquad\text{with}\quad\lambda_*=\frac{\lambda}{h_0}\,. \tag{3.2.20}$$

and the dimensionless thermal boundary conditions are

i *Isothermal wall*

$$T=1\,. \tag{3.2.21}$$

ii *Adiabatic wall*

$$\frac{\partial T}{\partial z}=Ec\,Pr\frac{\lambda\mu}{h}\left(\frac{\partial u}{\partial z}\right)^2. \tag{3.2.22}$$

Since $2V=-dh/dt$, from Eq. (3.2.8) we have

$$\frac{d^2h}{dt^2}=\frac{m}{2M}\int_0^1(1-r^2)\frac{\partial p}{\partial r}dr. \tag{3.2.23}$$

where $m=\rho\pi R^2h_0$, is the initial mass of the liquid in the volume of interest. In deriving this equation we have expressed p in (3.2.8) as the integral of its derivative and interchanged the order of integration.

3.2 Numerical Method

The system of equations posed in the previous section is solved by finite differences in the region $0 \leq r, z \leq 1$. In order to cluster the grid points near the solid surface where gradients are large, we use a uniform grid in the auxiliary variable $\xi = \tan\left(\frac{\pi}{2}\epsilon z\right) / \tan\left(\frac{\pi}{2}\epsilon\right)$, that also ranges between 0 and 1.

We discretize the momentum and energy equations (3.2.15) and (3.2.16) fully implicitly using upwinding for the convective terms. Upwinding is also used in the last term of the pressure equation (3.2.19). The resulting nonlinear system is solved iteratively in the following fashion. First, with the most recently updated value of the temperature the viscosity is calculated and the velocity field u updated from (3.2.15). The pressure term in the equation is expressed by means of (3.2.19) with the integrals effected by the trapezoidal rule. Next w is calculated from the continuity equation (3.2.14) and the temperature field updated. The process is arrested when the maximum relative correction to the temperature field is less than 10^{-8}.

When Eq. (3.2.23) for V is used, it is integrated explicitly by the Euler one-step method.

To simulate the impulsive nature of the flow, initially we assume that the radial velocity field u is uniform and the vertical velocity w is linear in the vertical coordinate. These fields are such that the continuity equation and the normal velocity condition (3.2.6) are satisfied for a plate velocity $V(0)$. This state of motion violates of course the no-slip condition but is an accepted procedure for impulsively started flows (see e.g. Gresho 1991).

The time step is set proportional to the gap width to resolve the extremely large velocity and temperature rates of change in the final stages of the process.

3.3 Results

The numerical results that follow have been obtained for the case of LGP 1845 for which $\rho = 1.452$ g/cm^3, $K = 0.15$ W/mK, $C_p = 2{,}300$ J/kgK, $Pr = 175$, $T_a = 524$ K, $T_b = 167$ K, $\mu_\infty = 0.169$ cP. We also take the plate radius $R = 10$ mm, half the initial plate separation $h_0 = 1$ mm, and the initial temperature $T_0 = 20$ °C, with a corresponding viscosity $\mu_0 = 10$ cP. With an initial velocity $V(0) = 1$ m/s, we thus have

$$A = 0.1\,, \qquad Re = 134.1\,, \qquad Ec = 1.4 \times 10^{-6}\,. \tag{3.4.1}$$

We first study the case in which the velocity of the plates is prescribed and their surface is adiabatic.

In view of the cylindrical geometry, radial velocities get larger with increasing distance from the axis and we therefore focus on the velocity and temperature distributions at $r = R$. In Fig. 2 we show the distribution of u across the gap $0 \leq z/h(t) \leq 1$ at different times for $V(0) = 1$ m/s. The calculation is stopped when the gap thickness reaches 10 μm, i.e. 0.5% of the initial value. Although not very clear from the figure, initially the velocity distribution is very nearly uniform except for a thin boundary layer near the plates. With time, viscous diffusion promotes the appearance of a profile with a vague similarity to the parabolic distribution that would be given by a lubrication approximation. Since here the Reynolds number for the radial flow is of the order of 10^4 and the flow highly unsteady, the physics underlying this distribution is of course quite different from that applicable in the lubrication case. Still later, due to the increasing energy dissipation near the wall, viscosity decreases and the velocity becomes nearly uniform in the central region. As a consequence, the shear becomes localized near the wall, where the temperature grows at a faster rate. Viscosity decreases further, and a non-monotonic velocity profile develops exhibiting features analogous to those of shear band in a solid. In the example studied here, this feature arises only very late in the process when the plate spacing is of the order of 0.5% of its initial value.

A corresponding sequence of temperature distributions across the gap at $r = R$ is shown in Fig. 3. In view of the large value of the Prandtl number the temperature rise occurs in a region that remains relatively thin compared with the gap width. The temperature increase becomes substantial only in the very last stages of the process. This point is clearer from Fig. 4 which shows the maximum temperature in the system (that occurs in this case on the plates at $r = R$) as a function of the dimensionless gap width $h(t)/h(0)$. The corresponding history for the radial velocity at $r = R$, $z = 0$ is shown in Fig. 5. In these two figures the solid lines are obtained allowing for the temperature dependence of viscosity and the dashed lines with a constant

viscosity, $\mu = \mu_0$. Clearly there is a very large difference between the two cases that indicates the total unreliability of the constant-viscosity model in the later stages of the process. Constant viscosity results will not be considered further. Figure 6 shows the radial velocity in the plane of symmetry (solid lines) and the maximum temperature (occurring at the wall for $r = R$, dashed lines) as functions of $h(t)/h(0)$. The upper pair of lines is for $V_0 = 1$ m/s, and the lower one for $V_0 = 0.5$ m/s. The solid curves for the velocity exhibit a small local maximum in the later stages of the process. This is due to the formation of the shear-band-like structure near the wall that has the effect of causing a temporary slowing down of the liquid at the midplane.

Figures 7 to 9 refer to the isothermal wall case. Figure 7 shows the radial velocity profiles at $r = R$ at different times for $V_0 = 1$ m/s. Qualitatively the trend is quite similar to that shown in Fig. 2 for the adiabatic wall case. However, the shear-band-like structure forms somewhat later, as could be anticipated. The corresponding temperature distributions, to be compared with those of Fig. 3, are shown in Fig. 8. Because of the relatively small thermal conductivity of the fluid, there is a substantial temperature increase in this case as well, although the magnitude is about one half of that found in the adiabatic-wall case. The velocity (solid lines) and temperature histories comparable to those of Fig. 6 are shown in Fig. 9. Upon comparison of the two, it is is seen that the maximum velocities are not very strongly affected by the wall boundary condition, while the temperature increases are reduced by about 50%.

We now turn to the more realistic situation in which the motion of the plates is opposed by the pressure field developing in the liquid. We use the same parameter values as before, but now V_0 is the initial condition for the velocity $V(t)$ that is calculated as explained before. The major difference with the previous case is that now the velocity of the plates starts decreasing appreciably as the pressure builds up. Of course, this effect sets in later and later as the inertia M of the plates is increased, but nevertheless it is a major effect for any M. Velocity and temperature distributions are similar to those shown in the previous figures, except for the fact that it is difficult to generate shear-band structures. To appreciate the differences with the previous cases it will be sufficient to consider the time histories of the radial velocity at $z = 0$ (solid lines) and maximum temperature shown in Figs. 10 and 11 for the adiabatic and isothermal cases respectively. For all cases $V_0 = 1$ m/s and the lines are, in descending order, for $M = 2$, 1 and 0.2 kg. A very striking difference with the previous situation is the drastic velocity reduction. Naturally, this is accompanied by a strong reduction in the maximum temperature increase. The 50% difference between the adiabatic and isothermal wall cases found before is also encountered here.

It is interesting to note that the acceleration becomes strongly negative in the later stages of the flow. In a situation in which a single drop of liquid is squeezed between the plates, the free surface along the rim of the drop would thus be subject to an acceleration directed from the surrounding air into the liquid, which is a Rayleigh-Taylor unstable situation. Thus one would expect a roughening of the drop periphery as is indeed observed experimentally (see e.g. Field et al. 1982). As a matter of fact, the ignition events reported by Field and co-workers all seem to originate in this peripheral region, possibly due to air entrapped by the surface deformation of the drop.

The final aspect that we consider is that of wall slip. Our justification is twofold. In the first place, the usual no-slip condition is an empirical fact that has never been tested at the extremely high velocities encountered in some of the cases that we have simulated. Secondly, it is known (see e.g. Richardson 1973; Davis and Miksis 1994) that the no-slip condition on a rough wall may be approximately replaced by a partial slip condition of the form (3.2.7) over a plane surface. In the first case, the parameter λ may be expected to be of the order of molecular (or molecular clusters) dimensions, so that $\lambda \sim$ 1-10 nm. In the second one, λ is of the order of the total volume of the roughnesses per unit area of the surface. For a polished metal surface typical values are in the range of 0.1 to 1 μm.

With slip, there is intense energy dissipation at the wall and it would be meaningless to consider the case of an isothermal wall. Hence we show in Fig. 12 the wall temperature at $r = R$, $z = h(t)$ as a function of $h(t)/h_0$ for $\lambda = 100$ nm, 10 nm, and 0. The 10 nm case exhibits only a negligible difference with the previous no-slip results. For $\lambda = 100$ nm, on the other hand, the temperature rise is approximately double that found in the no-slip case.

3.4 Conclusions on Viscous Heating

In this section we have studied the viscous heating of a thin ($\sim$ 2 mm) liquid layer squeezed between two rapidly approaching parallel rigid plates. The main conclusions are as follows:

1. Accounting for the temperature dependence of viscosity is essential. Constant-viscosity simulations give maximum temperature rises that can be an order of magnitude larger than those found allowing viscosity to decrease with increasing temperature.

2. If the velocity of the approaching plates is held constant, large temperature rises can be found by the time the plate spacing is of the order of 10 μm. This happens with both adiabatic and isothermal wall boundary conditions, although maximum temperature rises are about 50% smaller in the latter case. In addition, high-velocity "jets" resembling shear bands in solids form near the boundary due to the strong viscosity reduction in this region of high shear.

3. If the reaction of the liquid on the plates through the developing pressure field is accounted for, the violence of the phenomenon is greatly reduced and typical maximum temperature rises are of the order of 300 ° for an adiabatic wall and half as much for an isothermal wall.

4. The wall temperature is found to be very strongly sensitive to wall slip above a certain level. This aspect of the problem could be significant, but it has not been possible to pursue it to any great depth in view of the fact that very little seems to be known about the magnitude of the wall slip coefficient. In this connection, we might refer again to the ignition of propellants near the rim of the expanding drop observed in experiments. Indeed, it seems to be fairly well established that the motion of an air-liquid-solid contact line is accompanied by local slip (see e.g. Huh and Scriven 1971; Richardson 1973; Dussan V. 1979).

These results indicate that the process under consideration is strongly influenced by subtle aspects that cannot be ignored even as a first approximation. In particular, the effect of the large pressures developed in the liquid has been found to be important. In the model that we have studied, the solid surfaces were assumed to be rigid and the only effect of these pressures was to slow down the approach of the plates at a rate dependent on their inertia. More generally, when the inertia is very large, the high local pressures will lead to a deformation of the approaching surfaces which will also tend to strongly limit the heating of the liquid.

In all the cases we have studied, substantial liquid heating only occurs when the film has thinned to about 10 μm or less. At speeds of 1 to 0.1 m/s, the gap would close completely in 0.01 to 0.1 ms. According to the estimates of Field (1992; Field et al. 1992), over time and spatial scales of this magnitudes, temperatures of the order of 700 K are needed for ignition. Our results imply that such conditions are very hard to realize by relying solely on viscous heating.

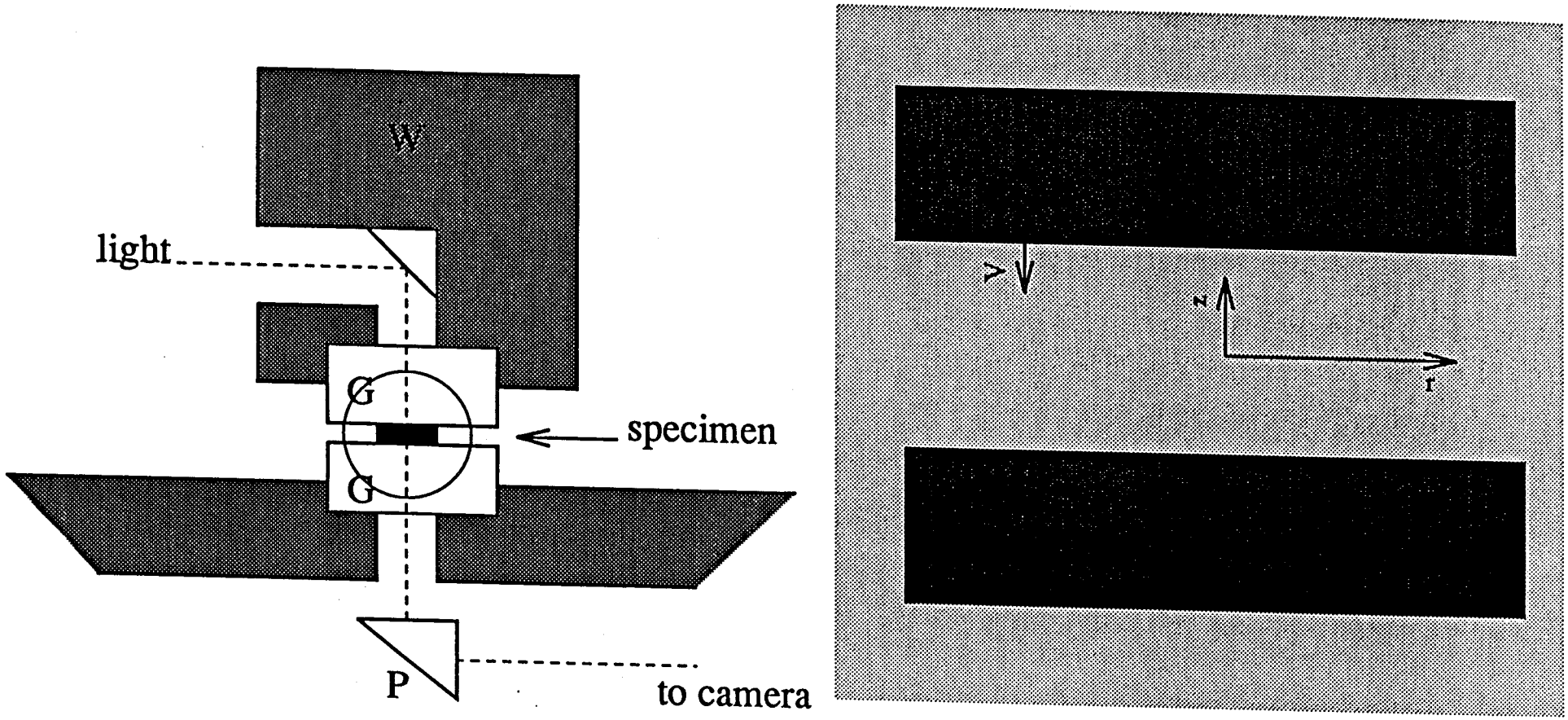

Fig. 1 The left part of the figure is a sketch of the experiment that motivates this study. The right part shows the process simulated in the present computations with the frame reference centered on the plane of symmetry.

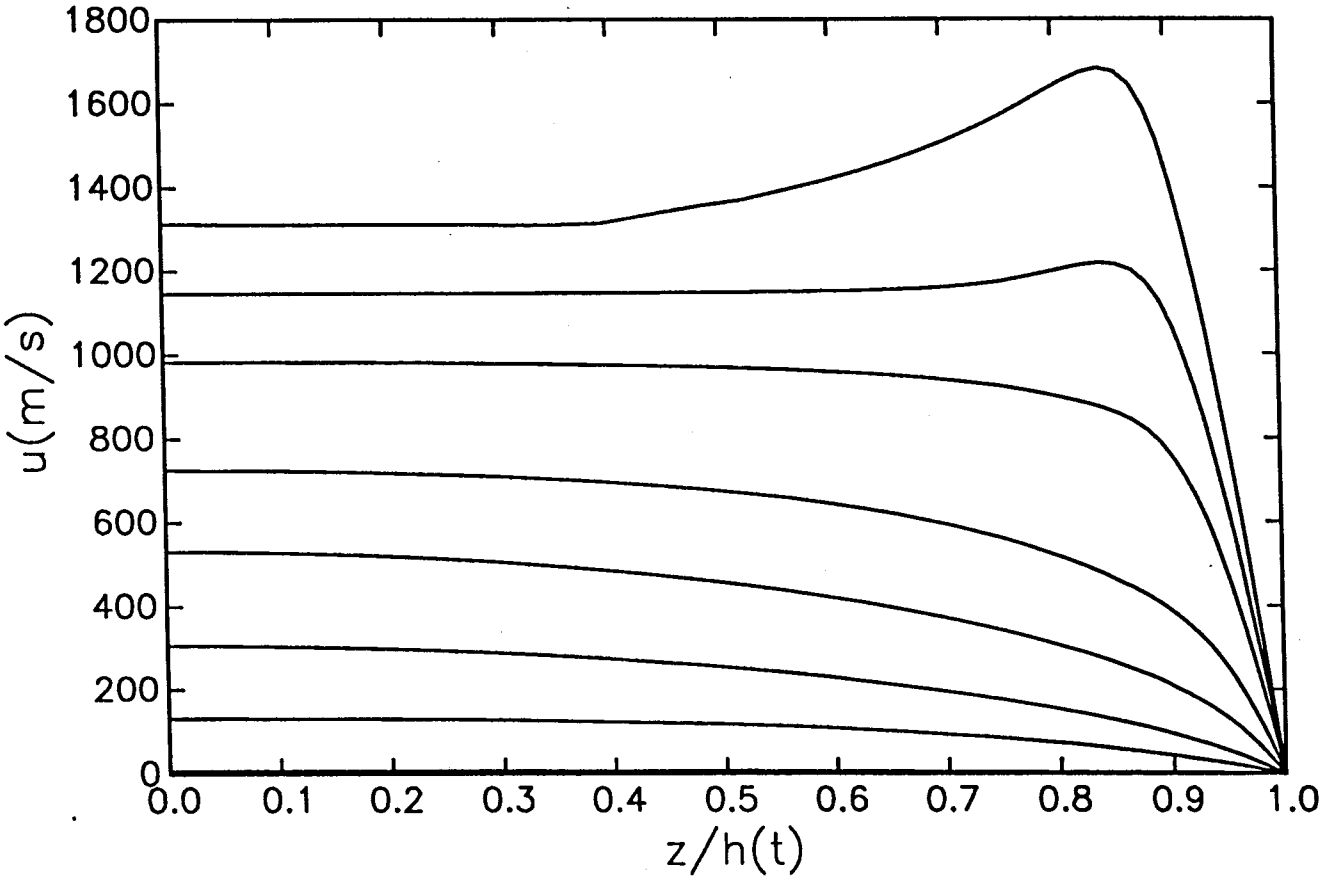

Fig. 2 Distribution of the radial velocity u across the gap at the edge of the plates for a constant velocity of approach $V_0 = 1$ m/s and adiabatic walls. The lines are, in descending order, for $h/h_0 = 0.00369, 0.00451, 0.00551, 0.00822, 0.0123, 0.0223, 0.0497, 0.819$.

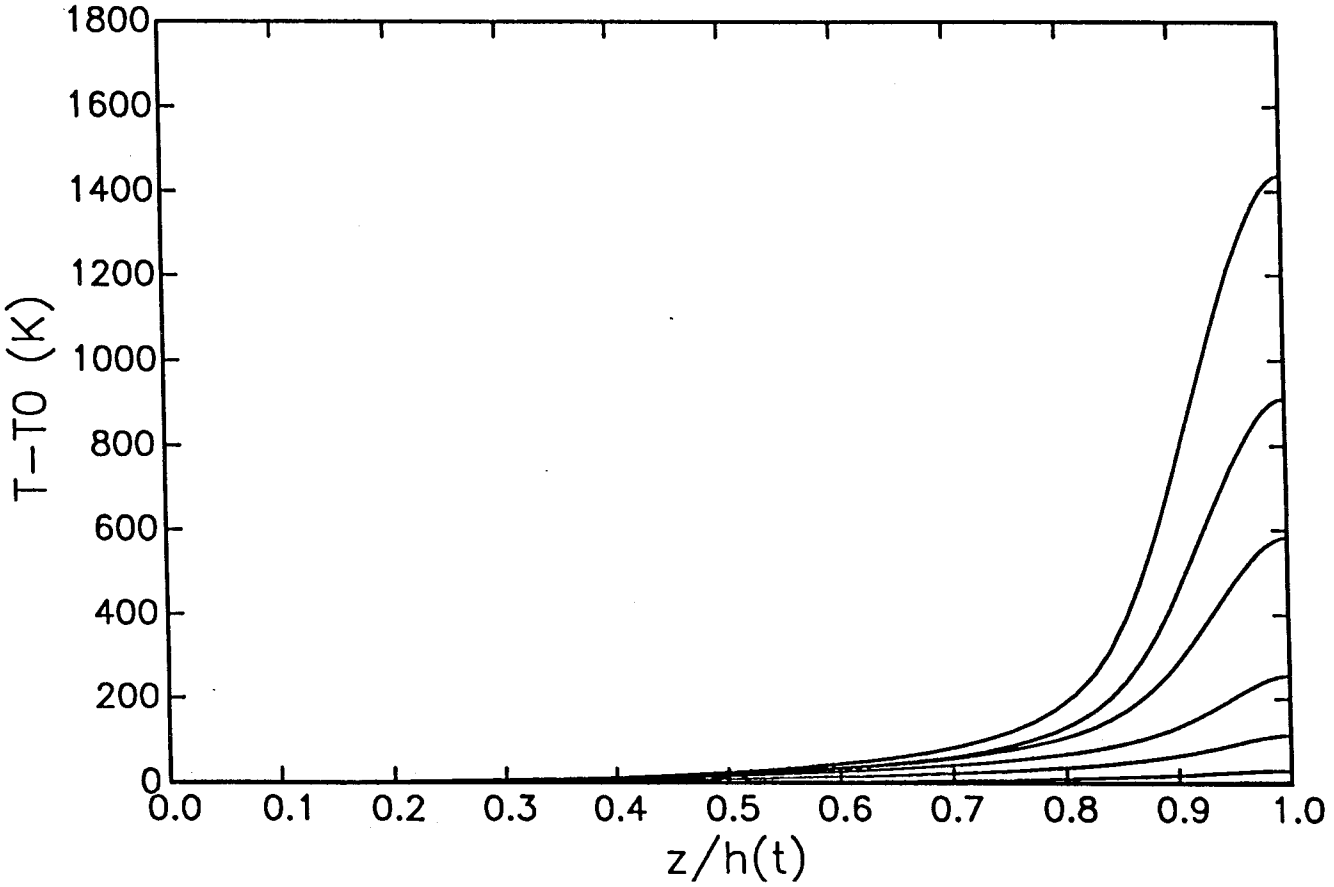

Fig. 3 Temperature distribution across the gap at the edge of the plates for a constant velocity of approach $V_0 = 1$ m/s and an adiabatic wall. The lines are, in descending order, for $h/h_0 = 0.00369, 0.00451, 0.00551, 0.00822, 0.0123, 0.0223, 0.0497, 0.819$.

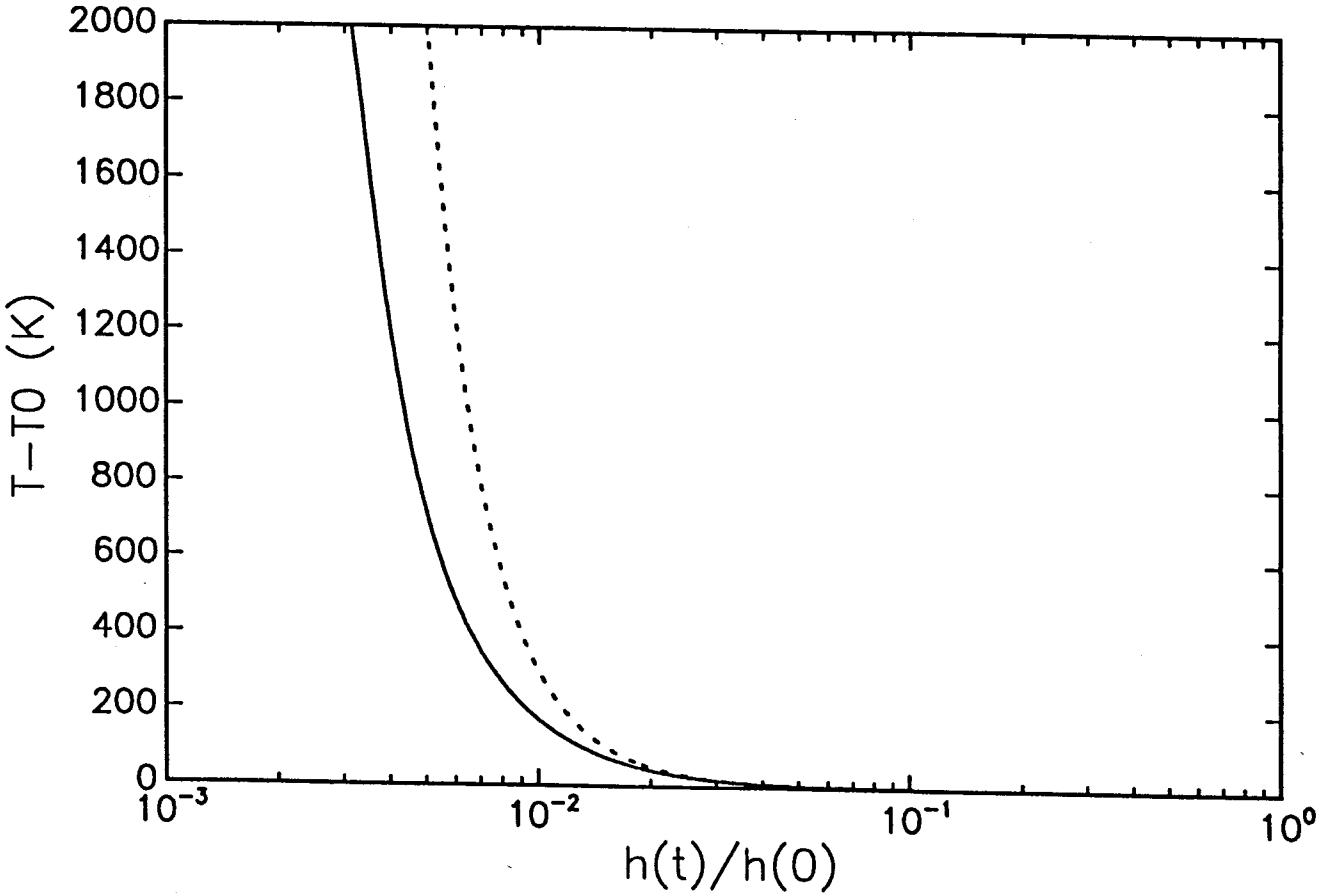

Fig. 4 Maximum liquid temperature (occurring on the plates at $r = R$) as a function of the dimensionless gap width $h/h(0)$ for the adiabatic-wall case and a fixed velocity of approach $V_0 = 1$ m/s. The solid line is for a temperature-dependent viscosity, the dashed line for a constant viscosity.

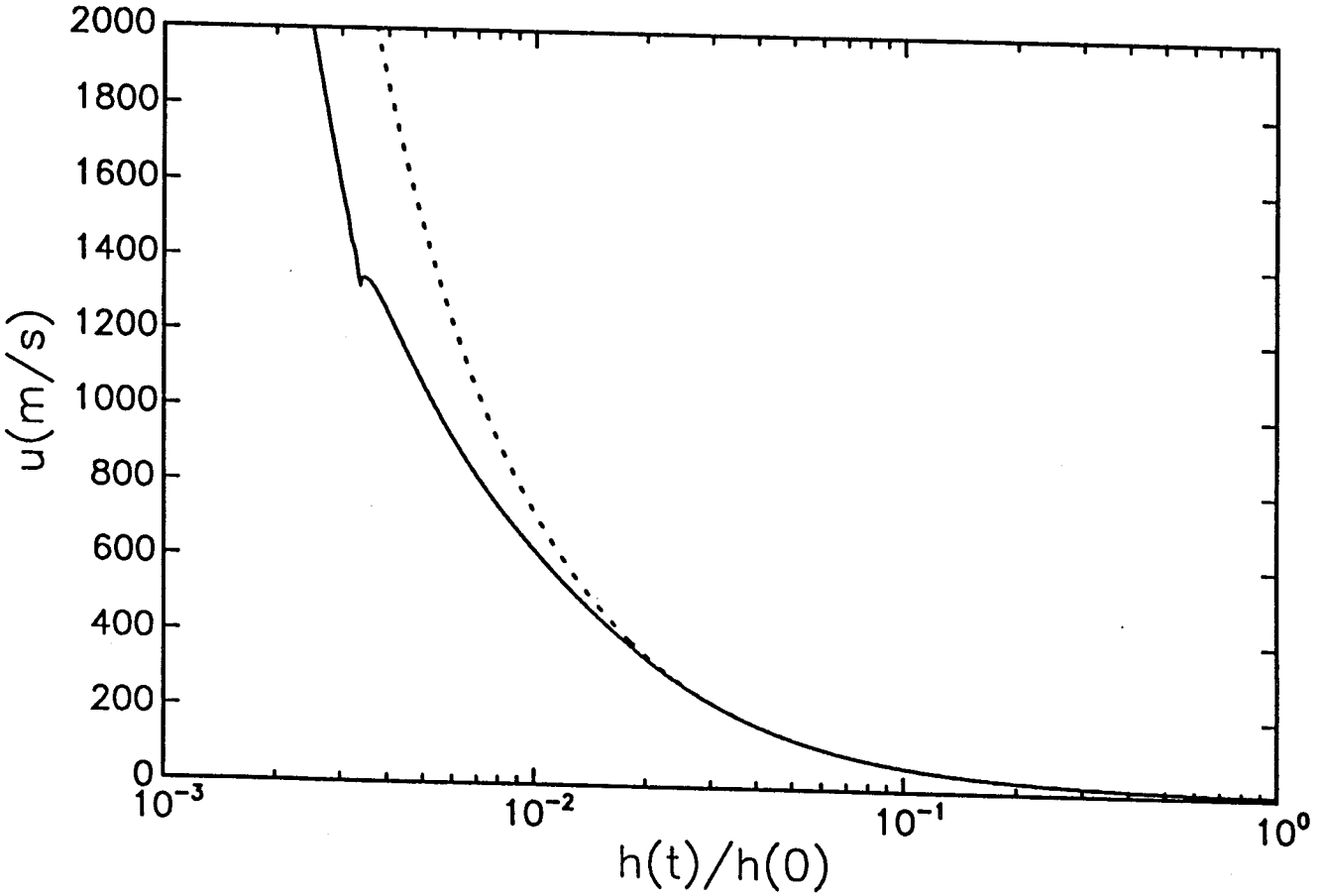

Fig. 5 The radial velocity on the plane of symmetry at the plates' edge $r = R$ as a function of the gap width $h/h(0)$ for a constant velocity $V_0 = 1$ m/s and adiabatic walls. The solid line is for a temperature-dependent viscosity, the dashed line for a constant viscosity.

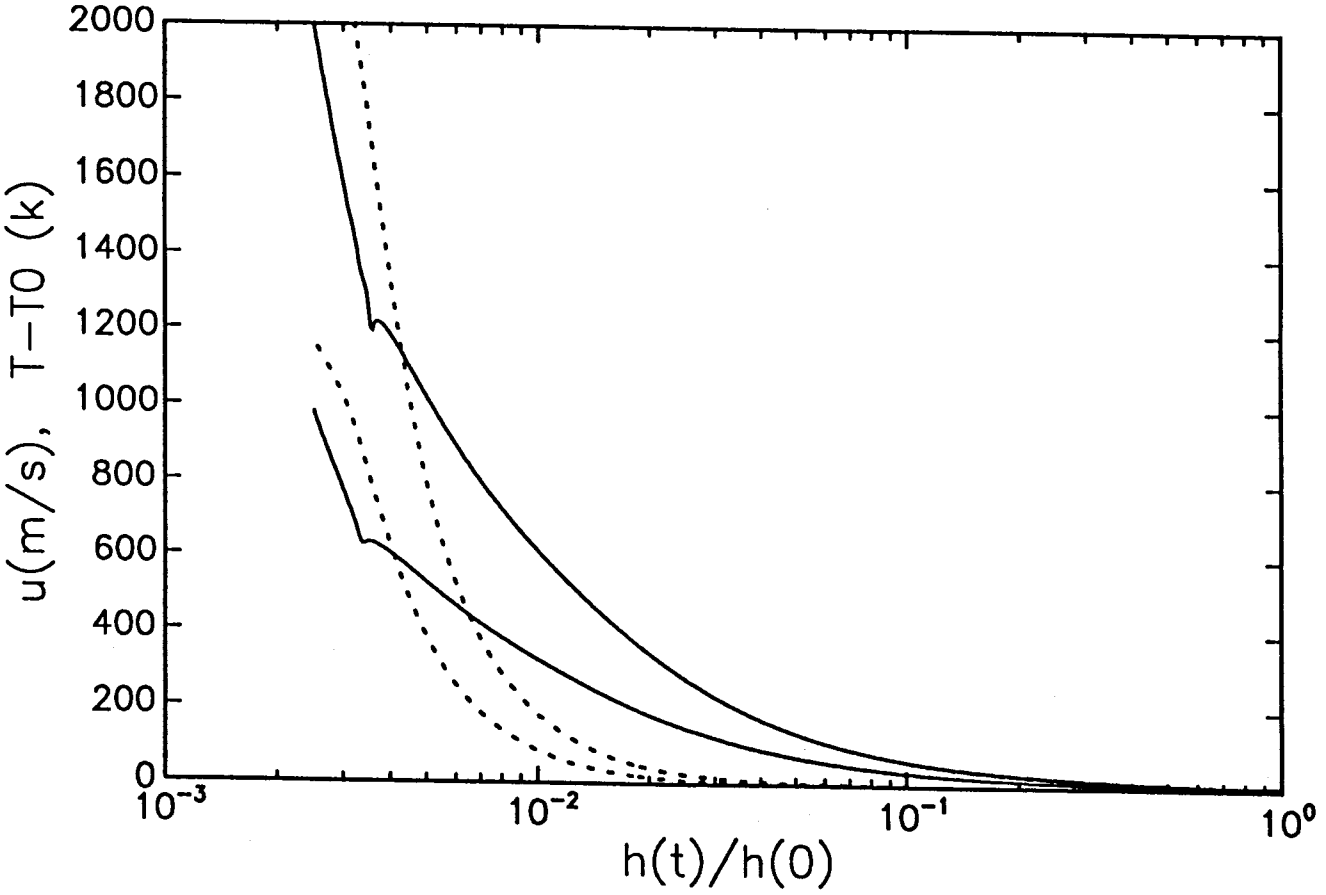

Fig. 6 The solid lines are the radial velocity on the plane of symmetry at the plates' edge $r = R$ for constant velocities $V_0 = 1$ m/s (upper curve) and 0.5 m/s as functions of $h/h(0)$. The dashed lines are the corresponding temperature increases at the plates for adiabatic boundary conditions. Units are in m/s for the velocities and K for the temperature increases.

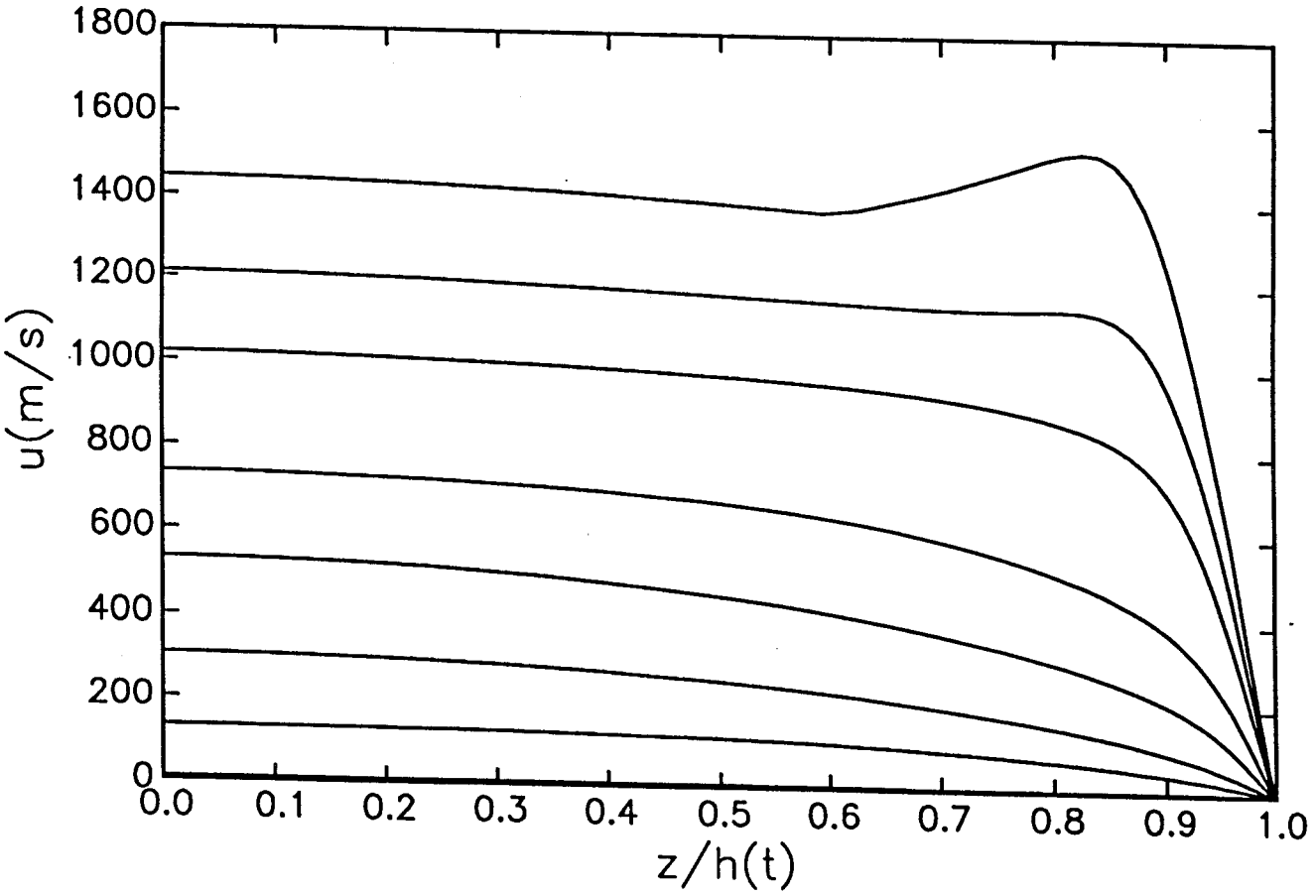

Fig. 7 Distribution of the radial velocity across the gap at the edge of the plates for a constant velocity of approach $V_0 = 1$ m/s and an isothermal wall. The lines are for the same values of $h/h(0)$ as in Fig. 2. Specifically, in descending order, $h/h_0 = 0.00369, 0.00451, 0.00551, 0.00822, 0.0123, 0.0223, 0.0497, 0.819$.

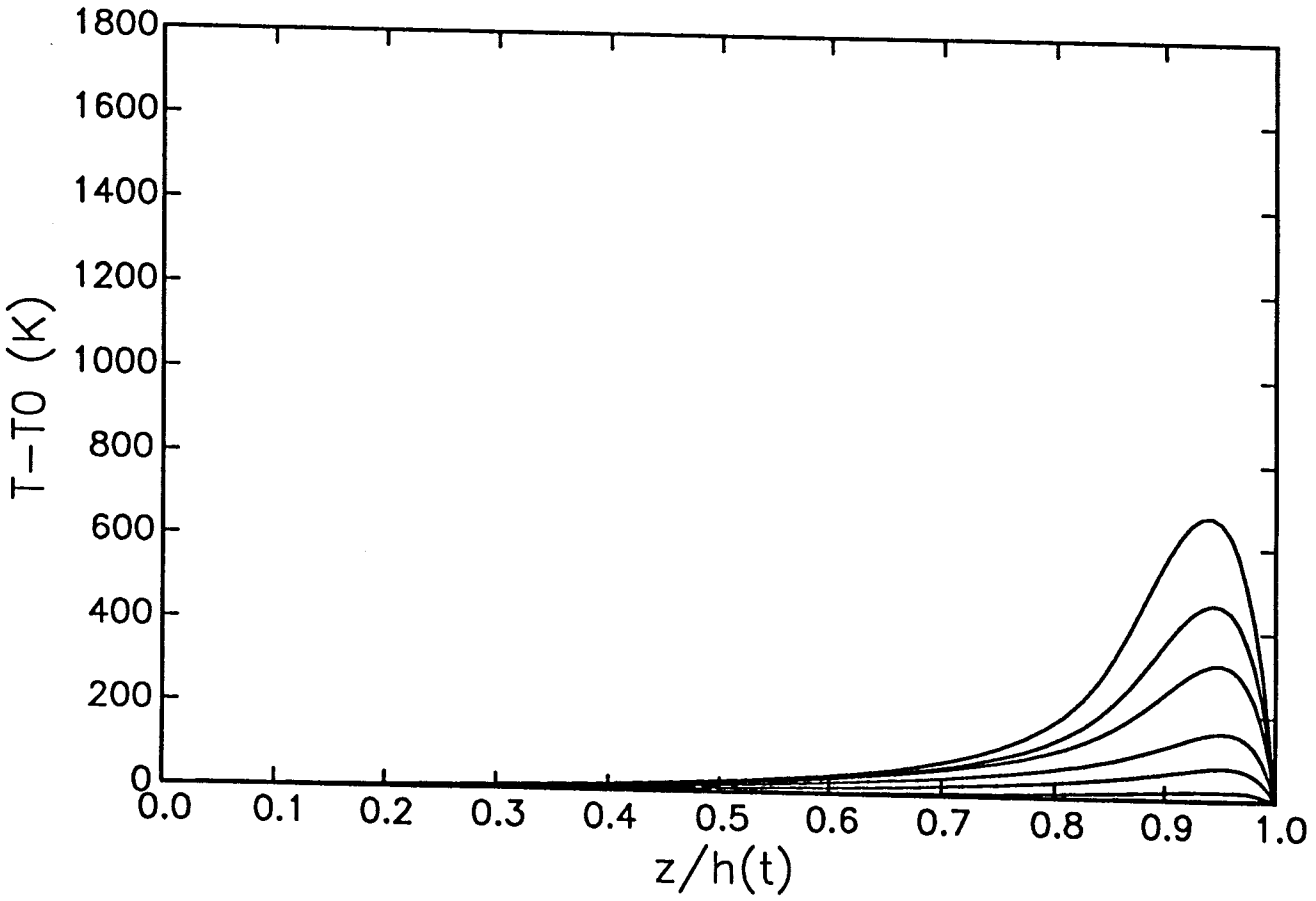

Fig. 8 Temperature distributions across the gap at $r = R$ for an isothermal wall for the same values of $h/h(0)$ as in the previous figure.

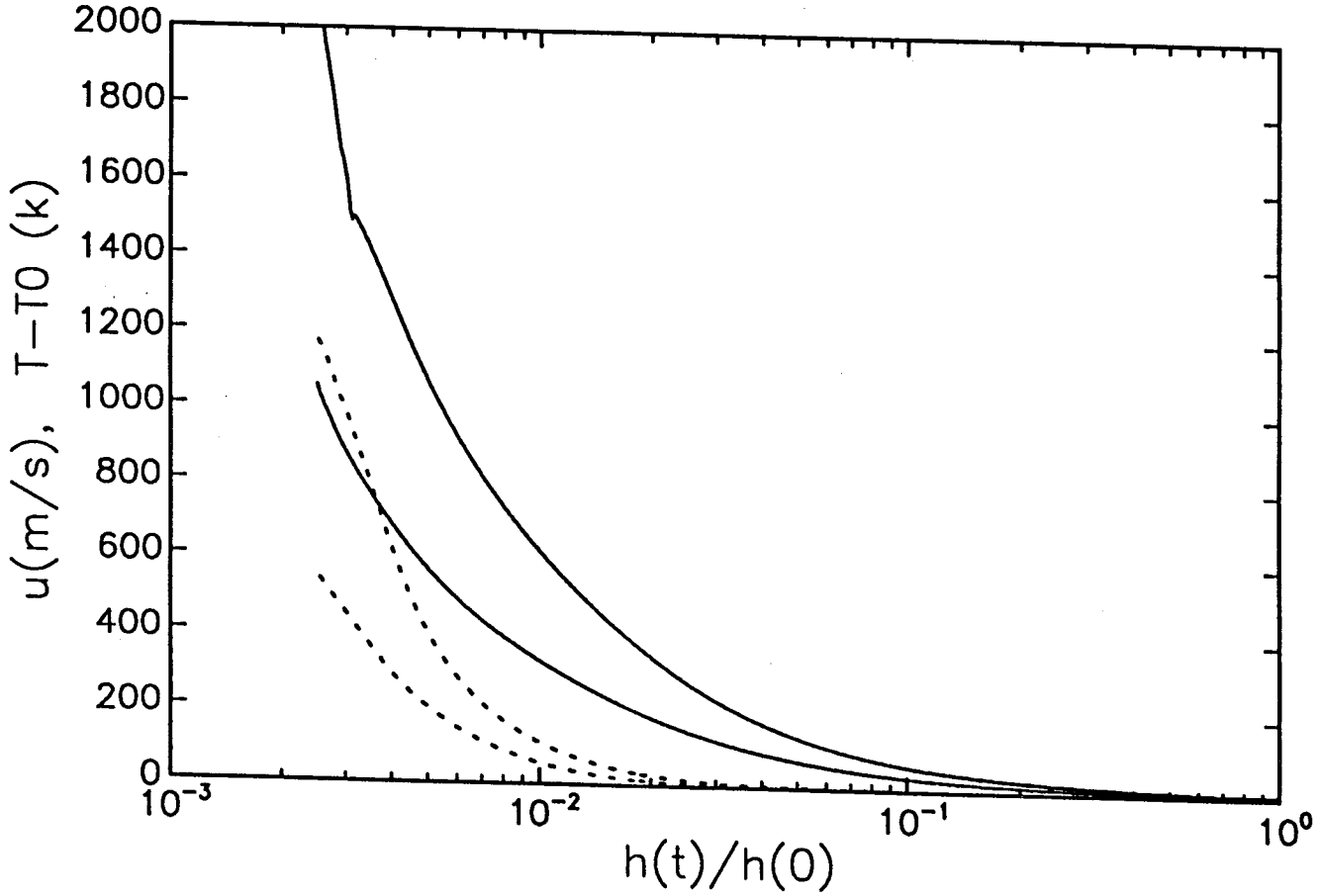

Fig. 9 The solid lines are the radial velocity on the plane of symmetry at the plates' edge $r = R$ for constant velocities $V_0 = 1$ m/s (upper curve) and 0.5 m/s as functions of $h/h(0)$. The dashed lines are the corresponding temperature increases at the plates for isothermal boundary conditions. Units are in m/s for the velocities and K for the temperature increases.

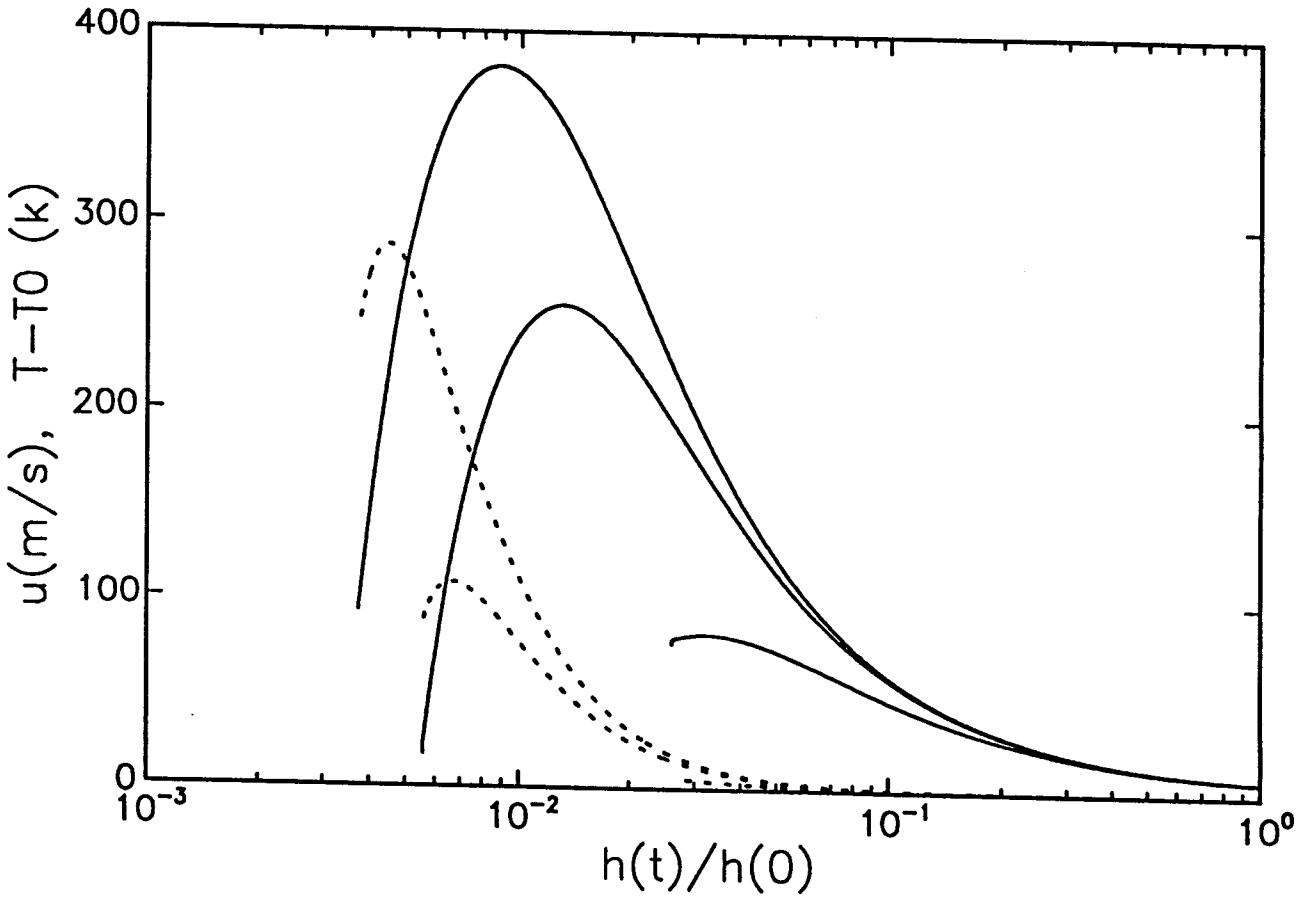

Fig. 10 Same as the previous figure for a variable velocity of approach controlled by the inertia of the plates. The three curves are, in ascending order, for $M = 0.2$, 1, and 2 kg and the walls are adiabatic.

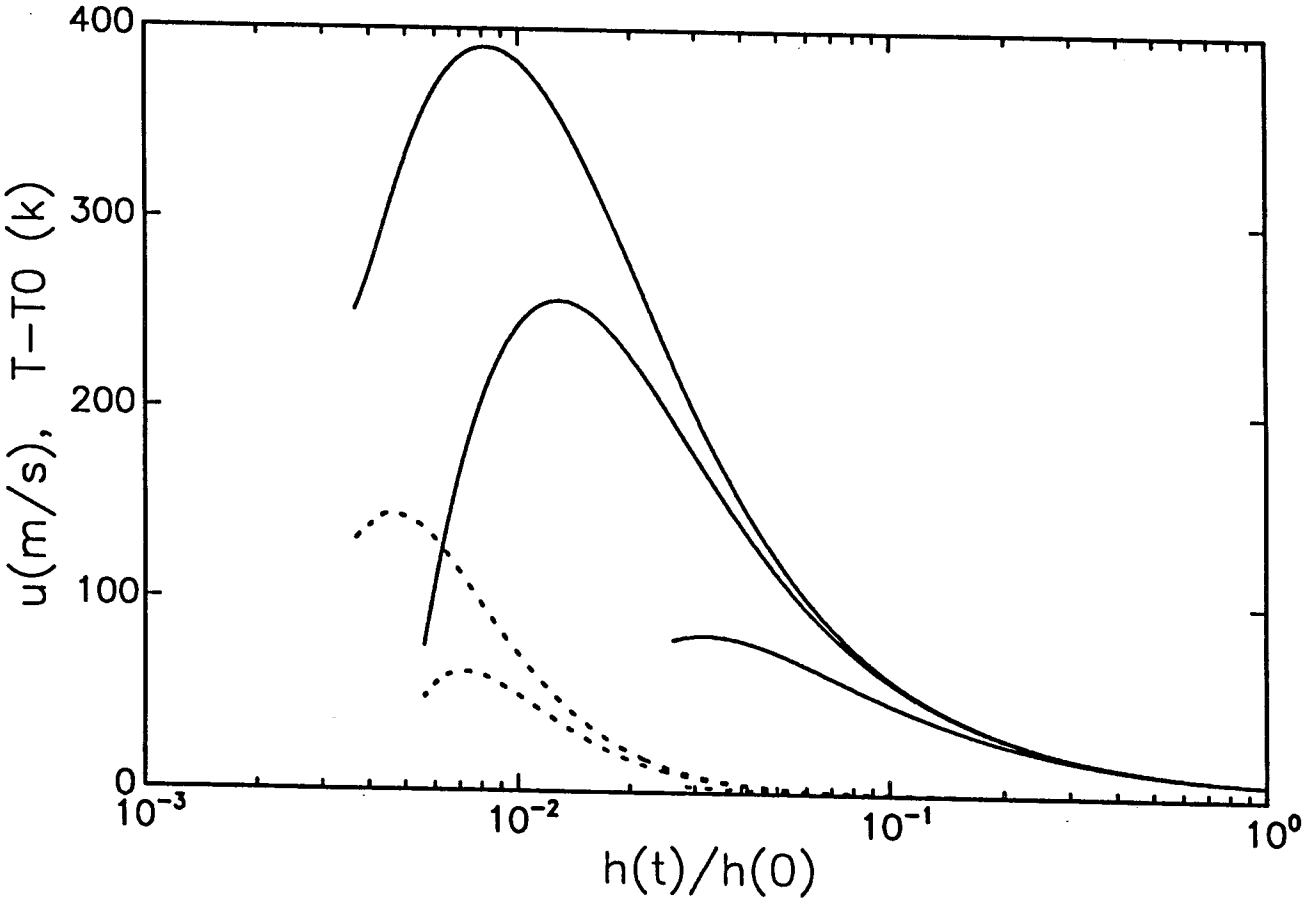

Fig. 11 Same as Fig. 10 for isothermal walls.

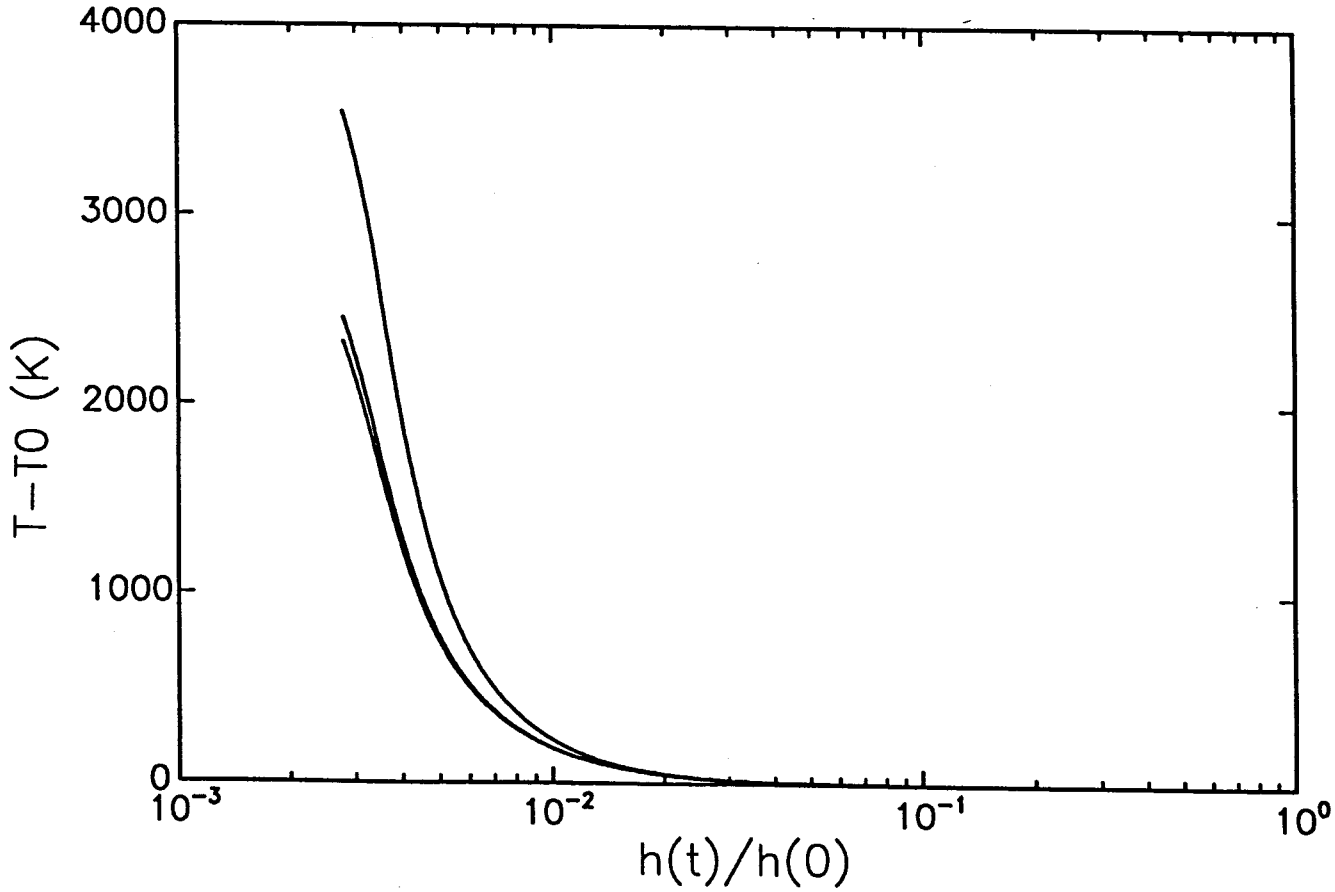

Fig. 12 Temperature rises in the presence of slip, with adiabatic walls and a fixed velocity $V_0 = 1$ m/s. The three curves are, in ascending order, for $\lambda = 0$, 10, and 100 nm.

Reports, Personnel, Patents

- **Reports**: In addition to the present final report, one other progress report for the period August 15 to December 31, 1993 was prepared in the course of the present grant.
  Authors: A. Prosperetti and H. Yuan
  Title: A theoretical study of ignition mechanisms in liquid propellants
  Institution: Department of Mechanical Engineering, The Johns Hopkins University
  Date: January 31, 1994

- **Publications**: One paper presented at the 31st JANNAF Combustion Subcommittee Conference Conference
  Authors: A. Prosperetti and H. Yuan
  Title: Viscous heating of liquid layers under intense shear
  Date: 17 - 21 October 1994

  Three more journal papers are in preparation

- **Personnel**:

  Prof. Andrea Prosperetti, Principal Investigator

  He Yuan, Research Assistant. Mr. Yuan expects to obtain his Ph. D. degree in the Spring of 1995

- **Inventions**: None

References

[1] Bourne N.K. and Field J.E. Cavity collapse in a heterogeneous commercial explosive. In *Proceedings of the Ninth Symposium (International) on Detonation*, pages 869–878, Washington, 1989. Office of Naval Research.

[2] Bourne N.K. and Field J.E. Bubble collapse and the initiation of explosion. *Proc. R. Soc. London*, A435:423–435, 1991.

[3] Bourne N.K. and Field J.E. Shock-induced collapse of single cavities in liquids. *J. Fluid Mech.*, 244:225–240, 1992.

[4] Bourne N.K. and Walley S.M. Impact ignition of liquid propellants. Technical report, Physics & Chemistry of Solids, Cavendish Laboratory, University of Cambridge, (1993).

[5] Chaudhri M.M. and Field J.E. The role of rapidly compressed gas pockets in the initiation of condensed explosives. *Proc. R. Soc. London*, A340:113–128, 1974.

[6] Coley G.D. and Field J.E. The role of cavities in the initiation and growth of explosion in liquids. *Proc. R. Soc. London*, A335:67–86, 1973.

[7] Davis S.H. and Miksis M.J. Slip over rough and coated surfaces. *J. Fluid Mech.*, 273:125–139, (1994).

[8] Dussan V. E.B. On the spreading of liquids on solid surfaces: Static and dynamic contact lines. *Ann. Rev. Fluid Mech.*, 11:371–400, (1979).

[9] Field J.E. Hot spot ignition mechanisms for explosives. *Accnts. Chem. Res.*, 25:489–496, (1992).

[10] Field J.E., Swallowe G.M., and Heavens S.N. Ignition mechanisms of explosives during mechanical deformation. *Proc. R. Soc. Lond.*, A382:231–244, (1982).

[11] Field J.E., Bourne N.K., Palmer S.J.P., and Walley S.M. Hot-spot ignition mechanisms for explosives and propellants. *Phil. Trans. R. Soc. Lond.*, A339:269–283, (1992).

[12] Frey R.B. Cavity collapse in energetic materials. In *Proceedings of the Eighth Symposium (International) on Detonation*, pages 68–80, Washington, 1985. Office of Naval Research.

[13] Gresho P.M. Incompressible fluid dynamics: some fundamental formulation issues. *Ann. Rev. Fluid Mech.*, 23:413–453, (1991).

[14] Heavens S.N. and Field J.E. The ignition of a thin layer of explosive by impact. *Proc. R. Soc. Lond.*, A338:77–93, (1974).

[15] Huh C. and Scriven L.E. Hydrodynamic model of steady movement of soli/liquid/fluid contact line. *J. Colloid Interface Sci.*, 35:85–101, (1971).

[16] Johansson C.H. The initiation of liquid explosives by shock and the importance of liquid break up. *Proc. R. Soc. Lond.*, A246:160–167, 1958.

[17] Kamath V. and Prosperetti A. Numerical integration methods in gas-bubble dynamics. *J. Acoust. Soc. Am.*, 85:1538–1548, 1989.

[18] Kamath V., Prosperetti A., and Egolfopoulos F.N. A theoretical study of sonoluminescence. *J. Acoust. Soc. Am.*, 94:248–260, 1993.

[19] Krishna Moan V. and Field J.E. Impact initiation of hexanitrostilbene. *Combustion and Flame*, 56:269–277, (1984).

[20] Krishna Moan V., Field J.E., and Swallowe G.M. Effects of physical inhomogeneities on the impact sensitivity of solid explosives: A high-speed photographic study. *Combusion Sci. and Tech.*, 44:269–278, (1984).

[21] Morrison W.F., Knapton J.D., and Mandzy J. A mechanism for the compressive ignition of liquid monopropellants. Technical Report ARBRL-MR-03173, U.S. Army Ballistic Research Laboratory, 1982.

[22] Oğuz H.N. and Prosperetti A. Surface-tension effects in the contact of liquid surfaces. *J. Fluid Mech.*, 203:149–171, 1989.

[23] Oğuz H.N. and Prosperetti A. Bubble entrainment by the impact of drops on liquid surfaces. *J. Fluid Mech.*, 219:143–179, 1990.

[24] Prosperetti A. The thermal behaviour of oscillating gas bubbles. *J. Fluid Mech.*, 222:587–616, 1991.

[25] Prosperetti A. and Lezzi A.M. Bubble dynamics in a compressible liquid. part i. first-order theory. *J. Fluid Mech.*, 168:457–478, 1986.

[26] Prosperetti A., Crum L.A., and Commander K.W. Nonlinear bubble dynamics. *J. Acoust. Soc. Am.*, 83:502–514, 1988.

[27] Randolph A.D. and Simpson K.O. Rapid heating-to-ignition of high explosives. ii. heating by gas compression. *Ind. Eng. Chem. Fundam.*, 15:7–15, 1976.

[28] Richardson S. On the no-slip boundary condition. *J. Fluid Mech.*, 59:707–719, (1973).

[29] Swallowe G.M. and Field J.E. The ignition of a thin layer of explosive by impact: The effect of polymer particles. *Proc. R. Soc. Lond.*, A379:389–408, (1982).

[30] Winter R.E. and Field J.E. The role of localized plastic flow in the impact initiation of explosives. *Proc. R. Soc. Lond.*, A343:399–413, (1975).